



Department of Micrometeorology
University of Bayreuth



Determination of the atmospheric boundary layer height in complex terrain during SALSA 2005

Diploma thesis in Geoecology

Katharina Staudt

September 2006

Content

Abstract	III
Zusammenfassung	IV
1 Introduction	1
2 Theoretical Background	3
2.1 Thermally induced wind systems	3
2.1.1 Slope winds	4
2.1.2 „Alpine Pumping“: circulation between mountains and foreland	4
2.2 Sodar/RASS	6
2.2.1 Measuring principle sodar	6
2.2.2 Measuring principle RASS	8
2.3 The atmospheric boundary layer (ABL)	8
2.3.1 The convective boundary layer (CBL)	10
2.3.2 The stable boundary layer (SBL)	11
2.3.3 The atmospheric boundary layer in complex terrain	11
2.3.4 The atmospheric boundary layer height	14
2.3.4.1 The ABL height determined from measurements	15
2.3.4.2 Parameterisations	16
2.3.4.3 Slab models	20
3 Data and methods	24
3.1 SALSA 2005	24
3.1.1 Investigation area	24
3.1.2 Measuring stations	26
3.2 Data	27
3.2.1 Meteorological Observatory Hohenpeißenberg (MOHp)	27
3.2.2 Sodar/RASS	27
3.2.3 Radiosondes	28
3.2.4 Tethered balloon	29
3.2.5 Turbulence measurements	29
3.2.6 Lokal-Modell	30
3.3 Methods for the determination of the atmospheric boundary layer height	30
3.3.1 Determination from sodar/RASS data	30
3.3.2 Determination from radiosonde and tethered balloon data	33
3.3.3 NWP model output (Lokal-Modell)	35
3.4 Input data for the parameterisations and the slab models	36
3.4.1 Parameterisations for the SBL height	36

3.4.2	Slab models for the CBL height	36
3.5	Statistical measures to evaluate model performance	37
4	Results and discussion	38
4.1	Weather conditions during the experiment	38
4.2	Thermally induced wind systems	40
4.2.1	Slope winds	40
4.2.2	Alpine pumping	42
4.3	Characterisation of the three golden days	47
4.4	Determination of the atmospheric boundary layer height	49
4.4.1	The ABL height determined from radiosonde data	50
4.4.2	The ABL height determined from sodar/RASS data	53
4.4.2.1	Visual inspection of reflectivity profiles	53
4.4.2.2	Automatic detection	57
4.4.3	Comparison of ABL heights inferred from sodar and balloon data	62
4.4.4	Parameterisations of the SBL height	66
4.4.5	Slab models for the CBL height	71
4.4.6	The ABL height in the Lokal-Modell	75
5	Conclusions	78
6	References	82
7	Index of figures	92
8	Index of tables	96
9	Index of used abbreviations and symbols	98
9.1	Abbreviations	98
9.2	Latin symbols	98
9.3	Greek symbols	100
10	Appendix: Technical specifications of measurement systems	101
	Acknowledgements	105
	Eidesstattliche Erklärung	106

Abstract

This study investigates the atmospheric boundary layer (ABL) height over complex terrain in the Bavarian Alpine foreland. Data was collected during the field experiment SALSA 2005 at Hohenpeißenberg in August and September of 2005. Sodar/RASS measurements, tethered balloon soundings and turbulence measurements were performed at the foot of the mountain, which overtops the surrounding terrain by about 300 m.

In the first step, thermally induced wind systems were identified. The mesoscale circulation system between the mountains and the foreland, referred to as Alpine pumping, was observed on four consecutive fair weather days. On the smallest scale of thermally induced wind systems, slope winds occurred.

The ABL height was determined for three selected days that were assumed to represent different weather conditions (easterly winds, westerly winds, Alpine pumping). Emphasis was placed on sodar measurements. Visual inspection of reflectivity profiles as well as automatic detection using profiles of reflectivity and the standard deviation of the vertical wind velocity component were applied to determine the ABL height. The applied automatic method performed reasonably well but could not replace the visual inspection method, which turned out to be the most reliable. Sodar reflectivity profiles frequently revealed a complex ABL structure. Tethered balloon measurements for one of the selected days were compared to sodar data which confirmed this complex structure. ABL heights determined with various methods using profiles of meteorological variables from routine radiosonde ascents at three sites in the vicinity turned out to be of only limited value due to their low temporal and vertical resolution. The applicability of parameterisations of the stable boundary layer (SBL) depth and of slab models for the growth of the convective boundary layer (CBL) using surface measurements was investigated in complex terrain. If the SBL top is assumed to be horizontal and the difference in elevation between measurement sites is taken into account, simple parameterisations reasonably agreed with SBL depths from sodar measurements, whereas more complicated parameterisations underestimated the SBL depth. Results from slab models agreed well with measurements for two of the three days, whereas these models largely overestimated the CBL depth for the day when Alpine pumping developed. This overestimation was attributed to the influence of factors such as advection and subsidence that were neglected in the model but could not be neglected under the prevailing conditions. Similar performance was observed for the Lokal-Modell.

The ABL structure was strongly influenced by Alpine pumping with distinct layering as well as suppressed CBL growth. Processes triggered by Alpine pumping such as cold air advection from the lower parts of the Alpine foreland as well as subsidence that replaces boundary layer air which is pumped into the Alps strongly affected the ABL structure.

Zusammenfassung

Die vorliegende Arbeit untersucht die Höhe der atmosphärischen Grenzschicht über komplexem Gelände des Bayerischen Alpenvorlands. Messungen wurden während des Feldexperiments SALSA 2005 am Hohenpeißenberg im August und September 2005 durchgeführt. Dabei kamen ein Sodar/RASS System, ein Fesselballon System und ein Turbulenzmesskomplex am Fuß des Berges, der das umliegende Gelände um 300 m überragt, zum Einsatz.

Als erstes wurden thermisch induzierte Windsysteme identifiziert. Die mesoskalige Zirkulation zwischen dem Gebirge und dem Vorland, auch als Alpines Pumpen bezeichnet, wurde an vier aufeinanderfolgenden Tagen beobachtet. Auf der kleinsten Skala thermisch induzierter Windsysteme traten Hangwinde auf.

Die Höhe der atmosphärischen Grenzschicht wurde für drei ausgewählte Tage bestimmt. Es wurde angenommen, dass diese Tage unterschiedliche Wetterbedingungen repräsentieren (Ostwind, Westwind, Alpines Pumpen). Besondere Bedeutung kamen den Sodar/RASS Messungen zu. Reflektivitätsprofile wurden sowohl visuell als auch automatisiert in Kombination mit Profilen der Standardabweichung des Vertikalwindes zur Bestimmung der Grenzschichthöhe herangezogen. Ergebnisse aus der automatisierten Routine waren zwar zufriedenstellend, können jedoch nicht die visuelle Methode ersetzen, die sich als zuverlässigste Methode herausstellte. Eine komplexe Struktur der atmosphärischen Grenzschicht ist oft an den Reflektivitätsprofilen erkennbar. Ein Vergleich von Fesselballonmessungen mit Sodarmessungen für einen der drei Tage bestätigt die komplexe Struktur der Grenzschicht. Die Höhe der atmosphärischen Grenzschicht wurde mit verschiedenen Methoden aus Profilen meteorologischer Parameter bestimmt, die von routinemäßig durchgeführten Radiosondenaufstiegen an drei Stationen in der Umgebung gemessen wurden. Der Nutzen der Grenzschichthöhen aus Radiosondenprofilen ist beschränkt durch die geringe zeitliche und vertikale Auflösung der Daten. Die Anwendbarkeit von Parametrisierungen für die stabile Grenzschicht sowie von sogenannten slab models für die konvektive Grenzschicht, in die bodennahe Messungen eingehen, wurde in komplexem Gelände untersucht. Wird die Obergrenze der stabilen Grenzschicht als horizontal angenommen und die Höhendifferenz zwischen den Messstationen eingerechnet, erzielten einfache Parametrisierungen annehmbare Ergebnisse für die Grenzschichthöhe verglichen mit Ergebnissen aus Sodarmessungen, wohingegen kompliziertere Parametrisierungen die Grenzschichthöhe unterschätzten. Ergebnisse aus slab models stimmten an zwei der drei Tagen gut mit gemessenen Grenzschichthöhen überein. Die Höhe der konvektiven Grenzschicht wurde jedoch für den Tag, an dem Alpines Pumpen ausgeprägt war, stark überschätzt, was dem Einfluss von Faktoren wie Advektion und Absinken von Luftmassen zugeschrieben wurde. Die Modelle vernachlässigten diese Faktoren, was unter den gegebenen Bedingungen nicht zulässig

war. Ergebnisse aus dem Lokal-Modell verhielten sich ähnlich.

Die Struktur der Grenzschicht wurde stark vom Alpinem Pumpen beeinflusst, was sich in einer deutlichen Schichtung und in unterdrücktem Anwachsen der Grenzschicht auswirkte. Prozesse die durch Alpines Pumpen ausgelöst werden, wie Advektion von kalter Luft aus den tiefergelegenen Bereichen des Alpenvorlands, als auch Absinken von Luftmassen, die Grenzschichtluft die in die Alpen gepumpt wurde ersetzen, beeinflussten die Struktur der Grenzschicht.

1 Introduction

The atmospheric boundary layer (ABL) is the lowest part of the troposphere where the earth's surface interacts with the large scale atmospheric flow. Its height is a fundamental parameter that is needed as input for the prediction of pollutant concentrations (Beyrich, 1997), weather prediction (Holtslag et al., 1990) and climate models as well as for scaling of turbulence measurements (Holtslag and Nieuwstadt, 1986). Methods to determine the ABL height can be divided in two basic groups: one using profile data, either from measurements or from numerical model output, the other consisting of parameterisations using simple equations or models that only require a limited number of input data (Seibert et al., 1998, 2000). Remote sensing techniques such as sodar/RASS measurements are a very valuable tool in boundary layer research. Such a continuously working measurement system provides profile data with a high temporal and vertical resolution (Beyrich, 1997). Primarily, profiles of reflectivity are used to determine the stable boundary layer (SBL) height as well as the development of the convective boundary layer (CBL). In the literature, various criteria to determine the ABL height from reflectivity data can be found (for a review see Beyrich, 1997). Unfortunately, only the SBL depth and the evolution of the CBL in the morning hours can be determined due to the limited range of sodar/RASS. Measurements from tethered balloon and routine radiosonde ascents are another direct way of obtaining profile data. Several meteorological parameters and additional chemical compounds can be observed and the shape of their profiles can be used for the determination of the ABL height (Seibert et al., 1998, 2000). Parameterisations for the SBL height are frequently used in models. These parameterisations require surface layer measurements, particularly flux measurements, as input variables and range from simple relationships considering only single parameters (e.g. Koracin and Berckowicz, 1988) to more complex equations in the form of multi-limit equations (e.g. Zilitinkevich and Mironov, 1996) or derived from dimensional analysis (Steenefeld et al., 2006a). The CBL height can be modelled with slab models, assuming an idealized structure of the CBL (e.g. Tennekes, 1973).

Extensive research has been done on more or less idealized ABLs, which means in homogeneous and flat terrain. Therefore, the structure of the ABL under these conditions is understood well (Arya, 2001). The methods to determine the ABL height mentioned before were developed and verified mainly under ideal conditions. Less attention has been paid to complicating factors which influence the ABL such as complex topography. In complex terrain, knowledge is also lacking concerning the spatial generalization of measurements (Beyrich, 1997).

Even though a good understanding of basic wind systems that develop in complex topography was achieved during the last century (Whiteman, 1990), mountain meteorological research is ongoing and new phenomena continue to be discovered (De

Wekker, 2002). Thermally induced wind systems that occur in complex terrain are found on various scales. On the smallest scale, there are slope wind systems (Vergeiner and Dreiseitl, 1987), whereas on the largest scale wind systems between a whole mountain range and its foreland are thermally triggered (Lugauer and Winkler, 2005). These wind systems have considerable influence on the diurnal development of the ABL in complex terrain (Whiteman, 2000). Here, factors such as advection and subsidence were found to modify the structure of the ABL in comparison to the ABL over flat, homogeneous terrain. Generally, the ABL over orographically structured terrain has a more complex structure.

The aim of this study was to determine the boundary layer height at Hohenpeißenberg, a complex terrain of the Bavarian Alpine foreland, during SALSA 2005 ('Contribution of nitrous acid to the atmospheric OH-concentration'). Thermally induced wind systems developed on different scales and were taken into consideration and identified throughout this study, with emphasis on slope winds and the mesoscale circulation between the Alps and the foreland called Alpine pumping (Lugauer and Winkler, 2005). The ABL height was determined using different methods. On the one hand, profile data from measurements from sodar/RASS, a tethered balloon system and routine radiosoundings were analysed, on the other hand, a simple model and parameterisations for the boundary layer using surface measurements were applied. Even though these methods have been developed for flat homogeneous terrain, they were applied in complex terrain without modification and their applicability was tested. The results from different methods were compared to each other. The deviation from the ideal development of the ABL height in the complex terrain of Hohenpeißenberg was determined.

2 Theoretical Background

This chapter outlines the theoretical background of this thesis. The first part deals with thermally induced wind systems that develop over complex topography. In this context, two wind systems, namely slope winds and the mountain-plain wind system are explained in detail because of their importance for this study. The second part introduces sodar/RASS measurements and gives some insight into the measuring principles. The atmospheric boundary layer is the topic of the third part, a description of its structure in space and time over flat homogeneous terrain as well as its structure over complex terrain is presented. Ways to measure, parameterise and model the height of the atmospheric boundary layer are dealt with in the last part of this section.

2.1 *Thermally induced wind systems*

Over complex topography, thermally driven diurnal mountain wind systems develop. Four wind systems of different scales can be observed (Whiteman, 2000): the slope wind system, the along-valley wind system, the cross-valley wind system and the mountain-plain wind system. Generally, winds blow upslope, upvalley and from the plain to the mountains during the daytime, and conversely at night time (Whiteman, 2000).

Valley and slope winds have been researched since the 19th century. In the first half of the 20th century, important research was done by several mountain meteorologists (e.g. Defant, 1949; for an overview see Whiteman, 1990), who described the currently recognized theory and a schematic of the diurnal development of slope- and valley flows. Since the 1980's the availability of new instruments and models led to considerable progress in this field of research. A review from Whiteman (1990) focused on valley and slope winds and textbooks such as Whiteman (2000) and Barry (1992) gave an introduction to mountain wind systems.

Horizontal pressure gradients that result from temperature differences developing over complex terrain trigger mountain winds. Winds thereby blow from areas with lower temperatures and higher pressures towards areas with higher temperatures and lower pressures. Compensatory flows are observed higher in the atmosphere that close circulation systems. Diurnal mountain winds develop best under weak gradient synoptic conditions when skies are clear and winds aloft are weak. Vergeiner and Dreiseitl (1987) pointed out that valley wind systems can be quite different in various valleys due to different relief features, even though certain methods and concepts are universally applicable. De Wekker (2002) summarised factors that influence the duration, intensity, vertical extent and other characteristics of slope- and valley flows. These include among others, valley width, ridge height, valley orientation, slope steepness, vegetative cover and latitude. Observation of single components of the mountain wind systems are rarely possible, as complex flow patterns almost always result from the interaction of the different components with each

other as well as with the regional and synoptic scale flows (Whiteman, 2000).

2.1.1 Slope winds

Slope winds represent the smallest scale of mountain wind systems (Vergeiner and Dreiseitl, 1987). They develop due to the horizontal temperature contrasts between the air over a slope and the air at the same level in the ambient environment. During the day, upslope winds and during the night downslope winds are typically observed, blowing parallel to the inclination of the slope (Whiteman, 1990). Wind speeds in the order of magnitude of a few meters per second ($1-5 \text{ m s}^{-1}$) are reached and peak a few meters above the surface (Whiteman, 2000). Dependent on the length of the flow, wind speeds can reach gale force on the long slope of the continental ice dome in Antarctica. Downslope and upslope flows vary over time and space as well as in depth, with downslope flows generally being shallower than upslope flows. The depth of downslope flows can be approximated as 5% of the drop in elevation from the ridge top. Upslope flows may reach a depth of 50-150 m during the first several hours after sunrise. Slope flows on the smaller scale, as considered in the context of this thesis, are spontaneous and intermittent in space and time (Vergeiner and Dreiseitl, 1987). Usually upslope flows start a few minutes after sunrise as an immediate reaction to insolation. Spatial variations in the surface energy budget and small-scale features of the underlying terrain may strongly influence slope winds.

2.1.2 „Alpine Pumping“: circulation between mountains and foreland

During fair weather days, large temperature differences between the air over the mountains and the air over the adjacent plain develop. The mountain atmosphere exhibits larger daily ranges of temperature, with colder temperatures at night and in the morning and warmer temperatures during the day. Vergeiner and Dreiseitl (1987) observed a mean daily range of vertically averaged temperature that is more than two times larger in the valley than in the foreland. This difference can be attributed to the volume effect (Steinacker, 1984; Whiteman, 2000). Air columns of the same area at its top contain a smaller volume of air over the valley than over the plain because of the sloping sidewalls. Assuming the same amount of solar radiative input, the air over the mountains heats up faster due to the smaller air volume. Temperature differences between the mountains and the foreland lead to pressure differences, forming a heat low in the mountains by day. Wind from the plain to the mountains is driven by this pressure gradient. Therefore, air from the foreland is “pumped” into the mountains during the day, leading to the term Alpine pumping (“Alpines Pumpen” in German) for this wind system in the Northern Alps (Lugauer and Winkler, 2002). At night, the reversed wind is developed, with colder air over the mountains flowing from the mountains to the plain.

In southern Bavaria, Alpine pumping was investigated by statistical analysis of meteorological data from several weather stations in the alpine foreland and the Alps of the years 1996-2000 (Lugauer and Winkler, 2005) and during the field experiment VERTIKATOR ('Vertical exchange and orography') in July 2002 (Lugauer et al., 2003; Fiedler et al., 2005). These studies resulted in the following picture of the meso-scale circulation between the Bavarian alpine foreland and the Alps. By day, a northerly flow transports boundary layer air from the foreland to the Alps, reaching strengths of only a few meters per second (Corsmeier et al., 2003). The layer that exhibits this northerly flow extends to 1000 to 1500 m above ground level (agl) over the alpine foreland, increasing from the north to the rim of the Alps (Weissmann et al., 2005; Reitebuch et al., 2003). Above the Alps, air is lifted convectively up to 3500 to 4500 m agl and transported with prevailing upper level winds. The onset of the northerly flow takes place at about 8 CET (Central European Time) within the valleys and advances to the north. The influence of Alpine pumping can cover distances of up to 100 km north of the Alpine rim (Lugauer and Winkler, 2005). During the night, the flow pattern is reversed and air is transported back from the Alps to the foreland. Alpine valleys opening to the north like the Isar, the Loisach and the Inn valley facilitate the flow between the foreland and the mountains (Lugauer, 2003). Earlier work (Pamperin and Stilke, 1985) already reported the influence of a low-level jet that forms at night time from the Inn valley up to 50 km away from the Alps. The Alpine foreland not only slopes in a north-south direction, but an east-west direction, also up to the elevated region of the Allgäu, which adds an easterly component to the flow in regions east of the Allgäu during the day. Lugauer and Winkler (2005) quantified the probability of Alpine pumping by deriving classes of daily total global radiation. High probability was reported for days with mean daily total global radiation of more than 20 MJ m^{-2} , which was observed on about 42% of the days from April to August. The development of Alpine pumping is influenced by the upper level wind, with the strongest impact of westerly upper level winds. Figure 2-1 shows a schematic of the flow structure in association with 500 hPa winds from south and north. In both cases, evidence of a closed circulation can not be provided. In the case of southerly upper level winds, the backflow above the boundary layer is faster than the flow in the boundary layer. In contrast, a backflow can not be established against northerly upper level winds.

The mass flux from the foreland to the Alps could be determined with the help of lidar (light detecting and ranging) measurements (Weissmann et al., 2005). During a sunny day nearly the entire layer of air in the lowest thousand meters of the atmosphere between Munich and the Alps is transported to the Alps. Chemical compounds are transported by the exchange of boundary layer air to the free atmosphere above the Alps and pollutants are deposited in high mountain areas (Winkler et al., 2006). The arrival of the plume from Munich at the alpine rim was seen in lidar data (Winkler et al., 2004). Pollutant transport from the foreland to the Alps was also reported for the southern alpine foreland in Italy

(Wotawa et al., 2000). There, considerable export of boundary layer air from valleys to the free troposphere, called topographic venting, was observed (Henne et al., 2004). Convective lifting above the Alps results in convective cloud formation, frequently resulting in the development of thunderstorms (Höllner et al., 2004). Above the foreland, subsidence displaces air that is exported to the Alps and suppresses convective cloud formation, particularly during the afternoon (Lugauer and Winkler, 2005).

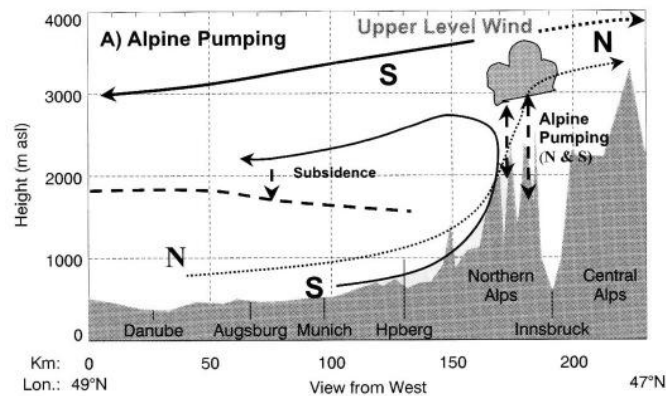


Figure 2-1: Schematic daytime flow structure with convective lifting in the Northern Alps and compensating subsidence above Southern Bavaria in association with 500 hPa winds from south (full arrows) and north (dotted arrows), respectively (Lugauer and Winkler, 2005).

2.2 Sodar/RASS

2.2.1 Measuring principle sodar

Sodar (sound detecting and ranging) was one of the first remote sensing techniques to be used in atmospheric science. Following some basic work on the theory of turbulent scattering mechanisms of sound and technical progress (Kallistratova, 1959, Tatarskii, 1961; McAllister et al., 1969; Little, 1969), sodar technique found its way into boundary layer research in the 1960's (Wilczak, 1996). In the beginning of the 1980's, commercial sodars were available and have been used since then as a reliable tool to profile mean winds in the lowest 500 m of the atmosphere. For an overview of the developments and applications of acoustic sounding see Neff and Coulter (1986).

Two basic variants of a geometrical configuration of a sodar have to be distinguished. In a bistatic system, there is a spatial separation of the transmitter and the receiver, whereas the monostatic sodar consists of only one antenna with transceivers, working as a transmitter and receiver depending on the phase of the measuring cycle (Kallistratova, 1997). The description of the measuring principle is limited to a monostatic sodar, which was used in this study.

A monostatic sodar can either consist of separate antennas for each beam (three big transducer tubes) or of a phased array of transducers. The sodar employed in this study consisted of 64 loudspeakers arranged in a square, able to transmit as well as receive. A

distinct phase shift between the loudspeakers generates 5 antennas due to interference, 4 tilted ones and one in the vertical direction (METEK, 2000).

The sodar emits short sound pulses of a distinct frequency. Due to scattering at small-scale temperature inhomogeneities, a fraction of the emitted energy returns to the receiving antenna of the sodar. These small-scale temperature inhomogeneities result from either fine-scale temperature layering or from turbulent fluctuations that have a typical size distribution and are transported with the mean wind flow (Beyrich, 1997). Scattering only occurs at inhomogeneities that have a characteristic scale l_t that is comparable to the wavelength of the sound λ_a . The Bragg condition describes this dependency (Kallistratova, 1997):

$$l_t = \frac{\lambda_a}{2 \sin \Theta_B} \quad (2-1)$$

with the Bragg angle Θ_B . If the Bragg angle equals 90° , the backscattered signal intensity results only from inhomogeneities having a l_t equal to one half of λ_a . Usually, this is within the ‘inertial subrange’ of the turbulence spectrum (Beyrich, 1997). The backscatter intensity is proportional to the acoustic refractive index structure parameter C_N^2 . C_N^2 depends on the temperature structure parameter C_T^2 (Wyngaard et al., 1971):

$$C_N^2 = \left(79 \cdot 10^{-6} \cdot \frac{p}{T^2} \right)^2 \cdot C_T^2 \quad (2-2)$$

where p is the mean air pressure and T is the ambient air temperature. To a first approximation, C_N^2 can be replaced by C_T^2 (Beyrich, 1997).

Heights corresponding to the recorded signals are allocated by the use of run durations of the sound, using a standard temperature measurement near the sodar to estimate the speed of sound. Within the sodar system used in this study, the term acoustic reflectivity R is used instead of the term backscatter intensity, which will be used throughout the rest of this study as well.

As temperature inhomogeneities are transported by the wind, a frequency shift can be observed in the backscattered signal compared to the emitted signal, which is called the Doppler shift. From this frequency shift, the projection of wind velocity in the sounding beam direction can be calculated. Using two tilted and one vertical antenna, wind velocity can be calculated as a three dimensional vector (Kallistratova, 1997).

The standard deviation of the vertical wind velocity σ_w is calculated either from the broadening of the mean backscattered spectra or from the high frequent time series of the vertical wind velocity w (Neff and Coulter, 1986). Measurements of the turbulent components of the wind speed are more challenging and research is continuing in this field (Wilczak, 1996).

Stronger rain or snow, perfect adiabatic conditions due to strong thermal mixing and

large noise from the surrounding constrain sodar measurements (Emeis et al., 2004).

2.2.2 Measuring principle RASS

A RASS (radio acoustic sounding system) is used as an extension to a sodar system to get simultaneous temperature profiles up to a few hundred meters (METEK, 2000, 2001). Such a system combines radar (radio detecting and ranging) and acoustic techniques. The backscatter of electromagnetic waves at fluctuations of the refractive index artificially caused by an emitted sound pulse, is the basic principle of the RASS. The Bragg condition which is a fixed relationship of the radar wavelength and the acoustic wavelength must be fulfilled (Matuura et al., 1986):

$$\lambda_r = 2 \cdot \lambda_a \quad (2-3)$$

Additionally, to obtain strong backscatter, the backscattered signal must be focused onto the receiver antenna (May et al., 1988).

The Doppler shift in the radar waves is a measure for the speed of sound c_a in case of a Doppler RASS, as used in this study. The sonic temperature T_s can be calculated from the observed speed of sound c_a at a particular height (Singal and Goel, 1997):

$$T_s = \frac{c_a^2 \cdot M}{\gamma \cdot R} \quad (2-4)$$

where M is the molecular weight of air, γ is the ratio of specific heats and R is the universal gas constant. The sonic temperature T_s nearly equals the virtual temperature T_v , which can be approximated by (May et al., 1989):

$$T_v = \left(\frac{c_a}{20.047} \right)^2 \quad (2-5)$$

Similarly to the sodar configuration, a bistatic as well as a monostatic RASS is possible. The RASS used in this study has a bistatic design, which means that the transmitter and the receiver are separated. This set-up is necessary due to the continuous operation of the transmitter and is advantageous due to the “wind-neutral” geometry, which means that under zero wind conditions, the focus of the scattered field and the centre of the receiver coincide (METEK, 2001).

To ensure that the Bragg condition is fulfilled at all heights, the frequency spectrum of the acoustic waves must cover a sufficient range of frequencies.

2.3 The atmospheric boundary layer (ABL)

The atmospheric boundary layer (ABL) is the lowest part of the troposphere where the surface of the earth interacts with the large scale atmospheric flow. Frequently, the term planetary boundary layer (PBL) is used synonymously (e.g. Arya, 2001). In this section an introduction to boundary layer structure and dynamics following Seibert et al. (1998, 2000)

and text books including Stull (1988), Foken (2006) and Garrat (1992) is given. Thereby only the idealized case of a non-disturbed ABL is described.

Figure 2-2 shows the diurnal evolution of the boundary layer. On a fair weather day a convective boundary layer (CBL) develops shortly after sunrise. It can be subdivided into three different layers: the surface layer, the mixed layer (ML) and the entrainment layer or entrainment zone. The surface layer makes up about 10% of the CBL and fluxes of energy and constituents are considered to be constant with height within this layer. The ML exhibits intensive vertical mixing due to mainly convectively driven turbulence. Therefore, profiles of most mean meteorological variables, especially potential temperatures, are found to be more or less constant with height. At the top, the ML is confined by the stable entrainment layer that forms a transition zone to the free atmosphere (FA) above. Through the entrainment layer warm air is mixed from above into the ML (entrainment). As a counteracting process air from the mixed layer penetrates into the stable FA in the form of thermals. The entrainment layer can considerably vary in thickness, but usually constitutes 10-30 % of the total depth of the CBL.

A stable boundary layer (SBL) starts to develop shortly before sunset, when due to longwave radiative cooling a near-surface temperature inversion is formed. In the formerly well-mixed layer turbulence decays, but the mean meteorological variables stay more or less the same. Therefore, this layer is called the residual layer (RL). At the transition to the free atmosphere, the RL is capped by a free inversion (capping inversion). Under stable as well as under convective conditions the lowest layer is the surface layer.

Holtslag and Nieuwstadt (1986) subdivided the ABL into different scaling regimes depending on the distance from the surface and the stability conditions. These regimes are characterized by certain relevant scales. The ABL height is one of the relevant scaling parameters.

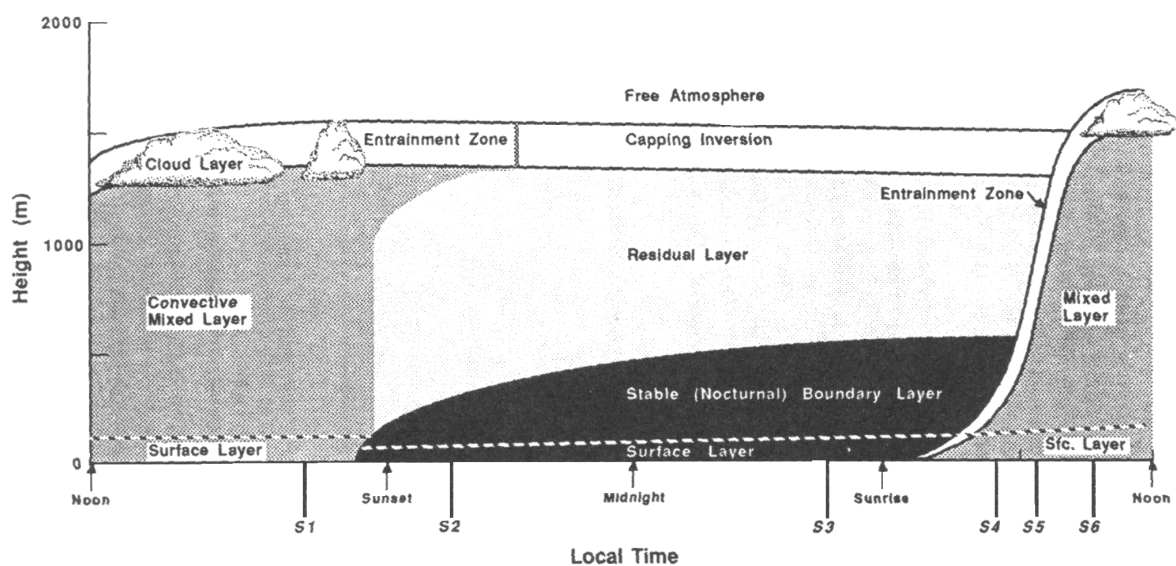


Figure 2-2: Schematic diagram of the diurnal evolution of the boundary layer over a plain in fair weather during summer. Time markers indicated by S1-S6 will be used in Figure 2-3 (Stull, 1988).

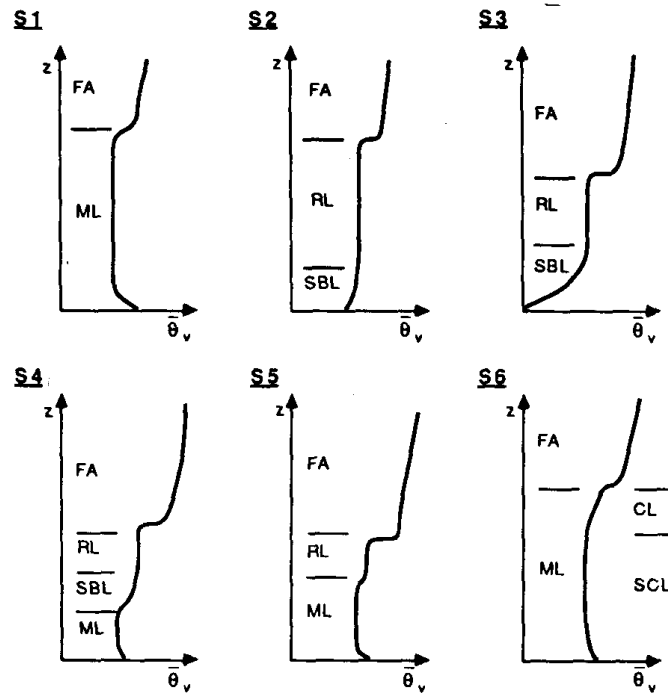


Figure 2-3: Profiles of mean virtual potential temperature $\overline{\theta}_v$, illustrating the boundary layer evolution during a diurnal cycle starting in the late afternoon. S1-S6 identify each sounding with an associated launch time indicated in Figure 2-2. (FA = free atmosphere, ML = mixed layer, RL = residual layer, SBL = stable boundary layer, CL = cloud layer, SCL = subcloud layer) (Stull, 1988).

2.3.1 The convective boundary layer (CBL)

In Figure 2-3 the profile of the mean virtual potential temperature $\overline{\theta}_v$ in a well developed convective boundary layer in the afternoon is shown (profile S1). Throughout the mixed layer, the virtual potential temperature is nearly constant. By approximation, this also holds true for humidity and pollutants as well as for wind speed and wind direction. Even though mixing can also be generated mechanically by wind shear, buoyant turbulence is the dominating process in a CBL which is caused by thermal heating due to strong solar radiation.

The evolution of the CBL is illustrated in Figure 2-2 and the corresponding profiles of mean virtual potential temperature during the period of a growing CBL are found in Figure 2-3 (S4 – S6). The daily cycle of a CBL can be divided into four phases (Stull, 1988; Seibert et al., 1998). The first stage is the formation of a shallow mixed layer (ML). This process is comparably slow with growth rates in the order of 10 to 100 m h⁻¹ as the strong nocturnal surface inversion caps the growing ML until this inversion is completely destroyed (see profile S4) (Seibert et al., 1998). By the time the increasing ML has reached the base of the residual layer (RL), the second phase of rapid ML growth starts (see profile S5). Until the ML has reached the capping inversion, growth rates of 100 to 1000 m h⁻¹ can be observed as there is virtually no stable layer that covers the ML. The following phase is characterised by a relatively constant ML depth that only experiences slow changes caused

by entrainment and subsidence and lasts most of the afternoon until shortly before sunset. The final depth varies largely amongst different regions of the world but is typically in the order of 1 to 2 km over land in mid-latitudes (Stull, 1988). In the fourth stage a stable layer starts to develop at the surface and turbulence decreases in the ML, converting the convectively driven ML into an elevated residual layer.

The depth of the convective mixed layer z_i marks the depth with the most negative heat flux and the strongest capping inversion, which is near the middle of the entrainment zone (Stull, 1988).

2.3.2 The stable boundary layer (SBL)

A stable boundary layer (SBL) starts to develop in the evening hours with the gradual build up of a near-surface temperature inversion with strongest temperature gradients near the ground (profiles S2 and S3 in Figure 2-3). The determination of the top of the stable layer from profiles of virtual potential temperature is complicated due to the smooth transition of the SBL to the RL (Stull, 1988).

In the SBL, turbulence is mainly produced mechanically by wind shear. It might be strong and continuous, but it can also be patchy, weak and intermittent. Seibert et al. (1998, 2000) subdivide the SBL into two layers: a layer of sporadic or intermittent turbulence and an inner layer of continuous turbulence, which was further used as the scaling height h for the SBL. Often the depth of the SBL is defined as the height where turbulence intensity is a small fraction of its surface value (Stull, 1988).

Close to the ground, wind speeds in a SBL are often light or even calm. Frequently, a pronounced maximum of wind speed occurs near the top of the stable layer, sometimes reaching values greater than the geostrophic wind speed, which is referred to as nocturnal low-level jet (LLJ) (Stull, 1988). In mid-latitudes a LLJ occurs typically between 100 and 300 m agl and is most pronounced 4-7 hours after sunset, showing a steady clockwise turning (northern hemisphere) of the wind vector (Seibert et al., 1998). During the night the LLJ descends to smaller altitudes and increases in strength (Beyrich, 1994).

2.3.3 The atmospheric boundary layer in complex terrain

Over horizontally homogeneous flat terrain the development of the ABL is largely understood. In complex terrain, however, interactions between the terrain and the overlying atmosphere can cause different transport and mixing processes, which may result in a different picture of the ABL evolution (e.g. De Wekker, 2002; Kalthoff, 1998). Mostly, thermally induced wind systems influence the structure of the ABL in complex terrain.

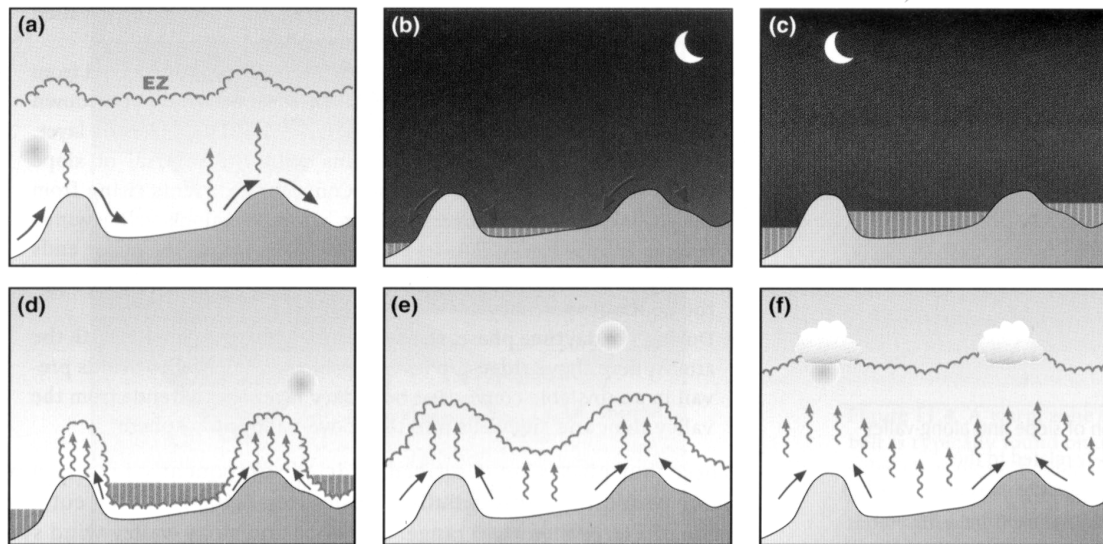


Figure 2-4: Temperature and wind structure evolution over a valley cross section during the course of a day focussing on the slope wind system. Lines with arrows indicate slope flows, wavy vertical lines with arrows indicate convective currents, the grey fill represents the valley inversion, and the scalloped line marks the entrainment zone at the top of the CBL (Whiteman, 2000).

Results from various studies were summarised in a conceptual model of the diurnal evolution of the ABL over mountainous terrain (Figure 2-4; Whiteman, 2000; De Wekker, 2002). Four phases were distinguished by Whiteman (2000). During the evening transition period (Figure 2-4 (a) and (b)), cold air drains off the mountains and collects in the valleys, forming stable inversions. In a valley, downslope and down-valley winds develop in this period. The night time phase (Figure 2-4 (c)) is characterised by decoupling of the valley atmosphere from the atmosphere above the ridge top and down-valley winds. Figure 2-4 (d) and (e) show the morning transition phase, which was described by a more detailed conceptual model by Whiteman (1982). After sunrise, upslope winds develop and transport mass and heat along the sidewalls. Convection due to surface heating creates a shallow CBL at the valley floor through destroying the inversion from below. To compensate the removal of mass from the valley floor, the stable core is forced to sink deeper into the valley. The subsiding air is warmed adiabatically, causing an increase in temperature over the entire valley atmosphere and small growth rates of CBL height. Finally, the stable core is destroyed and the development of the CBL can proceed much faster than over the mountain ridges. At the end of the morning transition phase, the CBL more or less follows the terrain (Figure 2-4 (e)). The valley atmosphere and the atmosphere above ridge-top level are coupled during the daytime phase and the CBL may become level (Figure 2-4 (f)). Prevailing winds in the CBL are upslope and up-valley winds during this period.

Numerous studies have dealt with the ABL structure in valleys and basins (e.g. Whiteman, 1982; Banta, 1984; Kuwagata and Kimura, 1995; Baumann-Stanzer and Groehn, 2004; Chemel and Chollet, 2005). These studies mainly confirmed the conceptual model, even though the boundary layer structure was often more complex than in the

conceptual model. Frequently, distinct layering was observed in the vertical potential temperature profile (Kossmann et al., 2002; De Wekker et al., 2005). One topic of research was the relationship between the upslope flow depth and the CBL depth. Even though most studies found the upslope flow to fill the whole CBL depth, Reuten et al. (2005) observed a closed slope-flow circulation within the CBL. Other mesoscale circulations like sea and land breezes have an influence on the ABL as well. Lieman and Alpert (1993) reported ABL heights over coastal regions being shallower than inland ABLs and stressed the impact of the interaction of the large-scale flow with the sea breeze on the ABL structure. Kossmann et al. (2002) observed interacting multi-scale wind systems ranging from microscale slope winds to mesoscale coast-to-basin flows that have an impact on the temporal and spatial variation of the ABL.

In the Upper Rhine valley which is a very large valley surrounded by mountainous regions (Black Forest), the TRACT ('Transport of air pollutants over complex terrain') experiment was carried out (Kalthoff et al., 1998; Kossmann et al., 1998). During this study, the top of the CBL above the mountains east of the valley was observed to remain small, which was attributed to synoptic westerly winds that force the capping inversion towards the mountain ridge and suppress the growth of the CBL. The heat budget of the CBL in this region was influenced by up-slope winds due to advection of cold air, leading to smaller growth rates of the CBL in regions where upslope winds occur (Kalthoff et al., 1998). Kossmann et al. (1998) studied the temporal evolution and spatial variation of the CBL on the meso- β scale and found a large influence of the underlying orography to the CBL growth. In the morning, the ABL followed the shape of the terrain, whereas this dependence got less during the course of the day. Kalthoff et al. (1998) pointed out that the spatial scale is important, as a horizontal CBL-top was observed over hilly terrain whereas larger-scale terrain structures induced a non-horizontal CBL top. Air was transported from the boundary layer to the free atmosphere in horizontal direction (advective venting) through the inversion step caused by the interaction of the slope wind system and the large scale winds above the western slopes of the Black Forest (Kossmann et al., 1999).

The CBL was observed to follow the terrain over a high mountain range, following the terrain less in the afternoon (De Wekker et al., 2004). Contrasting to observations in flat terrain, aerosol-layer heights and CBL heights were not equal. Over this mountain range aerosol-layer heights from a down-looking lidar were higher and more uniform than CBL heights. This discrepancy was attributed to mountain venting processes caused by thermally driven flows.

Methods and theories for the ABL height as introduced in the following sections are, strictly speaking, only valid for homogenous and more or less flat terrain. Nevertheless, as hardly any methods exist that are specific to complex terrain, these methods were applied in this study and their applicability was tested in complex terrain.

2.3.4 The atmospheric boundary layer height

In pollution meteorology commonly used terms are “mixed layer” or “mixing layer”. In this thesis “mixed layer” is only used in the context of a convective boundary layer which is well-mixed under sufficiently convective conditions. Beyrich (1997) and Seibert et al. (1998, 2000) defined the term “mixing layer” in the context of dispersion modelling. This expression was used for stable as well as for convective conditions for the turbulent layer adjacent to the ground. They preferred the term “mixing layer” because it stresses not the result but the process, as complete mixing can often not be observed during stable conditions. Their definition for the mixing height, which is used as a guideline in their study, was:

“The mixing height is the height of the layer adjacent to the ground over which pollutants or any constituents emitted within this layer or entrained into it become vertically dispersed by convection or mechanical turbulence within a time scale of about an hour.”

Attention has to be paid concerning the term mixing layer. Recently, this term was used in the context of turbulence in plant canopies (Raupach et al., 1996; Finnigan, 2000). It was found that canopy flows resemble features of plane mixing layers known from engineering applications, which gave rise to the canopy-mixing layer analogy. Nevertheless, the term mixing layer is still used in studies dealing with ABL heights (e.g. Emeis and Türk, 2004; Wiegner et al., 2006).

Beyrich (1997) discusses the relationship between the terms mixing height and ABL-height. As the definition of mixing height is based on the vertical mixing of pollutants, these two terms can be used equivalently if the ABL-height definition is based on turbulence parameters. Frequently vertical profiles of mean atmospheric parameters are used as criteria to estimate the ABL-height. In these cases, the two terms can only be considered equivalent if convective or mechanical turbulence governs the structure of the ABL.

In this thesis, the term ABL height is applied as various methods, including profile methods, are used for the determination of the ABL height. A distinction is drawn between the stable boundary layer and the convective boundary layer, which is reflected in the use of the terms CBL height and SBL height. More precisely it is distinguished between the depth and the height of the ABL (Kossmann et al., 1998; de Wekker, 2002). The ABL height is defined as the height of the ABL above sea level (asl) and the depth of the ABL as the height of the ABL above ground level (agl). Especially in complex terrain the correct use of these terms is important.

There are many different definitions of ABL heights found in literature which shows practical and theoretical problems of finding an overall valid definition (for a selection of definitions see Seibert et al. (1998)). Definitions of the ABL height often depend on the database available. In general, defining the CBL height is more straightforward than the

SBL height. In the following section a short introduction to methods for an experimental determination of the ABL height is given. In section 3.3 the techniques used in this thesis are described in further detail, together with the corresponding definition of the ABL height. Sections 2.3.4.2 and 2.3.4.3 deal with parameterisations for the SBL depth and a model for the CBL depth, each including definitions for the respective ABL depth.

Symbols used in the following are h for the SBL depth and z_i for the CBL depth.

2.3.4.1 The ABL height determined from measurements

Seibert et al. (1998, 2000) and Beyrich (1997) reviewed methods for ABL height determination from measurements. Measuring platforms can be divided into two groups. On the one hand, direct measuring techniques and sensor platforms are the most common techniques, on the other hand, aircraft and remote sensing techniques are becoming prevalent. Direct measurements are made by radiosondes, tethered balloons and masts. Remote sensing techniques such as doppler weather radar/wind profiler, lidar and sodar can be applied to measure ABL heights. Four requirements for vertical profiles of atmospheric parameters were stated by Beyrich (1997):

- The profiles should reach a height of 2-3 km above ground.
- The vertical resolution should be about 10-30 m to avoid uncertainties.
- A good time resolution of 1 h or less is required to describe the evolution of the CBL.
- Parameters characterising the intensity of turbulence or the result of the mixing process are preferred.

In this study, data from radiosonde and tethered balloon ascents as well as sodar data is used for ABL height determination. In the following, these measuring systems are introduced as well as advantages and shortcomings mentioned (after Seibert, 1998, 2000). Radiosoundings are a widely distributed tool for operational ABL height determination. Data from routine ascents are available from all over the world, usually providing 2-4 soundings per day. Such a low time resolution is a disadvantage for detailed ABL height determinations, as well as the fast ascents that only provide “snapshot”-like profiles with a low vertical resolution (Beyrich and Görndorf, 1995). In contrast, tethered balloon measurements make profiles with high vertical resolution and a better time resolution available. In addition to the measurements of standard meteorological parameters, turbulence and trace gas concentration measurements are possible. Shortcomings of this measuring platform are the limited measurement range, limitations of operation in cases of high wind speed or strong turbulence and the high personnel expense as no unmanned operation is possible. Continuous operation as well as the fact that remote sounding systems do not cause any modifications of the investigated flow make these systems valuable tools for probing the ABL. Sodar is a relatively simple, not very expensive system that provides profile data with high temporal and vertical resolution. One disadvantage is

the limited sounding range (500-1000 m). Sensitivity to environmental noise and noise pollutions are additional shortcomings for the operation of a sodar.

It can be seen that none of the systems described above is able to meet all the requirements. Beyrich (1997) illustrates this problem and says that “the ‘Mixing height-meter’ does not exist”. To overcome this problem he suggests the integration of different instruments into a complex sounding system. But this may be problematic as well as ABL heights inferred from different measurement systems may deviate a lot due to different criteria and methods. Numerous comparison studies can be found in literature, revealing ambiguous results. Sound agreement between different measurement systems was found especially in cases with a well defined inversion during a clear CBL evolution, while considerable deviations occur under stable situations (e.g. Coulter, 1979; Emeis et al., 2004; Beyrich and Görsdorf, 2005; Hennemuth and Lammert, 2006.; Wiegner et al., 2006).

Different criteria and methods exist to determine the ABL-height from the measured profiles. Beyrich (1997) summarises these criteria into two groups, one based on profiles of mean variables, the other one based on profiles of turbulent variables. In section 3.3 the criteria and methods applied in this study are explained in detail.

2.3.4.2 Parameterisations

In this section, parameterisations for the SBL height are introduced. The purpose of formulations for the SBL height are mainly for the use in models (Vickers and Mahrt, 2004). There are two types of relationships, namely diagnostic and prognostic equations. Even though prognostic equations seem to be more reliable, comparisons of different diagnostic and prognostic relationships with observations did not reveal big differences in the performance of these equations (Seibert et al., 1998). Diagnostic equations are either in the form of Richardson number relationships or are based on surface layer measurements, mainly requiring turbulent heat and momentum fluxes at the surface. Here, several diagnostic relationships based on surface layer measurements were tested. The selection of equations was based on a paper by Vickers and Mahrt (2004), with additional equations from other studies. Equations from the paper by Vickers and Mahrt (2004) are labelled by VM and the number of the equation in their paper in addition to the general numeration, which will be used in section 4.4.4 of the results.

The most simple equation tested was suggested by Koracin and Berckowicz (1988). It considers only the influence of friction (surface friction velocity u_*):

$$h = 700 \cdot u_* \quad (2-6)$$

Rossby and Montgomery (1935) additionally regarded the influence of the earth’s rotation on the boundary layer depth, expressed by the Coriolis parameter f (VM(1)):

$$h = C_n \frac{u_*}{f} \quad (2-7)$$

C_n is a nondimensional coefficient, having a value of 0.1 to 0.5.

Kitaigorodskii (1960) proposed a formulation that takes the Obukhov length L^* as the only appropriate length scale into account (VM(2)):

$$h = C_s L^* \quad (2-8)$$

The Obukhov length L^* is calculated with the following equation, which does not include the von-Kármán-constant κ . B_s is the scaled surface buoyancy flux.

$$L^* = \frac{-u_*^3}{B_s} \quad \text{and} \quad B_s = \left(\frac{g}{\theta} \right) \overline{w'\theta_v'} \quad (2-9)$$

Here, g is the acceleration due to gravity, θ is the potential temperature and $\overline{w'\theta_v'}$ is the buoyancy flux. The dimensionless coefficient C_s widely varies from 100 to 1.

Zilitinkevich (1972) suggested an equation incorporating the influences of the Coriolis parameter and the surface flux, which has been a very popular equation in observational and modelling studies (VM(3)):

$$h = C_{sr} \frac{u_*^2}{\sqrt{-fB_s}} \quad (2-10)$$

with the nondimensional coefficient C_{sr} ranging at 1.

Pollard et al. (1973) incorporated friction, the Earth's rotation, and the freeflow stratification N in their relationship (VM(4)):

$$h = C_{ir} \frac{u_*}{\sqrt{fN}} \quad (2-11)$$

The nondimensional coefficient C_{ir} has a value of 1.7.

N is the buoyancy frequency in the free atmosphere just above the boundary layer, also called Brunt-Väisälä frequency, and is incorporated to estimate the influence of stratification on entrainment at the top of the boundary layer. N is calculated from the temperature gradient, which requires information of the temperature profile or at least temperature information at two points above the boundary layer.

$$N^2 = \left(\frac{g}{\theta} \right) \frac{\partial \theta}{\partial z} \quad (2-12)$$

A similar relationship was proposed by Kitaigorodskii and Joffre (1988), only incorporating surface friction and background stratification (VM(5)):

$$h = C_i \frac{u_*}{N} \quad (2-13)$$

The nondimensional coefficient C_i ranges between 4 and 20.

Zilitinkevich and Mironov (1996) deduced two multi-limit equations for the SBL height by inverse interpolation of relevant SBL height scales. The first one reads as (VM(6)):

$$\left(\frac{fh}{C_n u_*}\right)^2 + \frac{h}{C_s L^*} + \frac{Nh}{C_i u_*} = 1 \quad (2-14)$$

Their second equation incorporates two additional terms that take cross interactions between the parameters determining the SBL height into account (VM(7)):

$$\left(\frac{fh}{C_n u_*}\right)^2 + \frac{h}{C_s L^*} + \frac{Nh}{C_i u_*} + \frac{h\sqrt{f}}{C_{sr}\sqrt{u_*}L^*} + \frac{h\sqrt{Nf}}{C_{ir}u_*} = 1 \quad (2-15)$$

Nieuwstadt (1981) suggested the following equation (VM(8)):

$$\frac{h}{L} = \frac{0.3u_* / (fL)}{1 + 1.9h/L} \quad (2-16)$$

Here, the Obukhov length includes the von-Kármán-constant:

$$L = \frac{-u_*^3}{\kappa \left(\frac{g}{\theta}\right) w' \theta'_v} \quad (2-17)$$

Other equations were proposed by Deardorff (1972) (VM(9)):

$$h = \left(\frac{1}{30L^*} + \frac{f}{0.35u_*}\right)^{-1} \quad (2-18)$$

and by Businger and Arya (1974) (VM(10)):

$$h = \sqrt{\frac{\kappa u_* L^*}{f}} \quad (2-19)$$

A new multi-limit equation was derived by Zilitinkevich et al. (2002) from the momentum equations, implicitly accounting for the turbulence kinetic energy (TKE) budget (VM(11)):

$$h = \frac{C_R u_*}{f} \sqrt{1 + \frac{C_R^2 u_*^2 (1 + C_{UN} L^* N / u_*)}{C_s^2 f L^*}} \quad (2-20)$$

This formulation is one of the diagnostic formulations recommended by Zilitinkevich and Baklanov (2002) for more accurate SBL height calculations within one-dimensional and three-dimensional models. Coefficients have the following values: $C_R = 0.4$, $C_s = 0.75$ and $C_{UN} = 0.25$. The coefficient C_{UN} was newly estimated by Sodemann and Foken (2004) for a dataset for Antarctica. Their estimates were higher than the one given by Zilitinkevich et al. (2002), having a value of $C_{UN} = 0.51$ for katabatic outflow conditions and $C_{UN} = 2.26$ for strong wind conditions. The first coefficient was tested in this study as well and will be named VM(11/2) in the results.

In addition to the formulations reviewed by Vickers and Mahrt (2004), two diagnostic

equations developed by Steeneveld et al. (2006a) were applied. Formal dimensional analysis with the same quantities as in the multi-limit equations ((2-14), (2-15)) was performed. Their diagnostic equation for the stable boundary layer height reads as (SWH(3)):

$$h = L \left(\frac{\left| \frac{g}{\theta} \overline{w' \theta'_v} \right|}{\alpha u_* f N L} \right)^\lambda \quad (2-21)$$

with $\lambda = \left(C_1 - 0.001 \frac{N}{f} \right)^{-1}$, $\alpha = 3$, and $C_1 = 1.8$.

As the relevance of f was discussed in recent literature, Steeneveld et al. (2006a) performed a principal component analysis to get insight into the relative impact of the different quantities on the SBL height. The Coriolis parameter f appeared to be relatively unimportant. Therefore, a dimensional analysis was performed ignoring this variable. Two regimes were observed from the data. The resulting diagnostic equation reads as (SWH(4)):

$$\begin{aligned} h &= \frac{10u_*}{N} & \text{for } \frac{u_*^2 N}{B_s} > 10 \\ h &= 32 \sqrt{\frac{B_s}{N^3}} & \text{for } \frac{u_*^2 N}{B_s} < 10 \end{aligned} \quad (2-22)$$

Handorf et al. (1999) studied the SBL over an Antarctic ice sheet. They tested equation (2-14) (Zilitinkevich and Mironov, 1996) and developed the following equation (HFK(19)):

$$\frac{1}{C_n} \frac{h|f|}{u_*} + \frac{1}{C_{sr}^2} \frac{h}{L^*} \frac{h|f|}{u_*} + \frac{1}{C_{ir}^2} \frac{hN}{u_*} \frac{h|f|}{u_*} = 1 \quad (2-23)$$

Applying the dimensionless coefficients listed in Table 2-1, they yielded realistic equilibrium heights of the SBL with both equations. These coefficients were used in this study in equation (2-14), named VM(6/2) in the results section, and in equation (2-23).

In Table 2-2 dimensionless coefficients as they were applied by Vickers and Mahrt (2004) and Steeneveld et al. (2006a) are listed. These coefficients were used in this study for all equations except of equation (2-23).

Generally, the introduced parameterisations were developed for horizontally homogeneous stably stratified boundary layers. Even though this is not the case in this study, where the terrain is complex and land use heterogeneous, parameterisations are tested without any modification.

Table 2-1: Dimensionless coefficients from Handorf et al. (1999) for the use in (2-14) and (2-23).

C_n	C_s	C_i	C_{sr}^2	C_{ir}^2
0.5	12	9.05	0.14	0.115

Table 2-2: Dimensionless coefficients from the literature (after Vickers and Mahrt, 2004; Steeneveld et al., 2006a).

C_n	C_s	C_i	C_{sr}	C_{ir}	C_R	C_S	C_{UN}	α	C_1
0.1	10	11	1	1.7	0.4	0.75	0.25	3	1.8

2.3.4.3 Slab models

A so-called slab or jump model is used to calculate the evolution of the depth of the convectively mixed ABL over a horizontally homogeneous area (Tennekes, 1973; Tennekes and Driedonks, 1981; Stull, 1988; Yi, 2001). This model makes the assumption of constant values of potential temperature, specific humidity and momentum with height within the mixed layer (Figure 2-5), thus assuming sufficient turbulence to maintain this distribution. At the top of the mixed layer z_i a jump in these variables marks the transition to the free atmosphere. $\Delta\theta$ is the temperature jump at the top of the mixed layer and depicts the inversion strength. The air above the mixed layer is stable, with a vertical gradient of potential temperature γ that is taken to be independent of height and time. Within the mixed layer the turbulent heat flux is assumed to be linear with height, with a jump at the top. At the inversion base a downward turbulent heat flux $(\overline{w'\theta'})_i$ occurs due to the entrainment of warm air into the cooler boundary layer. In this model, the entrainment zone is assumed to be infinitesimally thin.

Due to the linear dependence of the turbulent heat flux $\overline{w'\theta'}$ on the height z , the mixed layer heats up uniformly. Changes in the mixed-layer temperature θ_m are described as

$$\frac{\partial \theta_m}{\partial t} = \frac{1}{z_i} \left[(\overline{w'\theta'})_s - (\overline{w'\theta'})_i \right] \quad (2-24)$$

where s and i depict values at the surface and height z_i , respectively.

From the continuity equation the entrainment velocity w_e can be written as

$$w_e = \frac{dz_i}{dt} - \overline{w} \quad (2-25)$$

Here \overline{w} is the mean large-scale vertical motion at the top of the mixed layer which is negative for subsidence. Subsidence is usually neglected in these models and the mean large-scale vertical motion \overline{w} is set to zero.

The behaviour of the potential temperature jump is governed by two processes. On one hand, inversion strength $\Delta\theta$ decreases as the mixed layer is heated, on the other hand entrainment increases $\Delta\theta$ at the rate γw_e .

The net rate of change is

$$\frac{d}{dt} \Delta\theta = \gamma \frac{dz_i}{dt} - \frac{\partial \theta_m}{\partial t} . \quad (2-26)$$

At the interface between the mixed layer and the air above, heat is transported into the mixed layer by entrainment as the inversion base rises. This amount of heat has to be carried away by a heat flux into the boundary layer. Therefore the downward heat flux at the inversion base can be written as

$$-\overline{(w'\theta')}_i = \Delta\theta \cdot \frac{dz_i}{dt} . \quad (2-27)$$

The influence of radiative fluxes as well as the influence of shear are neglected in this model.

The formulas above are solved by the use of the so-called flux ratio-method (Seibert et al., 1998), which is a parameterisation of the heat flux at the mixed layer top through the surface heat flux. From the budget for turbulence kinetic energy (TKE) a constant heat flux ratio is derived as (Tennekes, 1973)

$$-\overline{(w'\theta')}_i = c \overline{(w'\theta')}_s . \quad (2-28)$$

Gryning and Batchvarova (1990a, 1990b) not only considered the buoyancy production of TKE but also the mechanical production of TKE within the boundary layer. Then the downward directed heat flux at the inversion reads as

$$-\overline{(w'\theta')}_i = c \overline{(w'\theta')}_s + \frac{Bu_s^3 \theta_m}{gh} \quad (2-29)$$

where c is the entrainment constant and B a parameterisation constant. Different values of c and B can be found in the literature. Tennekes (1973) suggested $c = 0.2$ and $B = 2.5$. These values were applied in this study as well.

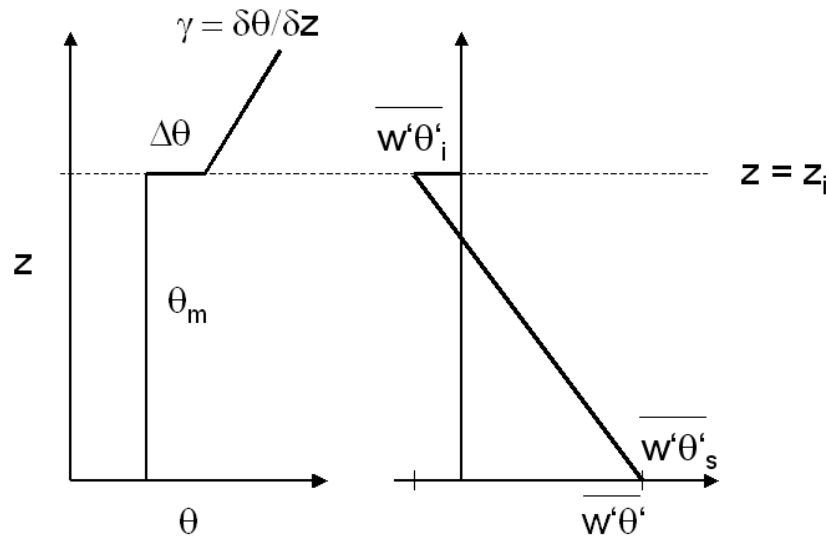


Figure 2-5: The profile of potential temperature and heat flux distribution in a slab model (modified after Tennekes and Driedonks, 1981).

Solving the equations above, differential equations for z_i can be deduced. The simpler form of heat flux parameterisation (2-28) results in (Betts, 1973)

$$\frac{dz_i}{dt} = (1 + 2c) \frac{(\overline{w'\theta'})_s}{\gamma \cdot z_i} \quad (2-30)$$

Gryning and Batchvarova (1990b) yielded with (2-29)

$$\frac{dz_i}{dt} = \frac{(1 + 2c)w_*^3 + 2Bu_*^3}{\gamma \left(\frac{g}{\theta_m} \right) z_i^2} \quad (2-31)$$

The convective scaling velocity w_* is calculated as

$$w_* = \left(\frac{g}{\theta_m} z_i (\overline{w'\theta'})_s \right)^{\frac{1}{3}} \quad (2-32)$$

The differential equation (2-30) can be solved when neglecting the initial value of z_i . Then a simple relationship to calculate the CBL growth writes (Schipper, 2002)

$$z_i = \sqrt{\frac{2(2c+1)}{\gamma} \int_0^t (\overline{w'\theta'})_s dt'} \quad (2-33)$$

It can be seen from (2-33) that the height of the mixed layer is proportional to the square root of the cumulative turbulent heat flux $(\overline{w'\theta'})_s$. From a large set of data obtained in Wisconsin, USA, from March through October of 1998, Yi et al. (2001) gained a least squares linear fit following:

$$z_i = a + b \sqrt{\int_0^t (\overline{w'\theta'})_s dt'} \quad (2-34)$$

They yielded $a = 97.1$ m and $b = 25.537 \text{ K}^{-1/2} \text{ m}^{-1/2}$ by fitting profiler-measured convective boundary layer heights z_i and flux measurements from a sonic anemometer ($r^2 = 0.98$). From these values the lapse rate can be estimated as $\gamma \approx 4.3 \text{ K km}^{-1}$. As the equations derived above are only valid until the mixed layer reaches its maximum depth, Yi et al. (2001) assume that z_i may be calculated by integrating (2-34) to 2 h after the turbulent heat flux $(\overline{w'\theta'})_s$ reaches its maximum.

Schipper et al. (2002) derived a similar relationship from a measurement period of 10 days in June and July 1999 in Tennessee, USA. Fitting boundary layer heights measured by a wind profiler against the square root of cumulative surface buoyancy flux H (energetic units) they gained $a = 150$ m and $b = 0.61 \text{ s kg}^{-1/2} \text{ m}^{-1}$ ($r^2 = 0.55$). In their study they got $\gamma \approx 7 \text{ K km}^{-1}$.

The relatively simple relationships (equation (2-33) and equation (2-34) using a and b from the studies by Yi et al. (2001) and Schipper et al. (2002)) as well as the model following Gryning and Batchvarova (1990b) (equation (2-31)) were tested in this study.

Several equations have been proposed by various authors as solutions to the slab model based on different considerations of the terms in the TKE budget and their parameterisations (for an overview see Seibert et al., 1998). Seibert et al. (1998, 2000) recommend the use of models that take the mechanical contribution to CBL growth into account in addition to the consideration of surface heating, such as the equation proposed by Gryning and Batchvarova (1990b).

3 Data and methods

Within this chapter, the data and methods that were used in this study are introduced. The first section describes the SALSA 2005 project. In the following section, the used data from various measurement systems is shortly outlined. Methods for the determination of the boundary layer height are dealt with in the third section of this chapter. The last two sections address the input data for the parameterisations and the slab models as well as statistical measures to evaluate model performance.

3.1 SALSA 2005

The aim of the project SALSA 2005 ('Beitrag von Salpetriger Säure zur atmosphärischen OH-Konzentration'), carried out in August and September of 2005, was to study the contribution of nitrous acid (HONO) to the atmospheric OH-concentration. To get a better understanding of possible transport mechanisms, not only chemical measurements of OH, nitrous acid and other trace gases were made at the mountain site and at its base but also meteorological, turbulence and profile measurements to characterise the flow conditions and possibly arrive at a budget for nitrous acid.

3.1.1 Investigation area

The SALSA 2005 project was carried out at and around mount Hohenpeißenberg, a mountain in the Bavarian Alpine foreland that has a maximum elevation of 989 m asl. Hohenpeißenberg is situated 20 km north of the Alpine margin and about 60 km southwest of Munich in a landscape stamped by moraines (Figure 3-1).

The mountain overtops the surrounding hilly terrain by about 300 m, is aligned in an east-west direction and has a length of 4.5 km and a width of 1.5 km at its base. The mean elevations of the surroundings to the north, west and south are 700 m asl. South of Hohenpeißenberg, the river Ammer forms a deep canyon-like valley with a bottom height of 620 m asl extending from east to west. East of Hohenpeißenberg there is a sharp decline of height to the town of Peißenberg (590 m asl), which lies in a flat area associated with Lake Ammersee in the north. Figure 3-2 and Figure 3-3 illustrate the main topographic features of the region.

Land use in the investigation area is quite heterogeneous. There are two major urban settlements in the vicinity of the mountain, the villages of Hohenpeißenberg in the south and Peißenberg in the east. South of Hohenpeißenberg the major land use is forest, whereas mount Hohenpeißenberg itself and the surroundings to the north and west are characterised by patches of forest and agricultural land (mainly meadows).

From this site description, it can be concluded that different types of terrain inhomogeneities exist (land use, terrain height) that are expected to cause a complex structure of the ABL.

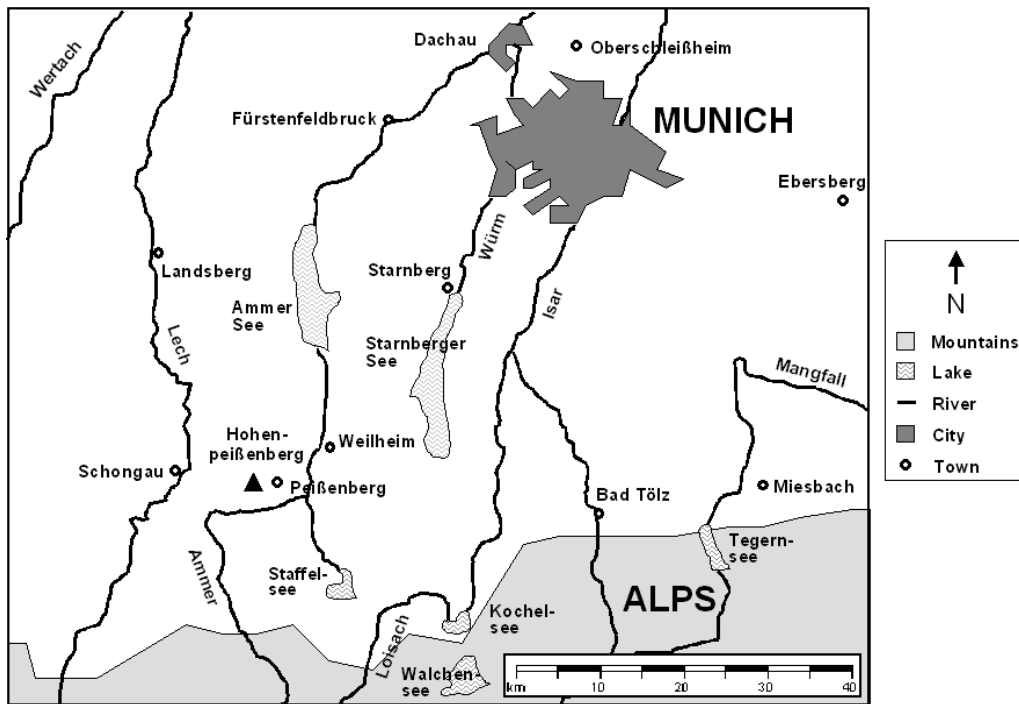


Figure 3-1: Map of the Alpine foreland and the northern Alps. Hohenpeißenberg is indicated with a black triangle (modified after Top50 Viewer, Topographische Karte 1 : 1 000 000 Bundesrepublik Deutschland).

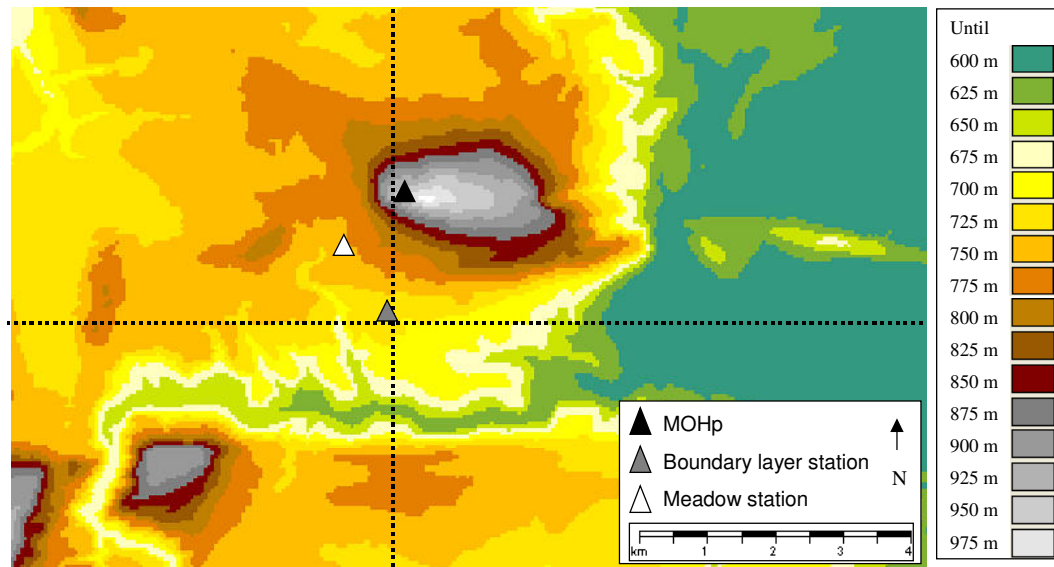


Figure 3-2: Contour map of mount Hohenpeißenberg and its surroundings, dotted lines mark profiles shown in Figure 3-3 (adapted from Top50 Viewer, Topographische Karte 1 : 50 000 Bayern (Süd)).

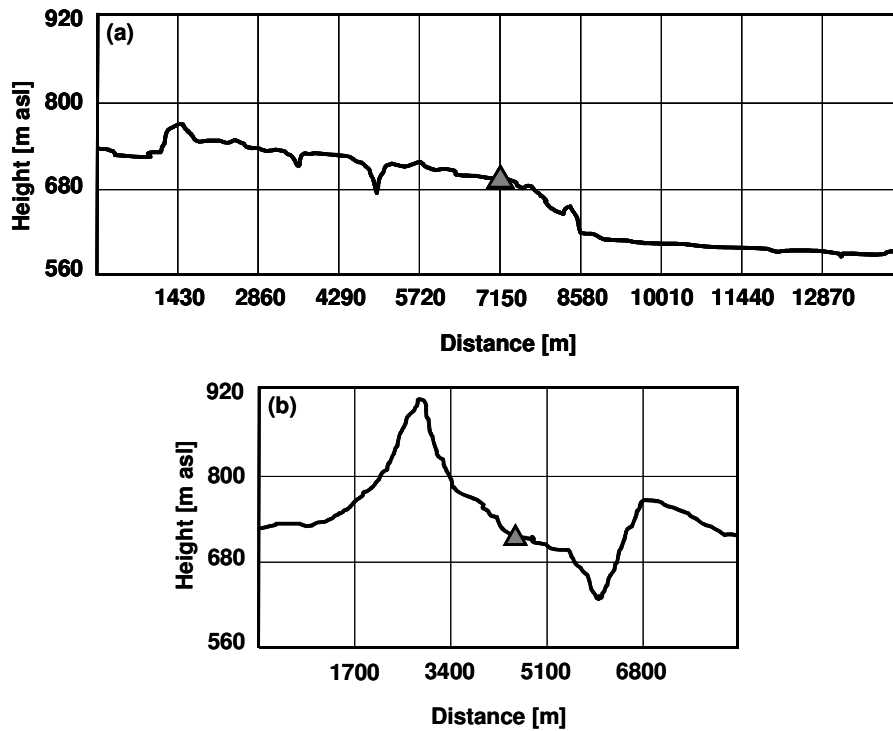


Figure 3-3: W-E-profile (a) and N-S-profile (b) as indicated in Figure 3-2 (adapted from Top50 Viewer, Topographische Karte 1 : 50 000 Bayern (Süd)).

3.1.2 Measuring stations

The meteorological observatory of the German Meteorological Service (DWD) on top of mount Hohenpeißenberg (977 m asl), which is also a GAW station (Global Atmosphere Watch of the World Meteorological Organization), provides routinely measured meteorological as well as chemical data. The Meteorological Observatory Hohenpeißenberg (MOHp) is located at the western edge of the mountain, which is the smallest and steepest part of the mountain. Several measuring stations were set up around Hohenpeißenberg during the experiment (see Figure 3-2). 1.7 km south of the observatory and with a difference in elevation of 264 m, the boundary layer station (713 m asl) was set up at the lower end of the village of Hohenpeißenberg in a meadow. Measurement systems included a sodar/RASS system, a tethered balloon (meteorological parameters as well as CO_2 and O_3), an automatic weather station providing standard meteorological data and gas measurements (O_3 , CO_2 , NO , NO_x). At the meadow station (743 m asl), 1.1 km south-east of the observatory, eddy covariance, gradient and radiation measurements were carried out on a slightly sloped meadow. HONO was measured at this site during a certain period which was the main aim of the project. The horizontal distance between the meadow station and boundary layer station was 1.1 km and there was a difference in elevation of 30 m. Two additional stations were set up at the upper slopes of the mountain, one south of the observatory in the forest, the other one north of the observatory in an open meadow. Data from the latter two stations were not used in this study.

Table 3-1: Coordinates of the measuring stations.

Station	Height [m asl]	Latitude [N]	Longitude [E]
Boundary layer station	713	47° 47.15'	11° 00.36'
Meadow station	743	47° 47.70'	10° 59.87'
MOHp	977	47° 48.09'	11° 00.38'

3.2 Data

3.2.1 Meteorological Observatory Hohenpeißenberg (MOHp)

Meteorological data was provided by the Meteorological Observatory Hohenpeißenberg (MOHp). Standard meteorological measurements were made at 977 m asl, with wind measurements on top of a tower at the same location at a height of 1018.3 m asl.

3.2.2 Sodar/RASS

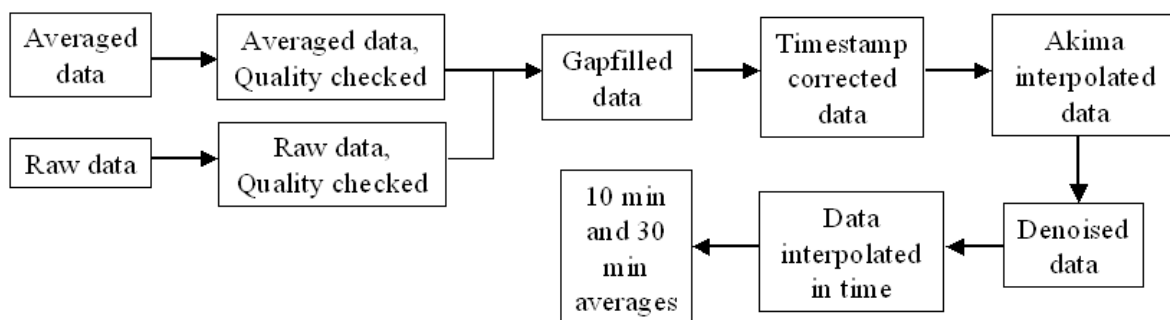
In this study a phased-array Doppler-sodar (model DSDPA.90/64, METEK Meteorologische Messtechnik GmbH) combined with a 1290 MHz RASS extension (METEK GmbH, for technical details see appendix) was run at the boundary layer station south of the village of Hohenpeißenberg. From 18 August 2005 until 26 August 2005 measurements were carried out at a location that appeared to be disturbed by the hum of a power supply line. Therefore, the sodar/RASS system was shifted 100 m to the south, where measurements were made from 27 August until 21 September 2005 without any major disturbances. At the first measuring location, preliminary frequency tests were conducted. On the one hand, a high sounding range was desired, on the other hand, fixed echoes had to be avoided. A fixed echo appears as an increased reflectivity at a distinct height, which continues to exist for a longer time period. The higher the frequency, the lesser the range of the measurements, because absorption increases with increasing frequency of sound waves (Crescenti, 1998). During the frequency tests, an increase in fixed echoes was observed with lower frequencies. Therefore, a compromise had to be found for a range as high as possible and a prevention of fixed echoes, which was achieved with a frequency of 1600 Hz. Due to problems which turned out to be caused by a power supply line, the frequency was increased the following days up to a frequency of 1663 Hz, which was used from 22 August 2005 until the measurement location was moved. At the second location no frequency tests were performed, because conditions of atmospheric turbulence were not expected to vary between the two locations. Instead, sounding parameters tested at the first location were adopted. To find the best frequency, frequency was gradually changed starting from 1663 Hz. A measuring frequency of 1725 Hz was then used from 3 September 2005 until the end of the experiment. Sounding parameters for both locations are summarized in Table 3-2.

Table 3-2: Sounding parameters for the continuous measurements at location 1 and location 2 during SALSA 2005.

Parameter	Location 1	Location 2
Acoustical frequency [Hz]	1663	1725
Minimum height [m]	40	40
Maximum height [m]	910	910
Noise height [m]	1100	1100
Height resolution [m]	20	20

Minimum height of the measurements was 40 m, maximum height was 910 m, with a height resolution of 20 m. The noise height, which is the height where the emitted sound pulse was indiscernible from the ambient noise in the acoustic spectra was set to 1100 m.

Until 30 August 2005 averaging time was 10 minutes, thereafter it was set to 5 min. Averaged data as well as raw data from each antenna circulation were saved by the sodar/RASS system. In addition to various parameters, an error code was generated by the measuring system for all range gates at each antenna, based on important properties of the backscattered spectra and the signal-to-noise ratio. The data was processed using a set of programs developed by Mayer (2005). Filtering of the data can either be done by the use of error codes or by the signal-to-noise ratio. In this study, the applied filters were set as following: reflectivity was not filtered at all, for wind speed, wind speed components, wind direction, standard deviations of wind speed and dispersion class the filtering criteria was a signal-to-noise ratio of higher than -3 dB and for temperature a stricter criteria based on error codes was used. Quality controlled data was handed over to further data processing steps (Figure 3-4), which are: the correction of the timestamps, gap filling by applying an interpolation (Akima, 1970) in space over a maximum gap of 100 m, denoising of the profiles and temporal interpolation over a maximum gap of 10 minutes.

**Figure 3-4: Data processing scheme of the sodar/RASS data (Mayer, 2005).**

3.2.3 Radiosondes

Radiosounding data from three stations in the vicinity of the experimental area were used to determine the ABL height. At the meteorological observatory on top of Hohenpeißenberg, a Vaisala RS92 radiosonde (for technical details see appendix) coupled with a Brewer/Mast ozonesonde is launched twice a week in the early morning hours (5 or

6 CET). Radiosonde measurements (Vaisala RS92) and pilotballoon measurements are made at Altenstadt, situated 12 km west of Hohenpeißenberg and 3 km northwest of Schongau (see Figure 3-1) by the German Federal Armed Forces more frequently. Depending on the day, radiosoundings and pilotballoons from Altenstadt provided data up to 4 times a day (4 CET, 7 CET, 10 CET, 13 CET). At Oberschleißheim (see Figure 3-1), situated north of Munich and about 60 km northeast of Hohenpeißenberg, regular Vaisala RS92 radiosonde launchings are made at 1 CET and 13 CET by the German Meteorological Service. Exact locations of these three radiosounding stations are summarized in Table 3-3.

Radiosondes provided meteorological parameters up to a height of about 35 km. These parameters consisted of temperature, pressure, relative humidity, wind speed and wind direction. The data was recorded as a series of distinctive points together with data for the major pressure levels. Using the distinctive points a good approximation of the shape of the profile is given. Due to the way of data recording, vertical resolution varied largely between 5 m and 1500 m and in the lower 5000 m between 5 m and 500 m. A radiosonde took about 5 to 6 min to sound the lowermost 2 km of the atmosphere. At Altenstadt not only radiosondes were launched but also pilotballoons, which had a much lesser vertical range and only provided wind data.

Table 3-3: Locations of radiosounding stations.

Station name	Height [m asl]	Latitude [° N]	Longitude [° E]
Altenstadt	756	47.83	10.87
Hohenpeißenberg	977	47.80	11.01
Oberschleißheim	484	48.24	11.55

3.2.4 Tethered balloon

Profiles of wind speed, wind direction, pressure, temperature and relative humidity were measured between the ground and 700 m agl by a tethered balloon with up to three tethersondes (Vaisala TS-5A-SP tethersonde, for sensor specifications see appendix) at the boundary layer site. One ascent took about 30 min (one-way). Tethered balloon ascents were conducted only on fair weather days in morning and evening hours. During the day, strong turbulence prohibited the operation of the tethered balloon. In addition to meteorological parameters, CO₂- and O₃-mixing ratios were measured occasionally. These profiles were not used in this study.

3.2.5 Turbulence measurements

Flux measurements by eddy covariance and radiation measurements were carried out at the meadow station, which was a slightly inclined grassland site. Flux measurements consisted of a sonic anemometer (CSAT3, Campbell Scientific, Inc.), an open path CO₂/H₂O-analyser (LICOR LI7500, Campbell Scientific, Inc.) and a fast temperature

sensor (AIR 150, platinum wire). The sampling frequency was 20 Hz and the measuring height was 2.1 m above the canopy. The software package TK2, developed at the University of Bayreuth (Mauder and Foken, 2004), was used to compute turbulent fluxes with their corrections and quality tests (quality flags after Foken et al., 2004). Averaging times of the resulting processed data were 30 minutes.

Radiation measurements were conducted at the same site, using upward and downward facing radiation sensors. Short wave radiation was measured by the pyranometer CM 21 (Kipp & Zonen, Netherlands) and long wave radiation by the Eppley PIR pyrgeometer (The Eppley Laboratory, Inc, USA). The measuring height was 2 m above ground.

See appendix for technical details of the measuring devices.

3.2.6 Lokal-Modell

Together with the Global-Modell the Lokal-Modell (LM) forms the operational numerical weather prediction (NWP) system of the DWD, which has been in use since the end of 1999 (Doms et al., 2005). It is a nonhydrostatic limited-area atmospheric prediction model, which is designed for operational numerical weather prediction as well as for various scientific applications on the meso- β and meso- γ scale. At present, the LM is run on the meso- β scale using a grid spacing of 7 km. Prognostic variables are horizontal and vertical wind components, pressure, temperature, specific humidity, cloud liquid water, cloud ice and turbulence kinetic energy up to a height of about 22 km. In addition to that, soil temperature and soil moisture as well as snow mass and interception water are predicted (Weissmann et al., 2005). Vertical resolution varies with height, being finer close to the surface and getting coarser higher up. Results from the operational mode of the LM at the DWD were used in this study. For every prediction hour, profiles of various variables were given for 35 layers, together with CBL and SBL heights. The scheme for the determination of the boundary layer height will be described in section 3.3.3. Data from two grid points was available. The coordinates of the grid points mark the south west corner of a 7 x 7 km-grid box. The first grid point, called Hohenpeißenberg1, is situated on the northern edge of the mountain (47.81°N, 11.01°E, 651.68 m asl). The second grid point, called Hohenpeißenberg2, is located south of the Ammer valley (47.75°N, 11.01°E, 710.18 m asl). All three measuring stations were situated in the grid box that is marked by the grid point Hohenpeißenberg2.

3.3 *Methods for the determination of the atmospheric boundary layer height*

3.3.1 Determination from sodar/RASS data

Using sodar data, the height of the ABL is primarily inferred from profiles of the acoustic reflectivity (Beyrich, 1997). As described above (section 2.2) the reflectivity is

proportional to the temperature structure parameter C_T^2 . This interrelationship can be used because certain typical characteristics of the vertical profiles of C_T^2 appear under stable and convective conditions (Seibert et al., 1998). Using profiles of reflectivity is advantageous because even the simplest one-antenna echo sounders provide this data and accurate quantitative data is not always necessary as the shape of the profiles is of major interest. In Beyrich (1997) and Seibert et al. (1998, 2000) overviews of methods and criteria for the determination of the boundary layer height from sodar data were given. At the top of a well-mixed CBL or slightly above it a pronounced secondary maximum is observed. Therefore, a clearly-defined criterion can be formulated in the CBL (Beyrich, 1997). In the SBL no such straightforward criterion can be applied. Beyrich and Weill (1993) reviewed some characteristic heights recommended in literature, like:

- Height of a (secondary) elevated maximum in reflectivity, if it is observed (R_{\max}).
- The level where the change in the vertical gradient within a zone of continuous decrease is most pronounced (i.e., maximum curvature in the reflectivity profile).

According to them, the least satisfying procedure is to determine the SBL height as the height where reflectivity has decreased below a certain threshold value. They concluded that the stage of the SBL-evolution has a large impact on the relationship between the SBL height from sodar data and any other height scale. Therefore, the actual shape of the profiles of reflectivity determines which criteria has to be used to derive the SBL height. This means that none of the suggested criteria is superior to the others for the duration of a whole night. Instead, the use of more than one criteria during one single night may be necessary. A distinction between three SBL types is made depending on their characteristic shapes of the reflectivity profile (Table 3-4).

Doppler sodars not only provide reflectivity data, but also profiles of the horizontal wind vector, vertical wind velocity (w) and vertical wind velocity standard deviation (σ_w). These profiles can also be utilised to determine the boundary layer height (see overview of criteria in Beyrich (1997)). Caution is advised for the use of w - and σ_w -data because the measurement accuracy is frequently in the range of the typical values of these parameters. Therefore, Beyrich (1997) suggested the use of these profiles only as an additional supporting criterion.

The methods described above require visual inspection of every single profile and may be a bit subjective. They require experience of the operator and sufficient time for off-line work (Asimakopoulos, 2004). Several attempts have been made to overcome these shortcomings and to develop automatic algorithms to determine the boundary layer height from sodar data. This is not a trivial problem and has not been solved satisfactorily so far (Foken et al., 1987; Beyrich, 1997; Keder 1999; Asimakopoulos, 2004). For example, Keder (1999) compared radiosonde data to sodar data, using the REMTECH-method to determine the ABL height from sodar data. His results were disappointing, which he attributed to errors in the automatic routine supplied by the sodar manufacturer.

Table 3-4: Criteria for boundary layer height estimation from sodar data in the stable and shallow convective boundary layer (Beyrich et al., 1996).

Shape of the reflectivity profile	Applied method
Continuous decrease with decreasing gradient	Maximum curvature of reflectivity profile
Nonmonotonous decrease	Maximum gradient of the reflectivity profile
Elevated maximum of reflectivity	Height of the elevated maximum

A comparatively easy approach has been suggested by Emeis and Türk (2004). Profiles of reflectivity and of the standard deviation of the vertical wind velocity component were used simultaneously to automatically determine the ABL height. Two criteria were utilized. The first one searches for a sharp decrease of the reflectivity R with height z . System specific threshold values are used herein:

$$H_1 = z, \text{ if } (R(z) < 88 \text{ dB and } R(z+1) < 86 \text{ dB and } R(z+2) < 84 \text{ dB}) \quad (3-1)$$

The top of a turbulent layer is usually marked by the height H_1 . Surface inversions and elevated inversions are identified by the second criterion that diagnoses (secondary) maximums of the reflectivity that are not associated with high turbulence intensities. This criterion consists of two steps. First, it looks for elevated inversions, which can be identified by an increase in reflectivity below a certain height $z = H_2$ and a decrease above:

$$H_2 = z, \text{ if } (\delta R/\delta z(z+1) < 0 \text{ and } \delta R/\delta z(z-1) > 0 \text{ and } \sigma_w < 0.7 \text{ m s}^{-1}) \quad (3-2)$$

Second, (usually nocturnal) surface inversions are recognised by:

$$H_2 = z, \text{ if } (R(z) > 105 \text{ dB and } \sigma_w < 0.3 \text{ m s}^{-1}) \quad (3-3)$$

Low σ_w -values are required to avoid cases of superadiabatic temperature profiles.

The algorithm determines H_1 and H_2 separately and starts with small heights z . As soon as the criterion is met the first time, the search stops. The ABL height (in their paper called height of the mixing layer MLH) is taken as the smaller value of H_1 and H_2 :

$$MLH = \min(H_1, H_2) \quad (3-4)$$

There are cases when no MLH can be determined as none of the criteria are fulfilled, as it may be observed when the CBL top is higher than the range of the sodar.

The combination of the sodar system with RASS additionally provides temperature profiles. Temperature data can be analysed by simply using standard evaluation known from radiosondes, as is explained in the next section (section 3.3.2). Sodar/RASS measurements supply simultaneous measurements of vertical profiles of wind and virtual temperature, which makes this data highly suitable for applying Richardson number methods for the SBL (Engelbart and Bange, 2002). In their study, reasonable results are obtained with a critical Richardson number $Ri_c = 0.35$ which proves the applicability of Richardson number methods to sodar/RASS data. Richardson number methods as typical methods to determine the ABL height from radiosoundings are described in section 3.3.2.

3.3.2 Determination from radiosonde and tethered balloon data

Radiosonde and tethered balloon ascents provide profiles of different meteorological parameters (temperature, humidity, wind). Various methods are used to determine the boundary layer height from these profiles. Again, a good overview of methods can be found in Seibert et al. (1998, 2000).

From the temperature profile, the CBL height is derived through the use of the parcel method (Holzworth, 1964, 1967), which is considered the most reliable method in convective situations (Seibert et al., 1998; Baumann-Stanzer and Groehn, 2004). Starting with the surface temperature, the dry adiabat is followed up to its intersection with the temperature profile. This means that the height of the CBL is taken as the equilibrium level of a hypothetical rising parcel of air with surface temperature. Because of the high dependence on the surface temperature, several refinements were suggested, namely adding an excess temperature to the surface (potential) temperature (advanced parcel method), as calculated in Troen and Mahrt (1986) and Holtslag et al. (1990). Attention has to be paid in cases without a pronounced inversion at the top of the CBL. In this study, the simple parcel method was used. For the stable case, determination of the boundary layer height is not that straightforward. From the potential temperature profile, the SBL height can be derived as the top of the temperature inversion or the first discontinuity in the profile (Yamada, 1979, Hanna, 1969).

At the top of the CBL a reduction of moisture occurs, which makes it possible to derive the CBL height as well as the RL height from profiles of specific humidity (Seibert et al., 1998). Baumann-Stanzer and Groehn (2004) recognised the top of the CBL and the top of the RL at night with a decrease of specific humidity q of more than $0.01 \text{ g kg}^{-1} \text{ m}^{-1}$ with height. They called this the “humidity-jump method”.

During the night, a maximum wind speed is frequently observed close to the top of the SBL (see section 2.3.2). To identify such a maximum, Baumann-Stanzer and Groehn (2004) demanded at least 0.5 m s^{-1} higher wind speed than measured at the lowest level. The height of the wind minimum above such a maximum is another measure for the height of the RL.

The Richardson number as a measure for atmospheric dynamic stability may be used for the determination of the boundary layer height. The gradient Richardson number Ri reads as (e.g. Seibert et al., 1998):

$$Ri = \left(\frac{g}{\theta_0} \right) \frac{\frac{\partial \theta}{\partial z}}{\left(\frac{\partial u}{\partial z} \right)^2 + \left(\frac{\partial v}{\partial z} \right)^2} \quad (3-5)$$

with the acceleration due to gravity g , the potential temperature at surface θ_0 and the vertical gradients of potential temperature θ and horizontal wind components u and v .

The bulk Richardson number Ri_b is derived from this expression by substituting the gradients by finite difference expressions. It is assumed that in homogeneous and quasi-stationary conditions turbulence production vanishes at the SBL top and the Richardson number therefore exceeds its critical value Ri_c . The traditional approach leads to the following equation for the bulk Richardson number across the whole boundary layer (e.g. Hanna, 1969):

$$Ri_b = \left(\frac{g}{\theta_0} \right) \frac{(\theta_h - \theta_0) \cdot h}{u_h^2 + v_h^2} \quad (3-6)$$

Here θ_0 and θ_h are the potential temperatures at the surface and at the boundary layer top (frequently, virtual potential temperatures are used), h is the boundary layer depth and u_h and v_h are the wind speed components at the boundary layer top. The critical Richardson number marks the boundary between laminar and turbulent regions and has a value around 0.25 (Vogelezang and Holtslag, 1996). The boundary layer height h is defined as the height where the Richardson number becomes equal or larger than the critical Richardson number. Equation (3-6) reflects the ratio of buoyancy destruction across the whole boundary layer and the overall shear production. Vogelezang and Holtslag (1996) modified this traditional method by calculating the bulk Richardson number Ri_g between the top of the surface layer (or a fixed level z_s such as 20 m or 40m) and the top of the boundary layer h .

$$Ri_g = \left(\frac{g}{\theta_0} \right) \frac{(\theta_h - \theta_s) \cdot (h - z_s)}{(u_h - u_s)^2 + (v_h - v_s)^2} \quad (3-7)$$

Herein the index s refers to values at the height z_s .

The above explained formulations are only valid in stable conditions. For a neutral boundary layer turbulence due to surface friction is taken into account and the term $b \cdot u_*$ is added to the numerator in equation (3-7) ($b = 100$). To expand the use of the bulk Richardson number method to unstable conditions, a correction for the lower boundary condition for temperature is made (Vogelezang and Holtslag, 1996).

Even though Richardson number formulations as in equations (3-6) and (3-7) are strictly valid only in stable conditions, they are frequently applied in conditions that are dominated by convective turbulence as well (e.g. Baumann-Stanzer and Groehn, 2004). Seibert et al. (1998) recommended the use of an excess temperature when applying Richardson number methods in convective conditions, similarly to the advanced parcel method.

From the presentation of methods to determine the boundary layer height from radiosonde and tethered balloon data it is obvious that not every method is appropriate in all conditions. Seibert et al. (1998) considered the parcel method to be the most reliable method under convective conditions, whereas the Richardson number method was regarded as the most suitable method under conditions with mechanically produced

turbulence. Hennemuth and Lammert (2006) found that even though the parcel method seems to be the most reliable method, in the afternoon the humidity gradient method was superior due to the decrease in near surface temperature which made the parcel method inapplicable. Good agreement was found for ABL heights inferred from the parcel method and the Richardson number method.

3.3.3 NWP model output (Lokal-Modell)

The atmospheric boundary layer height is an important parameter of boundary layer schemes in NWP models. Beljaars and Viterbo (1998) stressed the significance of a realistic representation of the boundary layer in respect to surface boundary layer conditions, interaction with other parameterisation schemes and forecast products at observation level.

The scheme incorporated in the Lokal Modell (LM) to determine the boundary layer height uses the Richardson number (Fay et al., 1997). At each model grid point, height level, and time step Richardson numbers are computed as part of the calculation of exchange coefficients. In the LM the discretized form of the gradient Richardson number Ri is applied:

$$Ri = \left(\frac{g}{\theta_v} \right) \frac{\left(\frac{\Delta\theta_v}{\Delta z} + \frac{g}{c_p} \right)}{\left(\frac{\Delta s}{\Delta z} \right)^2} \quad (3-8)$$

with the acceleration due to gravity g , the virtual potential temperature θ_v , the specific heat c_p and the wind speed s . The critical Richardson number Ri_c has a value of 0.38. By the Richardson number scheme, boundary surfaces are defined at a level where a transition from laminar to turbulent conditions with height and vice versa takes place. In the LM, Richardson number profiles are searched from the surface upwards for Ri exceeding or falling below Ri_c . This scheme involves two steps. In the first step, the first transition from laminar to turbulent layers is detected, which is the height of the stable nocturnal boundary layer, labelled $pbstop$ in the model output. The second step determines the height of the mixed (convective) layer or residual layer ($pbltop$) at the first transition from turbulent to laminar layers. Exact heights are approximated between discrete model layers by a 2-step stability-weighted interpolation scheme (Fay, 2005). To avoid SBL heights from extending the typical range of 100 to 500 m, a preliminary maximum SBL height is set to model level 33 which is about 320 m above ground.

3.4 Input data for the parameterisations and the slab models

3.4.1 Parameterisations for the SBL height

Flux data from the turbulence measurements at the meadow station were used as input for the parameterisations. Only night time (0 CET to 6 CET) data was considered. Criteria for data selection were a buoyancy flux smaller than -5 W m^{-2} and surface friction velocity u_* larger than 0.05 m s^{-1} . Vickers and Mahrt (2004) noted that several difficulties arise when measuring surface fluxes in strongly stable conditions. In these data, poor quality of night time data as indicated by quality flags reflects these problems. Despite that, quality flags were not used as a criterion for data selection, except for data that fell in the worst quality class. To calculate the buoyancy frequency N the potential temperature gradient in the free atmosphere just above the boundary layer height is required. These gradients were calculated from half-hourly potential temperature profiles measured with the sodar/RASS, using potential temperature values of 20 m and 40 m above the SBL height determined from the reflectivity profile.

3.4.2 Slab models for the CBL height

The cumulative turbulent heat flux $(\overline{w'\theta'})_s$ is needed as an input for the slab models. Even though model equations in section 2.3.4.3 were derived for the sensible heat flux $(\overline{w'\theta'})_s$, in this study the buoyancy flux $(\overline{w'\theta'_v})_s$ from the turbulence measurements conducted at the meadow station was used following Yi et al. (2001) and Schipper et al. (2002). Calculation of the evolution of the CBL height with the slab model started when the buoyancy flux became positive (Driedonks, 1982). A problem occurred with that definition of initial conditions as the buoyancy flux was not always clearly smaller than zero during the second part of the night and numerous transitions of the zero value were observed. Therefore, the time of initiation was taken as the time when the buoyancy flux finally got greater than zero and did not become negative any more until the evening. Following Yi et al. (2001), the computation of the CBL depth z_i was performed until 2 hours after the buoyancy flux reached its maximum. The integration interval was 30 min. Equations (2-31) and (2-33) require the lapse rate above the top of the CBL, which was derived from radiosonde measurements. The gradient of each ascent was determined between 1600 and 4100 m asl and for each day the mean of this value from all ascents was calculated. Even though there were changes in the gradient, it was assumed to be constant for the whole day. The simple version of the slab model (equation (2-33)) did not require any initial input for the temperature profile and for the CBL height. For the use of equation (2-31) the initial value of the ABL height was taken from the results of the sodar measurements. Temperature values were taken from surface measurements due to a lack of sufficient temperature profile measurements. This assumption is justified as the influence

of the temperature value on the resulting CBL depths was determined and turned out to be very little. Calculations with this equation were done with z_i from the previous time step and surface measurements made during the actual time step.

3.5 **Statistical measures to evaluate model performance**

To evaluate model performance, various statistical measures were calculated. Willmott (1982) stressed that commonly used correlation measures like Pearson's product-moment correlation coefficient r and its square, the coefficient of determination r^2 are frequently not suitable and misleading. To compare model predicted and observed variables, difference measures seem to be more valuable. To describe average differences between observed (O) and model-predicted (P) variables, the mean absolute error MAE or the root mean square error RMSE can be computed:

$$MAE = N^{-1} \sum_{i=1}^N |P_i - O_i| \quad (3-9)$$

$$RMSE = \left(N^{-1} \sum_{i=1}^N (P_i - O_i)^2 \right)^{0.5} \quad (3-10)$$

To test whether the model overestimates or underestimates the measured values, Vickers and Mahrt (2004) evaluated the mean percent bias MPB:

$$MPB = N^{-1} \sum_{i=1}^N \left(\frac{100(P_i - O_i)}{O_i} \right) \quad (3-11)$$

4 Results and discussion

In this chapter, the results of the study are presented and discussed. At the beginning, the weather conditions during the experiment are shortly outlined to make the reader familiar with the framework of the study. The second part of this chapter deals with thermally induced wind systems, namely slope winds and Alpine pumping, as observed in this study. In the third section, the three golden days that are chosen for the determination of the ABL height are characterised. The fourth section covers the determination of the ABL height from measurements, parameterisations for the SBL, slab models for the CBL and Lokal-Modell output.

4.1 *Weather conditions during the experiment*

Prior to the beginning of the experiment a very unfortunate synoptic weather condition prevailed, dominated by a low that originated from the Mediterranean Sea where it had gathered a lot of moisture. Around the Alps, extremely high amounts of precipitation occurred from 21 to 23 August 2005 that lead to severe floods in Southern Bavaria. At the MOHp, an amount of 157.0 mm of precipitation was measured in these three days, which was about the mean amount of precipitation for August (1961-1990) (Rudolf et al., 2005). Further south in the Alpine regions, the amount of precipitation was up to twice as high.

Since 24 August 2005 this low lost its influence and high pressure weather, approaching from south west Europe, slowly gained in importance. From 27 August to 1 September 2005 Central Europe was under the influence of high pressure systems. Following two days (2 and 3 September 2005) under the influence of a small low from the North Sea, another high from southern Scandinavia established its influence on Germany on 4 September 2005 and governed the weather conditions until 9 September 2005. A low over Eastern Germany and Poland with its unsettled weather conditions replaced the high pressure period from 10 September 2005 on. From 13 until 15 September 2005 a ridge of high pressure prevailed, which was followed by another period predominated by a low. Its cold front reached southern Bavaria on 17 September 2005.

The synoptic conditions were very well reflected in the observed atmospheric conditions. Figure 4-1 shows maximum, mean and minimum daily values of temperature, relative humidity and wind speed at the MOHp. Elevated temperatures and larger temperature amplitudes as well as lower relative humidity indicated high pressure periods. On 17 September, the approaching cold front was accompanied by a break-in of cold air and very moist conditions with high amounts of precipitation (Figure 4-1). Precipitation occurred mainly during three periods (2-3 September, 9-12 September and 16-18 September) that coincided with low pressure periods. High wind speeds accompanied the change in weather conditions from high pressure periods to low pressure periods (9/10 September and 16 September 2005).

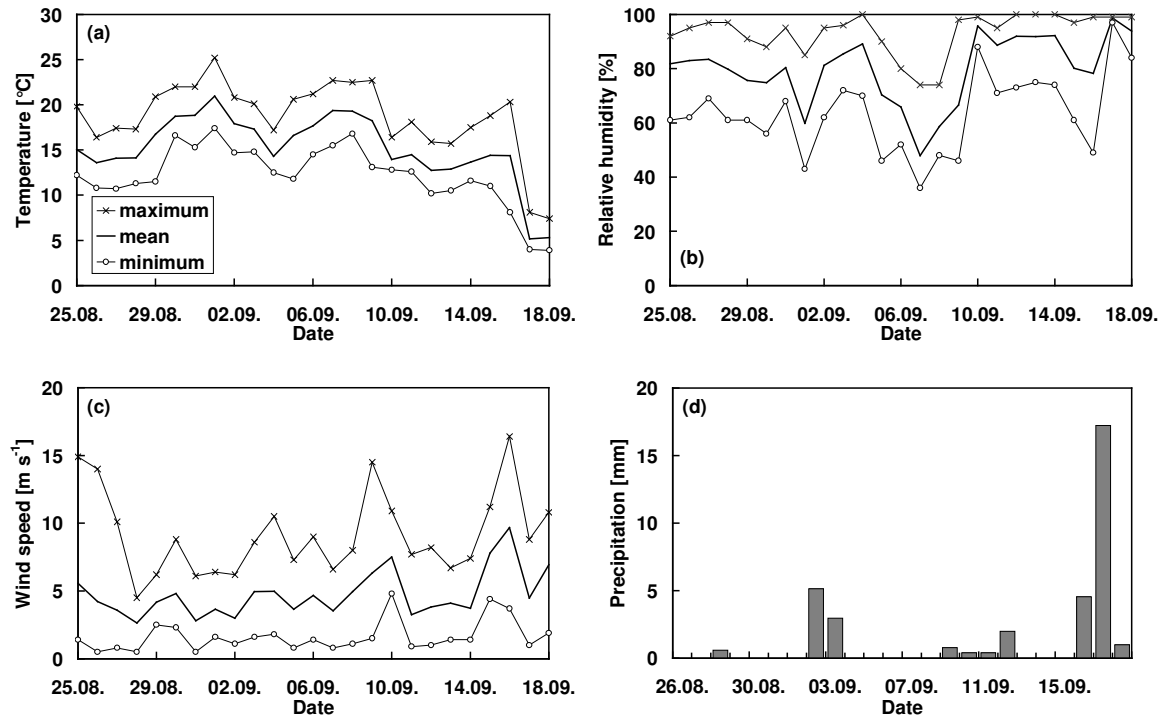


Figure 4-1: Maximum, mean and minimum daily values of temperature (a), relative humidity (b) and windspeed (c) measured at the Meteorological Observatory Hohenpeißenberg (MOHp) from 25 August to 18 September 2005 and daily precipitation (d) measured at the boundary layer station from 26 August to 18 September 2005.

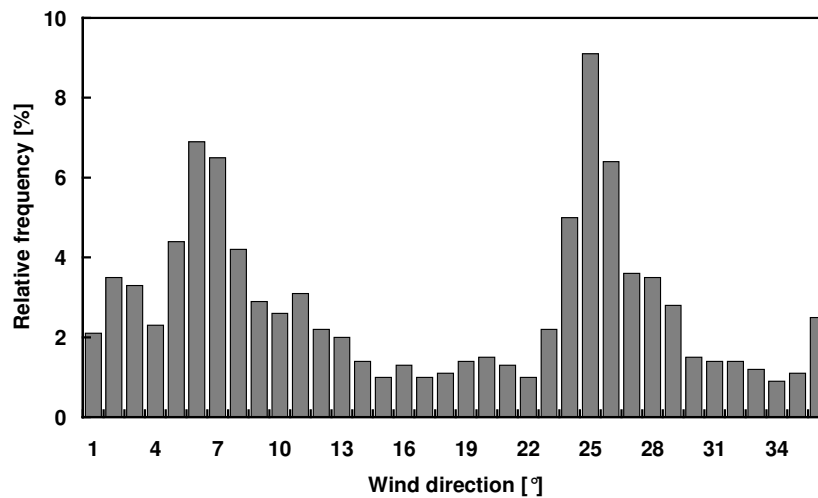


Figure 4-2: Relative frequency of wind direction (10 min averages) at the Meteorological Observatory Hohenpeißenberg (MOHp) from 25 August to 18 September 2005 ($N = 3599$, wind speed $> 1 \text{ m s}^{-1}$).

The relative frequency of wind direction measured at the observatory on top of the mountain (Figure 4-2) during the experiment exhibits a bimodal distribution. The main wind direction was 230° to 270° , the second, lower peak of wind direction was found between 50° to 80° . A similar pattern was observed in August and September of the years 1995 to 2004 (Oldenburg, 2005). Compared to the frequency distribution in her study, only the magnitudes of the two peaks differ, as during SALSA 2005 the relative frequency of north-easterly wind directions was more pronounced than during the years before and the

relative frequency of westerly winds was not as distinct as during previous years.

4.2 Thermally induced wind systems

4.2.1 Slope winds

To analyse the influence of the terrain on the wind distribution, relative frequencies of wind direction at the meadow station and the MOHp were compared. Two pronounced peaks were also found in the frequency distribution at the meadow station at 2 meters above ground (Figure 4-3). One maximum occurred at easterly wind directions (80-100°), the other one at northerly wind directions (360-20°). Southerly wind directions were rarely observed. When compared to Figure 4-2, considerable differences of the wind distribution between these two sites are seen. First of all, due to the location of the measurement site, wind speeds of less than 1 m s^{-1} hardly occurred at the MOHp, being on top of a mountain, whereas at the meadow station more than one third of the wind speed values was smaller than 1 m s^{-1} . A distinct peak at easterly wind directions occurred in both wind distributions, even though there was a deviation of about 30° of the largest peak with wind directions at the MOHp being more to north-east. The second peak (230-270°) that is seen at the MOHp was not found at the meadow station, even though west north-westerly wind directions (290-310°) occurred quite frequently at the meadow station. On the other hand, northerly wind directions appeared less frequently at the MOHp whereas these directions formed the most frequent wind direction at the meadow station for low wind speeds.

A closer look at the wind data at the meadow station revealed that northerly wind directions predominantly occurred at night. For illustration, 5 September 2005 was chosen, which was a day when Alpine pumping occurred. Fair weather conditions prevailed, which is favourable for the development of thermally induced wind systems. Figure 4-4 displays the wind direction at the meadow station and the MOHp for 5 September 2005. At the MOHp the course of the wind direction was typical for an Alpine pumping day (as described in more detail in the next section). The meadow station experienced a completely different diurnal course of wind direction. During the night, northerly to north-easterly wind directions were observed. From 8 to 9 CET wind direction shifted to south south-easterly wind directions, which lasted until 12:30 CET. Except for the night hours (21 to 24 CET), there was no exact agreement between the wind direction at the MOHp and the meadow station at any time. In the afternoon, wind directions were closest to each other and exhibited a similar course, even though there was a deviation of about 30° with easterly wind directions at the meadow station and north-easterly wind directions at the MOHp. The same displacement was observed for the peak in the distribution of the wind direction.

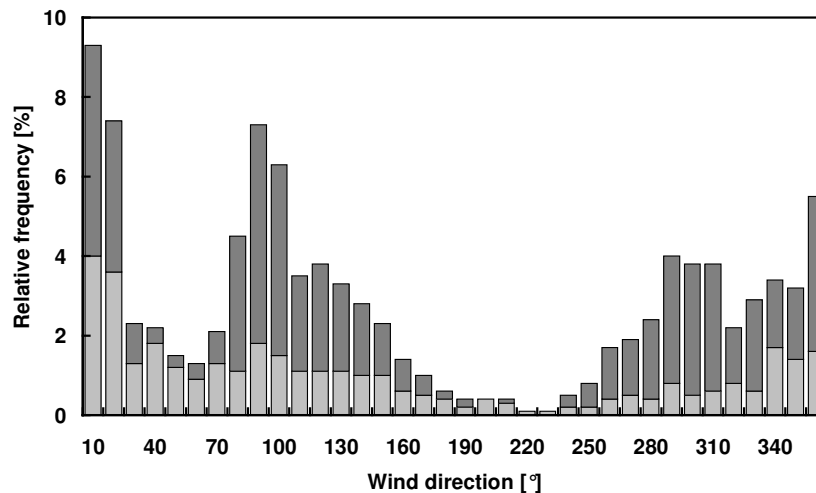


Figure 4-3: Relative frequency of wind direction measured with the sonic anemometer (30 min averages) at the meadow station from 25 August to 18 September 2005. Dark grey: wind speed $> 1 \text{ m s}^{-1}$, light grey: wind speed $< 1 \text{ m s}^{-1}$ (N = 1141).

The meadow site slightly sloped in north-eastern direction and was situated southwest of the mountain. Therefore, winds from north-easterly directions followed the slope of the terrain. As these wind directions mainly occurred during clear nights in high pressure periods, they could be identified as downslope winds. It is questionable whether southerly wind directions at the meadow station from 9 to 12:30 CET can be classified as upslope winds. The sudden change in wind direction between 8 and 9 CET might also have been an adjustment to the prevailing wind direction. On the other hand, the onset of the Alpine pumping occurred around 9 CET with a sudden change to north-easterly wind directions and not southerly wind directions. From Figure 4-3 it can be seen that southerly wind directions were very rare, indicating that upslope flows were not a frequent phenomenon and may only develop on very few days. Unfortunately, only a very limited data base was available for characterising slope winds, with only one measuring point at one height at the meadow station. Sodar data could not be used to identify slope winds as this is a small-scale phenomenon occurring in a shallow layer adjacent to the ground, probably below the range of the sodar data.

The displacement of wind direction between the two measurement sites of about 30° in the afternoon of 5 September 2005 as well as in the frequency distribution of wind directions was probably due to the modification of the wind flow caused by the mountain, which was situated north-east of the meadow measuring station.

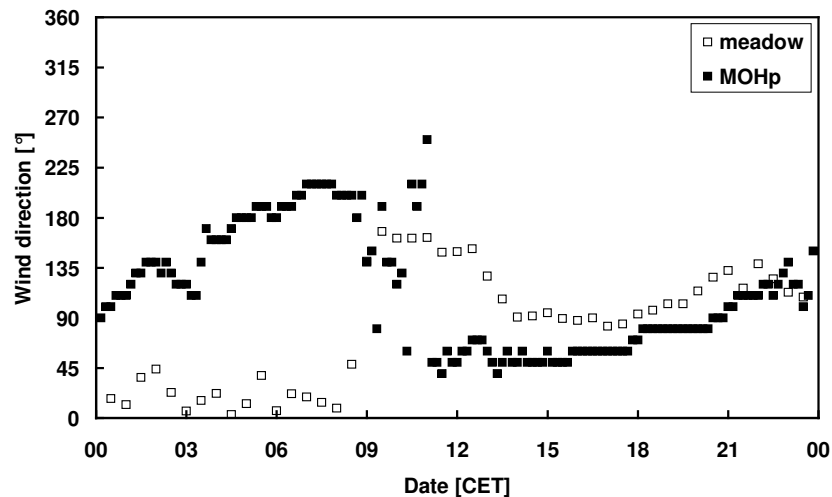


Figure 4-4: Wind direction at the meadow station ($z = 2$ m, 30 min averages) and the Meteorological Observatory Hohenpeißenberg (MOHp) ($z = 10$ m, 10 min averages) for 5 September 2005.

4.2.2 Alpine pumping

The days of the field campaign were classified in terms of radiative input following Lugauer and Winkler (2005). They developed a classification scheme based on daily total global radiation $K\downarrow_d$ to identify days that were favourable for the development of a mountain-plain circulation (class 1: $K\downarrow_d \geq 20 \text{ MJ m}^{-2}$; class 2: $10 \leq K\downarrow_d < 20 \text{ MJ m}^{-2}$; class 3: $K\downarrow_d < 10 \text{ MJ m}^{-2}$). During the period of 25 days between 25 August and 18 September 2005 the distribution of radiation classes was as follows: 8 days belonged to class 1, 12 days to class 2 and 5 days to class 3 (Figure 4-5). The following analysis was restricted to radiation class 1, similarly to the study by Lugauer and Winkler (2005). There were two periods each lasting four days that experienced high radiative input, period 1 from 29 August to 1 September 2005 and period 2 from 5 September to 8 September 2005.

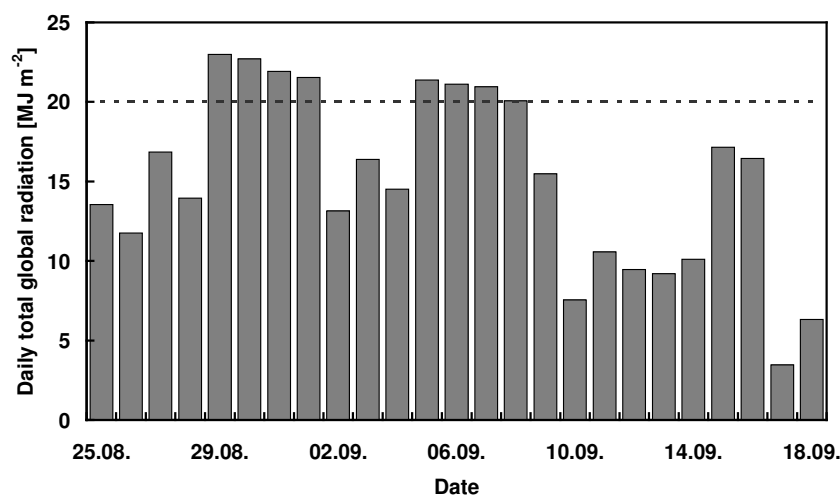


Figure 4-5: Daily total global radiation at the meadow station from 25 August to 18 September 2005. The dotted line marks 20 MJ m^{-2} (class 1 of daily total global radiation: $K\downarrow_d \geq 20 \text{ MJ m}^{-2}$, following Lugauer and Winkler, 2005).

During these two periods synoptic preconditions for Alpine pumping, as stated in Weissmann et al. (2005), were fulfilled with central Europe being under a high pressure area or a ridge. Upper-level synoptic winds were weak, with wind speeds up to 5000 m agl being less than 10 m s^{-1} . During period 1, data from radiosondes indicated 500 hPa wind directions being not very uniform and ranging between north-easterly, easterly and south-easterly, whereas during period 2 500 hPa wind directions were south-easterly to southerly most of the time.

The data analysis was done following Lugauer and Winkler (2002, 2005). For each period of four days the mean diurnal variations of wind speed s , persistence P , wind direction and wind components (u , v) of hourly means at the MOHp were computed. Persistence is calculated as:

$$P(t) = \frac{\sqrt{\overline{u(t)^2} + \overline{v(t)^2}}}{\overline{s(t)}} \quad (4-1)$$

and ranges between 0 and 1. $P(t) = 1$ means that wind direction at time t is constant over the whole data sample, whereas in cases when all wind directions occur with the same frequency $P(t) = 0$ results.

Mean wind directions (Figure 4-6) during period 1 were easterly to south-easterly during the night and northerly to north-easterly at daytime. The four days in period 1 were quite different concerning wind directions. During three days a more or less constant wind direction was observed with easterly to north-easterly winds at 29 and 30 August 2005 and westerly winds at 1 September 2005. The only day that experienced a sudden change in wind direction in the morning during period 1 was 31 August 2005. During period 2 all four days exhibited a similar daily variation in wind direction with a sudden change in wind direction around 9 CET. The mean wind direction during period 2 was characterised by southerly winds at night time and north-easterly winds in day time. The transition in the morning hours occurred very rapidly between 9 and 10 CET, whereas the evening transition proceeded more slowly, starting around 20 CET and lasting until midnight.

With the help of Figure 4-7 the characteristics of the wind at MOHp during the two periods can be analysed in more detail. Mean wind speeds were higher at night time during both periods, which is a typical feature of a mountain station. Period 2 exhibited a minimum in wind speed in the morning from 9 to 10 CET. The mean v - and u -component of the wind are presented in the lower two panels of Figure 4-7. For both periods there were two reversals of the v -component that occurred approximately at the same time, one in the morning (9 CET) and one in the evening (22 CET and 21 CET respectively). The strength of the v -component during the night was much larger for period 2 than for period 1, whereas at daytime equal strengths were observed. For the u -component the picture was different. During period 1 the value stayed constant (east) during most of the time, reaching a maximum in the evening. Reversals of the u -component were observed in

period 2, the first at approximately 9 CET, the second at approximately 22 CET. The u-component became the larger component after noon until the reversal in the evening. Persistence is displayed in the upper right panel of Figure 4-7. During both periods the highest persistence was found in the afternoon and in the evening. The persistence during period 1 did not show any striking pattern, whereas period 2 exhibited a distinct break-in of persistence at 9 CET. This feature reflects the sudden reversal of the wind direction in the morning from southerly to northerly winds. The second reversal of wind direction in the evening could not be identified in the persistence, which was due to the more continuous transition.

Lugauer and Winkler (2002, 2005) described mean characteristics of Alpine pumping. Comparison of these characteristics for the MOHp to the results of this study reveals that several features of period 2 are typical for Alpine pumping:

- Southerly wind directions in the second half of the night,
- The sudden reversal of wind direction in the morning hours at 9 CET,
- Minimum persistence in the morning and
- The continuous transition of wind direction in the evening.

In this study, in the daytime the u-component was larger than the v-component, meaning that the wind direction was more to the east, which was not observed by Lugauer and Winkler (2005). In their study such a behaviour was only reported for evening hours (18-24 CET).

Period 1 did not have the typical characteristics of Alpine pumping. Only one day during this period exhibited wind patterns that are typical for Alpine pumping, whereas wind directions were more or less constant during the other three days.

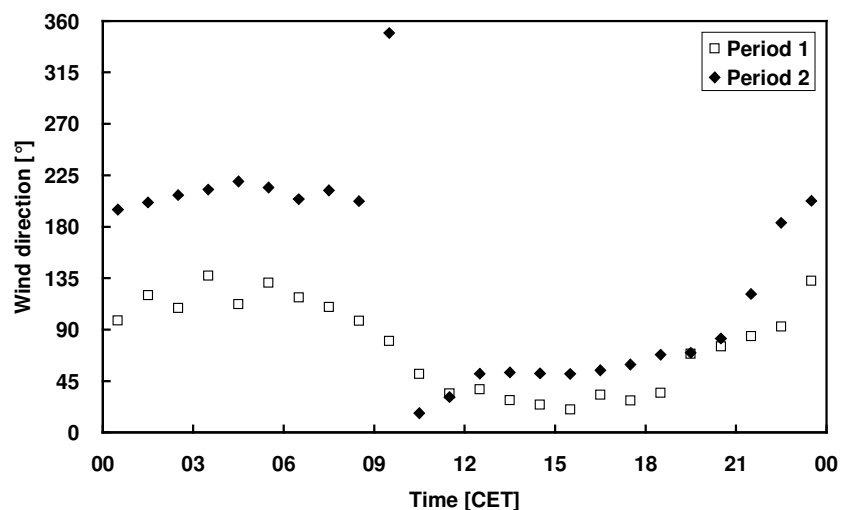


Figure 4-6: Mean diurnal variation of wind direction at the Meteorological Observatory Hohenpeißenberg for period 1 and period 2.

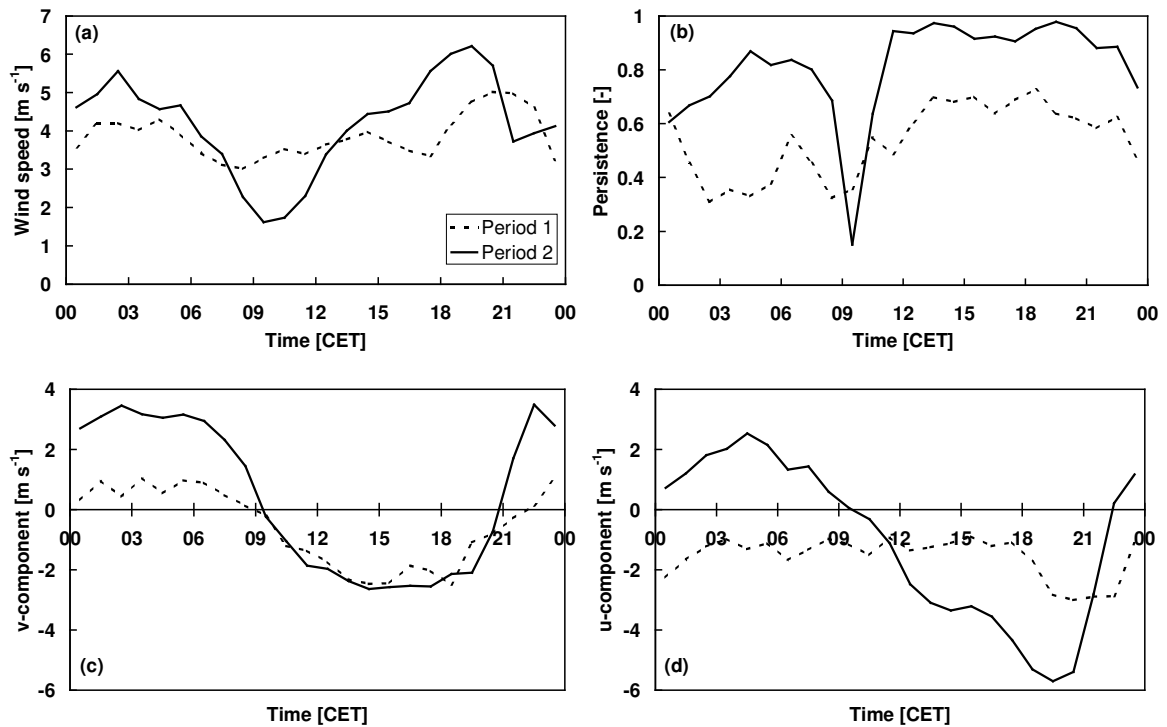


Figure 4-7: Mean diurnal variations of wind speed (a), persistence (b) and wind components ((c), (d)) at the Meteorological Observatory Hohenpeißenberg for period 1 (dashed line) and period 2 (solid line).

For a more detailed description of the phenomenon of Alpine pumping, 5 September 2005 was selected, which clearly showed the reversal of wind direction. During the night, the pattern of wind directions was complex (Figure 4-8). Above 100 m agl the wind slowly changed from easterly to southerly wind directions in the early morning hours, whereas wind directions behaved differently within the lowest 100 m adjacent to the ground with winds from north northwest. Around 8 CET wind direction suddenly changed to northeast in a layer adjacent to the ground up to 140 m agl. Higher up, the change of wind direction appeared a bit later, at 300 m agl at approximately 9:30 CET. The vertical propagation of the plain to mountain flow could be estimated from Figure 4-8, which resulted in a vertical propagation rate of about 0.036 m s^{-1} . This agrees with the rate of 0.04 m s^{-1} as estimated by Lugauer and Winkler (2005). From the sodar data the upper boundary of the layer of plain to mountain flow could not be detected after 11 CET due to the limited range of the sodar. In the lowest 400 m north-easterly winds prevailed during the day. In the evening the continuous transition to southerly winds is seen in the sodargram, starting from the surface.

The sudden change of wind direction was accompanied by a drop in temperature throughout the whole sodar/RASS temperature profile. This observation supports the theory that the observed phenomenon of reversal of wind direction can be attributed to Alpine pumping. Warm air was sucked from the foreland to the Alps, which resulted in the advection of colder air from the lower parts of the Alpine foreland.

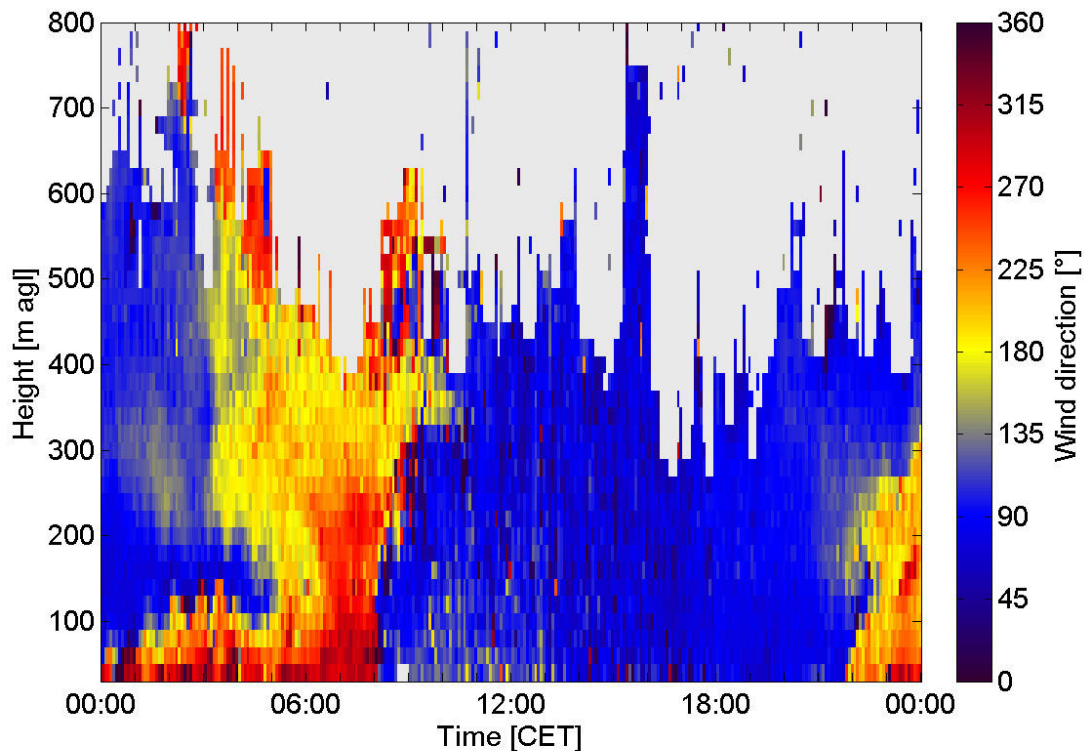


Figure 4-8: Sodagram of the wind direction for 5 September 2005.

Wind speeds during period 2 followed a more or less regular pattern (Figure 4-9). During times when the wind reversed its direction, low wind speeds occurred. After midnight in all nights except of 5 September 2005 a region of high wind speeds up to 8 m s^{-1} developed at about 250 to 300 m agl lasting until the morning hours. After Stull (1988) low-level jets (LLJ) are streams of high wind speeds with maximum values of 10 to 20 m s^{-1} usually observed 100 to 300 m above the ground. His criteria to define a LLJ is a relative wind speed maximum that is more than 2 m s^{-1} higher than wind speeds above it. This maximum has to be found in the lowest 1500 m of the atmosphere. Following this criteria, a LLJ could be identified on 7 September 2005. At midnight, maximum wind speeds occurred at 460 m agl. The peak of wind speed descended until 5 CET down to 220 m agl and then ascended again up to 320 m agl around 8 CET. Maximum wind speeds reached 7 m s^{-1} . Above this region of high wind speeds, wind speeds were low ranging at 2 m s^{-1} . On 6 September and 8 September 2005 regions of high wind speeds were not that easily identified as LLJ as data above the wind speed maximum was lacking most of the time. Another striking feature were regions of high wind speed that occurred between noon and evening, being most pronounced on 6 September and 8 September 2005. Wind speeds reached 10 m s^{-1} in 500 m agl in the evening hours before the reversal of wind direction started. High wind speeds in the daytime were very high throughout the profile and not as confined to one height level as during the night. During period 1 no such regular wind speed patterns were observed.

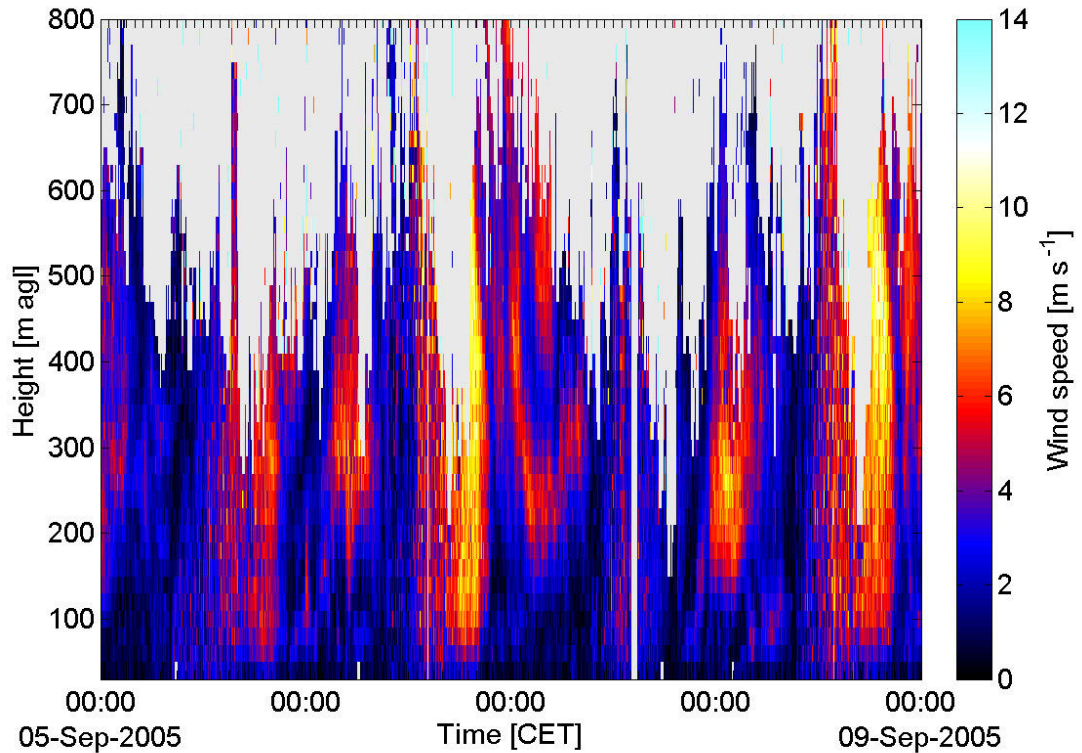


Figure 4-9: Sodagram of horizontal wind speed for period 2 (5 September to 8 September 2005).

4.3 Characterisation of the three golden days

For the determination of the ABL height, three days from the observation period were selected that were assumed to represent different weather conditions. In the following section, the prevailing meteorological conditions of these days are characterised.

The first day that was chosen was 30 August 2005. Due to the high radiative input (Figure 4-11), this day was allocated to radiation class 1 as defined in section 4.2.2. Skies were clear with a very low cloud cover throughout the whole day and no precipitation occurred. Even though preconditions for the development of Alpine pumping were favourable, no such wind system developed. At the MOHp prevailing wind directions were easterly to north-easterly throughout the whole day (Figure 4-12). At the meadow station easterly winds blew during the day and north-easterly slope flows were observed at night. The sodagram in Figure 4-10 shows the prevailing easterly flow throughout the day. During the night from 29 August to 30 August 2005 strong wind shear was observed. In the layer adjacent to the ground up to about 160 m agl southwest winds prevailed during the whole night (20:30 CET until 8 CET). A sudden change of wind direction with height occurred at the top of this layer, which was accompanied by a drop in wind speed. According to Kalthoff et al. (1998) strong wind-shear phenomena under stable stratification are a frequent phenomenon in mountainous terrain.

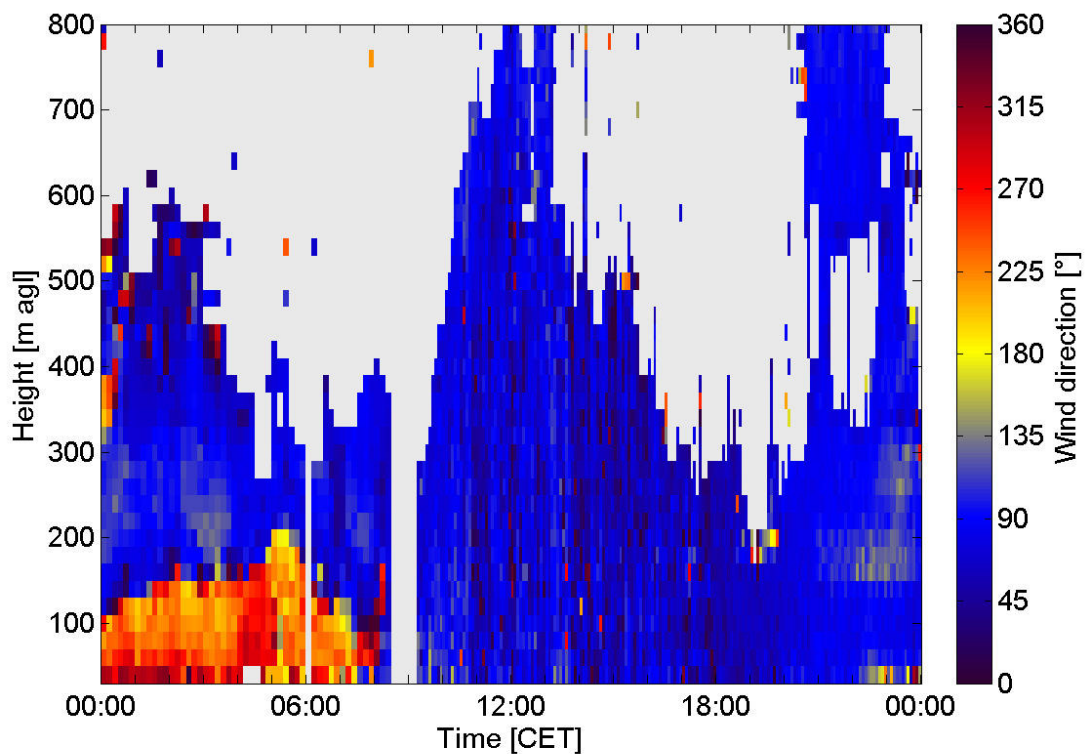


Figure 4-10: Sodargram of wind direction for 30 August 2005.

5 September 2005 was chosen as the second golden day. This day was already described in detail in previous sections concerning thermally induced wind systems. High radiative inputs were observed similarly to 30 August 2005 (Figure 4-11) and cloud cover was very low. Wind directions were typical for an Alpine pumping day (Figure 4-12).

The third golden day was 11 September 2005. In contrast to the two other days, this day only belonged to radiation class 2 with lower radiative input (Figure 4-11). In the forenoon hours cloud cover was very low. After 11 CET an increase in cloud cover was observed and precipitation was measured in the afternoon and evening with showers around 15:30 CET and 21:15 CET. Throughout the sodar range westerly winds prevailed during the whole day, as it is also seen in Figure 4-12 for the MOHp.

During all three days upper-level synoptic winds were weak with wind speeds up to 5000 m agl being less than 10 m s^{-1} .

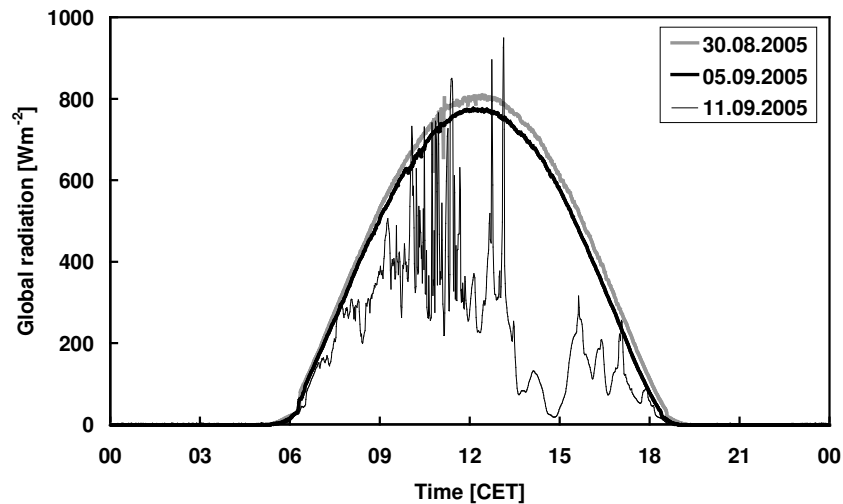


Figure 4-11: Global radiation at the meadow station for the three golden days.

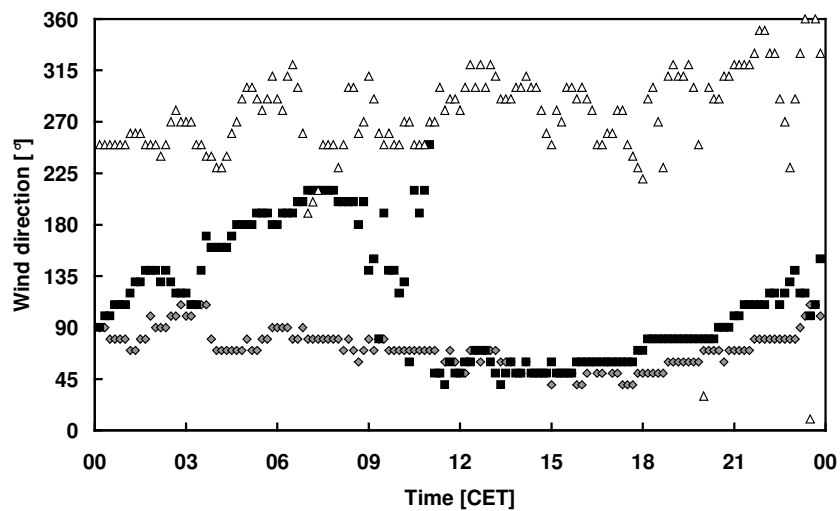


Figure 4-12: Wind direction at the MOHp for the three golden days (30 August: grey diamonds, 5 September: black squares, 11 September: white triangles).

4.4 Determination of the atmospheric boundary layer height

In this section, the results of the determination of the ABL height are presented. The first three subsections summarise results from the determination of the ABL height from measurements, namely radiosondes, sodar/RASS and tethered balloon measurements. Results from parameterisations, slab models and the Lokal-Modell are described in the following three subsections. Within each subsection, applicability of the methods as well as the influence of complex terrain on the structure of the ABL as seen in the results is discussed.

4.4.1 The ABL height determined from radiosonde data

Radiosonde data was available from routine ascents performed at three stations in the vicinity of Hohenpeißenberg. Temporal resolution varied from day to day, from only two ascents on 11 September 2005 to five ascents on 5 September 2005. Different methods were applied to the profiles of meteorological data, as was described in section 3.3.2. Table 4-1 summarises the results for the three golden days. From this table it is obvious that no statistical analysis was possible due to the limited number of ascents. Not every method was applicable to all profiles, as not every method was appropriate for all conditions. An exception was the determination from the profile of virtual potential temperature, which was possible in all cases, namely the simple parcel method (SPM) under convective conditions and the first discontinuity in the virtual potential temperature profile (1stD) under stable conditions. For these three days no systematic overestimation or underestimation of any method could be seen. In a few cases different methods agreed with each other, like the SBL height from the first discontinuity in the virtual potential temperature profile (1stD) and the maximum of wind speed (WMAX) for 5 September 2005 at 4 CET. On the other hand, large deviations may occur between the CBL height determined by the simple parcel method (SPM) and the humidity jump method (HU), as observed for 5 September 2005 at 13 CET.

CBL heights determined by the traditional Richardson number method (RI) following formula (3-6) were in most cases in accordance with CBL heights determined by the simple parcel method (SPM), even though Richardson number methods were strictly speaking not applicable in convective conditions. In stable conditions the Richardson number method (RI) failed in most cases, which may have been due to very low wind speeds and the very coarse resolution of the profiles. The Richardson number method using formula (3-7) after Vogelezang and Holtslag (1996) failed in most cases, probably also due to the factors mentioned before. Problems associated with methods using a Richardson number under stable situations were mentioned by Seibert et al. (1998) and Baumann-Stanzer and Groehn (2004) as wind profiles measured by radiosondes may be inaccurate and/or not sufficiently well resolved near the ground.

In the following, three radiosonde ascents performed at Altenstadt are exemplified. Figure 4-13 shows profiles of virtual potential temperature and relative humidity for 30 August 2005 for a stable case (4 CET) and a convective case (10 CET). The profiles at 4 CET were typical profiles under stable conditions. The virtual potential temperature profile was used to determine the SBL height as the first discontinuity of the profile. The humidity jump method (HU) yielded the RL height. The RL height can also be seen in the virtual potential temperature profile by a deviating profile at the same height where the humidity jump is found. In the profiles under convective conditions it can be seen that CBL heights determined from different methods differed. Even though both methods (SPM and HU) were applicable in this case, a large deviation occurred.

Table 4-1: ABL heights [m asl] determined from radiosonde ascents at Oberschleißheim (OS), Altstadt (AS) and Hohenpeißenberg (HP) following various criteria (SPM = simple parcel method, 1stD = 1st discontinuity, HU = humidity jump, WMAX = maximum of wind speed, WMIN = minimum of wind speed, RI = Richardson number, RI(VH) = Richardson number after Vogelezang and Holtslag (1996).)

	SPM	1stD	HU	HU2	WMAX	WMIN	WMAX2	WMIN2	RI	RI(VH)
30.08.2005										
01:00 OS	--	600	1334	--	879	1500	--	--	--	--
04:00 AS	--	900	1761	--	--	--	--	--	--	--
10:00 AS	1660	--	1340	--	--	--	--	--	1509	--
05.09.2005										
01:00 OS	--	705	850	1347	651	850	1063	1434	525	--
04:00 AS	--	1050	1079	1675	1050	1193	--	--	--	--
06:00 HP	--	1130	1025	1267	--	--	--	1267	--	--
10:00 AS	1113	--	1018	2540	--	--	--	--	1103	--
13:00 OS	1140	--	825	1542	--	--	--	--	1090	1139
11.09.2005										
01:00 OS	--	758	--	--	--	--	--	--	645	604
13:00 OS	1350	--	1559	--	--	--	--	--	1116	1167

Figure 4-14 shows profiles of virtual potential temperature and relative humidity (left) as well as wind speed and wind direction (right) for the early morning ascent (4 CET) at Altstadt on 5 September 2005. These profiles revealed a very complex structure and made it difficult to apply methods for the determination of the ABL height. The profile of virtual potential temperature exhibited more than one discontinuity and there were two jumps in the profile of specific humidity. Wind profiles also did not have a text book like shape, with several rotations in the profile of wind direction. All ascents on 5 September 2005 exhibited such a complex structure with multiple layering, which may have been due to the mesoscale circulation (Alpine pumping) between the foreland and the Alps. Thus, it was not straightforward to derive ABL heights from radiosoundings for this day.

From the results illustrated above it is clear that the application of different methods lead to different ABL heights. Errors in the estimation of the boundary layer height from radiosondes were reported to be about ± 100 m (Van Pul et al., 1994; Driedonks, 1982). There were a few cases where deviations between different methods were larger than this estimated error. The database in this study was not large enough to draw a conclusion as to which of the methods was most appropriate under the observed conditions. Due to the poor temporal resolution and the large spatial distribution, ABL heights from radiosondes can only be used as an orientation in this study.

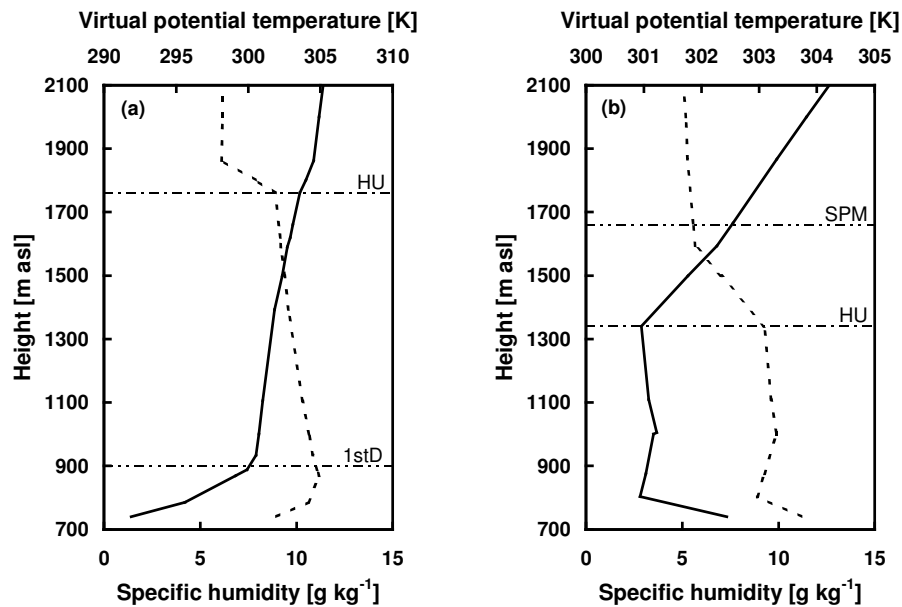


Figure 4-13: Profiles of virtual potential temperature (solid line) and relative humidity (dashed line) measured by radiosondes at Altenstadt on 30 August 2005 at 4 CET (a) and 10 CET (b). Vertical lines mark the SBL height and the CBL height, respectively, determined by different methods (SPM = simple parcel method, 1stD = 1st discontinuity, HU= humidity jump).

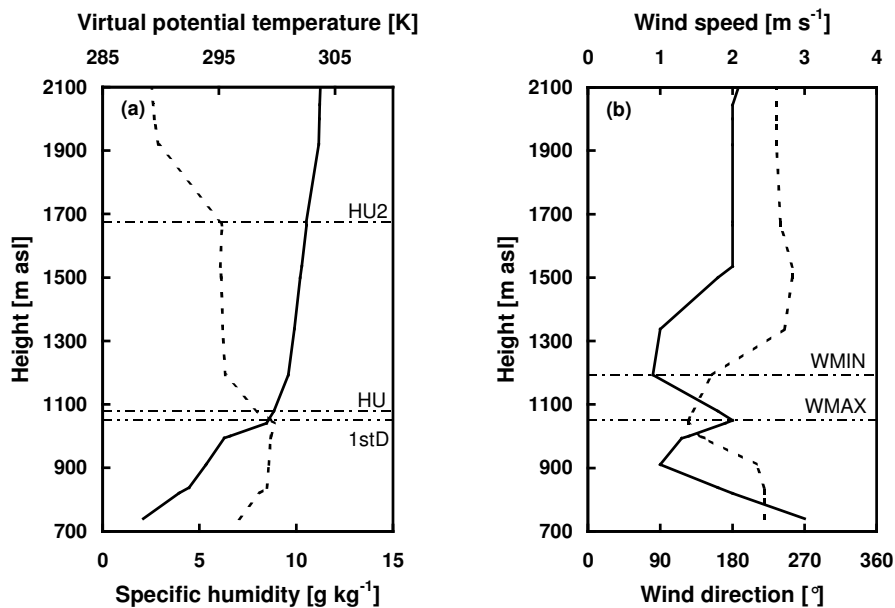


Figure 4-14: Profiles measured by radiosonde at Altenstadt on 5 September 2005, 4 CET. (a): virtual potential temperature (solid line) and relative humidity (dashed line), (b): wind speed (solid line) and wind direction (dashed line). Vertical lines mark the SBL height and the CBL height, respectively, determined by different methods (1stD = 1st discontinuity, HU = humidity jump, WMAX = maximum of wind speed, WMIN = minimum of wind speed).

4.4.2 The ABL height determined from sodar/RASS data

4.4.2.1 Visual inspection of reflectivity profiles

In this section the determination of the ABL height from sodar/RASS data is investigated. The analysis was done for the three golden days. Half-hourly means of reflectivity data of the vertical antenna (A3) were used, the time indicated marks the end of the half hour period. By visual inspection of these profiles, the height of the elevated (secondary) maximum of reflectivity was taken as ABL height in convective conditions whereas in stable conditions the shape of the profile was analysed as a first step and as a second step the appropriate criterion according to Table 3-4 (Beyrich et al., 1996) was applied. For these three days, all half-hourly profiles under stable conditions except for two had a shape with an elevated maximum of signal intensity. Therefore, the criterion that was applied in nearly all cases for day and night was the height of the elevated maximum. One profile (30 August 2005, 19:30 CET) showed a continuous decrease with decreasing gradient. In one case (11 September 2005, 5:00 CET) it was not possible to attribute any shape type to the profile, therefore no ABL height detection was possible. Unfortunately there was a gap in the data on 30 August 2005 in the morning (9:00 to 9:30 CET) which was caused by a change in sampling time and maintenance of the system. It was only possible to determine the SBL height and the transition to the CBL in the morning hours. In the afternoon the ABL height was out of the range of the sodar data. The evening transition period is still not very well understood (Beyrich and Görsdorf, 1995). During this period the reflectivity vanishes nearly completely, which is attributed to the cessation of heating from below (Emeis et al., 2004). Therefore, the ABL height could only be determined before and after that transition period.

Figure 4-15, Figure 4-16 and Figure 4-18 show the sodargrams of reflectivity together with the derived ABL depth. In several cases more than one elevated secondary maximum was observed, as stands for 30 August 2005 from midnight until the morning hours. In most of these cases two maximums appeared. The most pronounced maximum was taken as SBL height, which was mostly the lowest secondary maximum. For 5 September 2005 up to three maximums occurred in the first half of the day. All three maximums are displayed in Figure 4-16. To make a decision on which of the three observed maximums for 5 September 2005 reflects the ABL height, the sodargram of the standard deviation of the vertical wind velocity σ_w was taken as an additional supporting criterion. The criterion to determine the CBL height is a strong decrease of the standard deviation of the vertical wind velocity (Best et al., 1986, cited in Beyrich, 1997). In Figure 4-17 it can be seen that the lowest maximum marked the boundary between the very turbulent region due to the convection beneath the ABL height and the region with lesser turbulence above the ABL height. Therefore, the lowest maximum was taken as the ABL height and was used for comparison in the following sections.

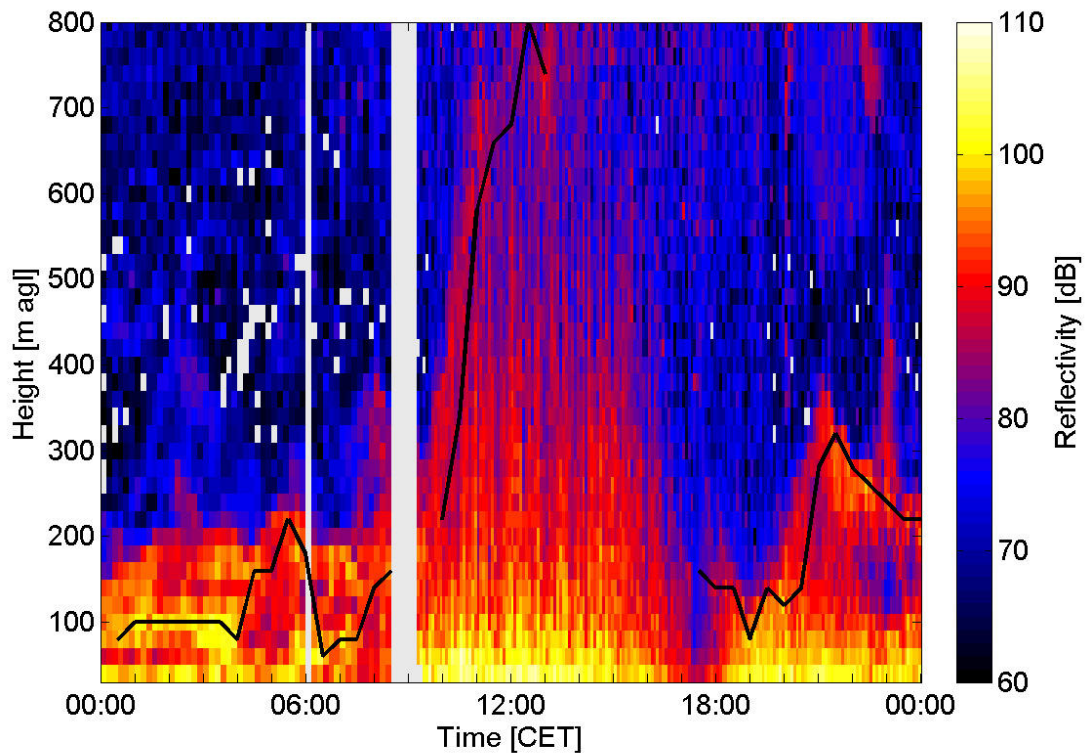


Figure 4-15: Sodargram of reflectivity for 30 August 2005. The ABL height is indicated by the black line, thereby values are indicated at the end times of the half hour period.

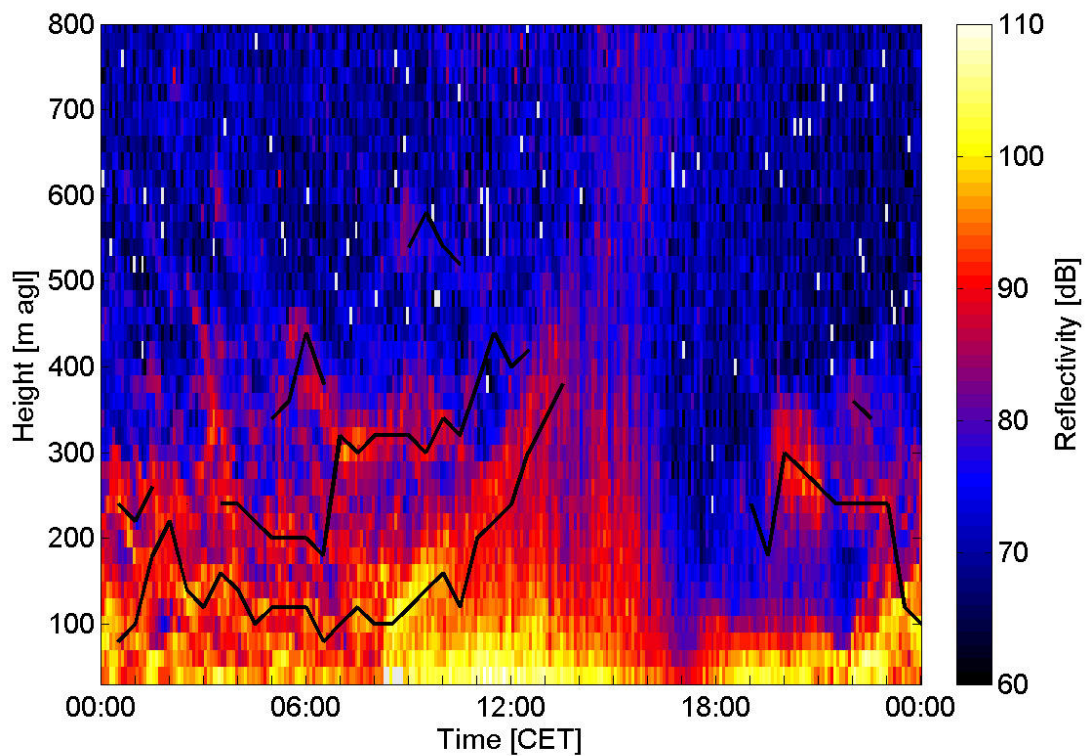


Figure 4-16: Sodargram of reflectivity for 5 September 2005. The ABL height is indicated by the black line, thereby values are indicated at the end times of the half hour period.

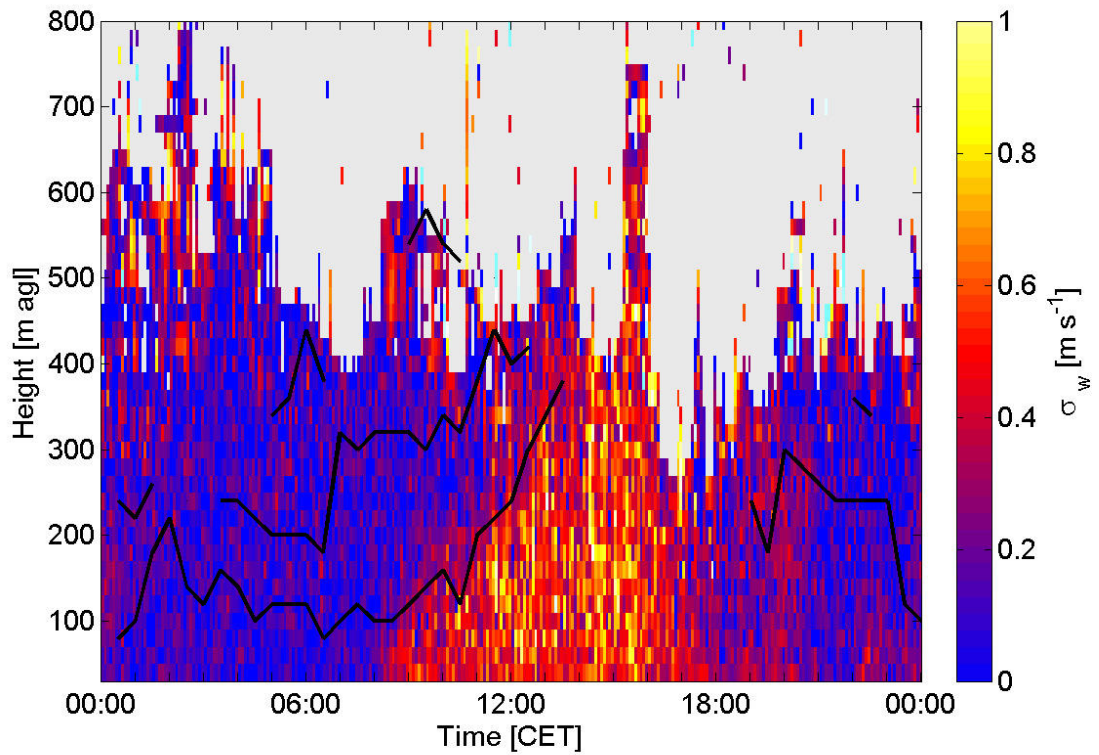


Figure 4-17: Sodargram of the standard deviation of the vertical wind velocity for 5 September 2005. The ABL height determined from reflectivity profiles is indicated by the black line, thereby values are indicated at the end times of the half hour period.

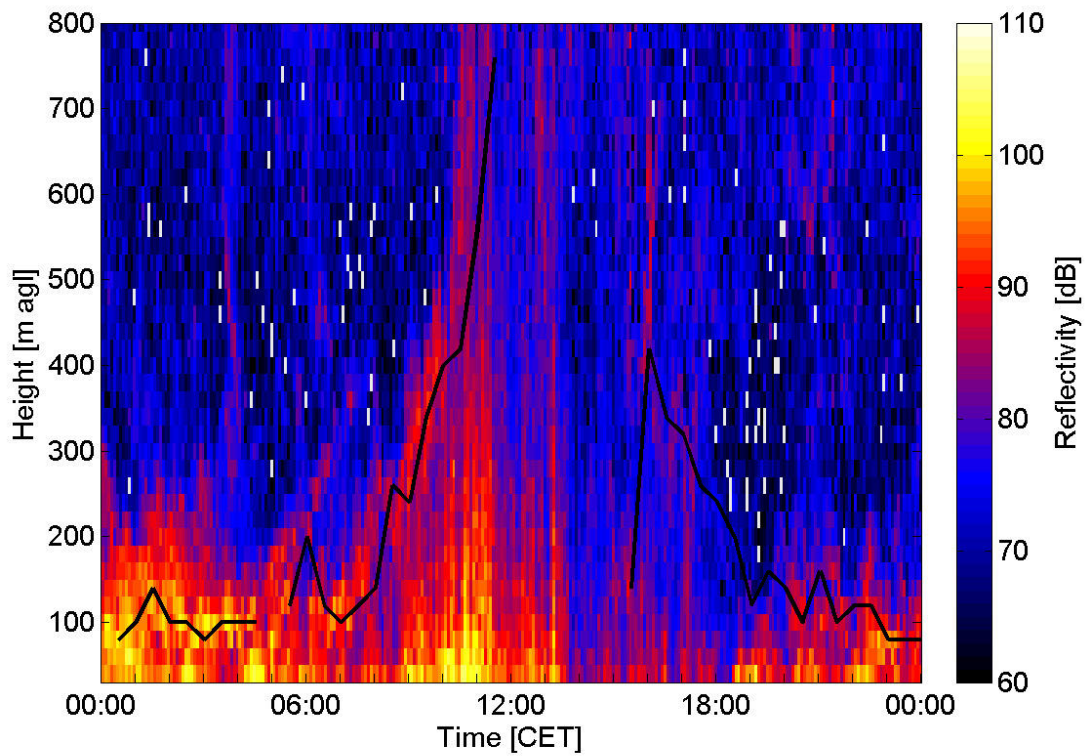


Figure 4-18: Sodargram of reflectivity for 11 September 2005. The ABL height is indicated by the black line, thereby values are indicated at the end times of the half hour period.

Table 4-2: Characteristics of the development of the CBL height using the elevated (secondary) maximum of reflectivity criterion.

	Start of CBL growth [CET]	Elevating rate [m h^{-1}]
30 August 2005	06:30	120
5 September 2005	08:00	50
11 September 2005	07:00	130

The characteristics of the development of the CBL in the morning hours are summarised in Table 4-2. On 30 August 2005 and 11 September 2005 the CBL started to grow approximately at the same time (6:30 CET respectively 7:00 CET). The evolution of the CBL depth was similar for these two days with elevating rates that lay in the range quoted by Seibert et al. (1998) (see section 2.3.1). In this study no distinction was made between the two phases of CBL growth and only one elevating rate was calculated for each day. However, from the figures it can be seen that growth of the CBL was slower in the early morning hours and increased in the forenoon hours. In both cases the CBL reached a depth of about 800 m agl around noon. On 5 September 2005 the evolution of the CBL started later, the elevating rate was much lower and the CBL depth reached only 380 m agl at 13:30 CET. It was surprising that only such low values were reached as 5 September 2005 was a fair weather day with high radiative input.

When comparing the detected ABL heights to wind direction and wind speed sodargrams, several features could be observed. On 30 August 2005 and 5 September 2005 shear layers adjacent to the ground were observed during the night until the morning hours (until 8 CET and 5 CET respectively) that were marked on top by a sudden change of wind direction with height and a drop in wind speed (see Figure 4-10 and Figure 4-8). The elevated secondary maximum of reflectivity was frequently in the range of the top of the shear layer, which was also observed by Emeis et al. (2004). On 30 August 2005 two elevated secondary maximums of reflectivity were observed. The lower one reflected the height of the wind speed maximum within the shear layer whereas the upper one was located at the top of the shear layer. The magnitude of these maximums changed, which was the reason why during the first few hours of 30 August 2005 (until 4 CET) the lower maximum was taken as the SBL height. After that during a short period the second maximum was more pronounced, before the development of the CBL started from below at 6:30 CET. On 5 September 2005 the SBL height coincided well with the top of the shear layer during the night until 5 CET. After the onset of the Alpine pumping, the CBL height was lower than the top of the layer of plain to mountain flow. In the evening of both days (21 CET respectively 20 CET) the ABL depth was detected quite high at about 300 m agl with very pronounced elevated secondary maximums. In both cases these maximums were associated with very high wind speeds which may be attributed to LLJs. For 11 September 2005 no such striking features were found.

Unfortunately temperature data from the RASS could not be used to determine the

ABL height. Quality of this data was only satisfactory to heights of about 300 to 400 m agl during the day and even a bit lower during the night, which was frequently the range of the ABL height. For the same reason, the determination of the ABL height by the use of Richardson numbers was constrained.

4.4.2.2 Automatic detection

The ABL depth was detected automatically by the routine suggested by Emeis and Türk (2004). Even though this method used system specific values, to begin with it was applied without any changes of these values. Later, improvement of the results were achieved by adjustment of the values, but without changing the general structure of the routine itself.

Input data for the routine were half-hourly means of reflectivity profiles as well as half hourly means of the standard deviation of the vertical wind velocity profiles. The final output, called height of the mixing layer MLH in their paper, as well as the heights H_1 and H_2 as they result from the two criteria were analysed.

For all three days results are displayed in Figure 4-19, Figure 4-20 and Figure 4-21. In general, during the night until the morning hours the ABL depth determined by visual inspection ($R_{\max} > 1$) coincided reasonably well with the ABL depth resulting from the automatic routine (MLH). The second criterion H_2 mainly determined the MLH output during these times. In the forenoon and around noon poor agreement was found between the results from the visual inspection and the automatic routine. For 30 August 2005 only the start of the elevating CBL was reproduced, whereas the growing CBL was not seen at all for 11 September 2005 in the output of the automatic routine, which equalled the second criterion H_2 . The first criterion H_1 rose in the forenoon hours, even though a bit delayed to the growth of the CBL as derived from visual inspection. Only for 5 September 2005 results matched well until noon. In the evening hours no general picture of agreement was found, as for 30 August 2005 results were quite satisfying, whereas for the other days deviations were larger for the early evening hours and got smaller towards midnight. In the evening, the first criteria H_1 more often determined the final output of the automatic routine.

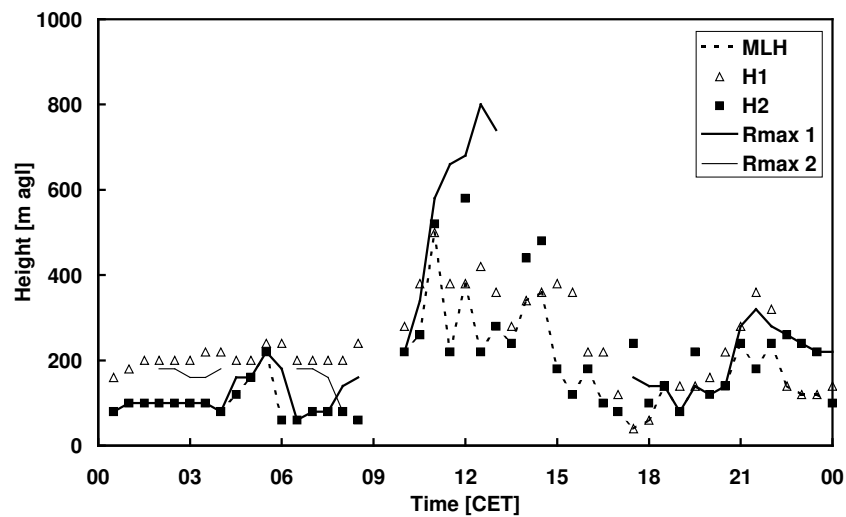


Figure 4-19: ABL depths derived from the automatic detection from sodar measurements (MLH, H1, H2 after Emeis and Türk, 2004) as well as Rmax 1 and Rmax 2 as determined by visual inspection from the profile of reflectivity for 30 August 2005.

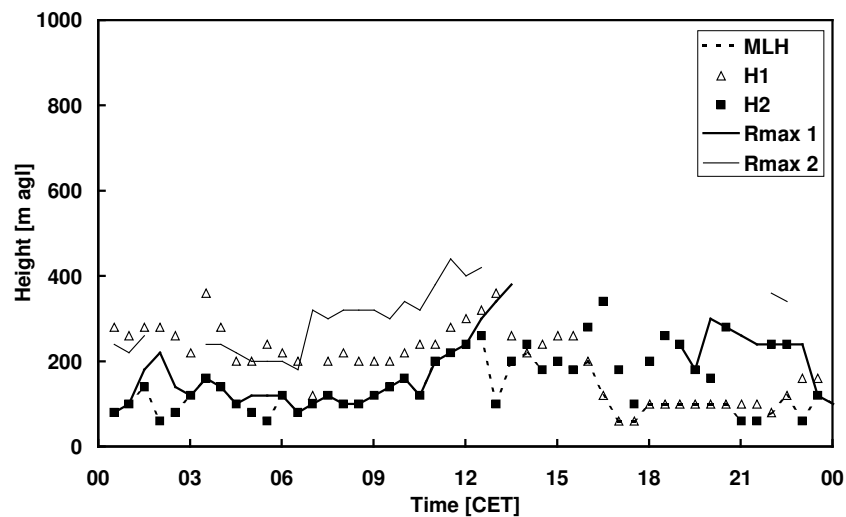


Figure 4-20: Same as Figure 4-19 for 5 September 2005.

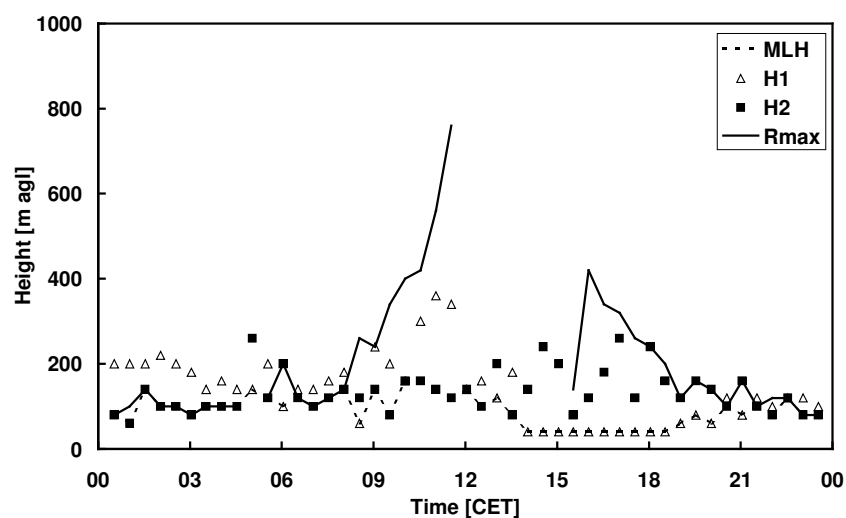


Figure 4-21: Same as Figure 4-19 for 11 September 2005.

Table 4-3: Statistical measures for the comparison of the outputs of the automatic routine to the lowest elevated maximum of reflectivity. Outputs of the automatic routine are: MLH (the ABL height) and H1 and H2 (criteria used in the routine). Only data from 0 CET until 13:30 CET was used for the statistical analyses. (MAE = mean absolute error [m], RMSE = root mean square error [m], MPB = mean percent bias [%]).

all (N = 73)				30.08.2005 (N = 24)			
	MLH	H1	H2		MLH	H1	H2
MAE	73	109	68	MAE	94	126	85
RMSE	159	137	154	RMSE	191	161	182
r ²	0.41	0.51	0.41	r ²	0.61	0.81	0.58
MPB	-19	55	-18	MPB	-20	60	-19

05.09.2005 (N = 27)				11.09.2005 (N = 22)			
	MLH	H1	H2		MLH	H1	H2
MAE	30	95	30	MAE	103	108	95
RMSE	69	106	69	RMSE	195	141	192
r ²	0.36	0.36	0.36	r ²	0.16	0.44	0.14
MPB	-13	74	-13	MPB	-26	28	-22

Statistical analyses were performed for the comparison of outputs of the automatic routine and the ABL height determined from reflectivity profiles (Table 4-3). Here, only data from 0 CET until 13:30 CET was used due to the uncertainties in the determination during the evening hours. The overall agreement was not unanimous for the whole data set as well as for single days. Coefficients of determination r^2 were better for the first criterion H_1 than for the final result MLH. Considering the other statistical values, it is seen that only the correlation was better for H_1 whereas the mean absolute error MAE was larger for H_1 than for H_2 and MLH. The first criterion H_1 overestimated the ABL height as determined by visual inspection, whereas the second criterion H_2 as well as the MLH underestimated the ABL height. The very similar results for MLH and H_2 show that the final results were mostly determined by the second criterion H_2 .

As threshold values were system specific values, the ones used in the original version of the automatic routine may not be appropriate for the system used in this study. Therefore, an adjustment was made to advance the results of the automatic routine. The structure of the automatic routine was maintained. Several combinations of threshold values were tested with data from all three days, but only considering data from midnight until 13:30 CET as confidence in the evening hours was not good. Resulting root mean square errors RMSE and coefficients of determination r^2 were compared and a minimum of RMSE and a maximum of r^2 was aimed. For individual days, different sets of threshold values achieved best results. The following modified criteria, in which threshold values were reduced compared to the original version, resulted in r^2 larger than 0.7 for all individual days.

$$H_{1,\text{mod}} = z, \text{ if } (R(z) < 83 \text{ dB and } R(z+1) < 81 \text{ dB and } R(z+2) < 79 \text{ dB}) \quad (4-2)$$

$$H_{2,\text{mod}} = z, \text{ if } (\delta R/\delta z(z+1) < 0 \text{ and } \delta R/\delta z(z-1) > 0 \text{ and } \sigma_w < 0.4 \text{ m s}^{-1}) \quad (4-3)$$

The second part of the second criterion was not changed.

These criteria were chosen even though the overall performance was better with a different combination, but performance was very different for individual days. Equal performance for all three days was considered to be more important than a better overall performance.

It was aimed to advance the results especially in the forenoon and noon hours to better reproduce the growth of the CBL, as during morning hours already reasonable outputs were obtained and in the evening hours high uncertainties occurred. From Figure 4-22, Figure 4-23 and Figure 4-24 it is apparent that this aim was realised. At night time, no changes occurred, whereas the evolution of the CBL in the morning and forenoon hours was much better reproduced in all three cases. In the evening hours, only little changes were found which did not improve the results much. But as stated above, this was not the aim of the modification.

Statistical analyses were performed in the same way as described above for the original version of the automatic routine (Table 4-4). With the modified routine, the second criterion H_2 was not fulfilled in all cases. Therefore, the statistical analysis for H_2 was based on less data points than for the final result MLH and the first criteria H_1 . When compared to Table 4-3, the improvement for the first half of the day was clearly seen. Correlation for MLH was much better than before and errors were smaller. The output MLH from the automatic routine still underestimated the results from the elevated maximums of reflectivity, but to a lesser extent than before. In most cases MLH was still determined by H_2 , as can be seen from the similar results for MLH and H_2 . Correlation of H_1 got better and errors got smaller, except for 5 September 2005, but the overestimation increased.

These results demonstrated that the ABL could be obtained by automatic methods only to some extent. The modified version of the automatic routine suggested by Emeis and Türk (2004) achieved reasonable results for the first half of the day. The fact that better results could be obtained for every individual day with different threshold values stresses that automatic detection of the ABL height is a non-trivial problem. Furthermore it is obvious that results from the automatic detection have to be critically examined. Beyrich (1997) stated that results from any automatic ABL height detection have to be checked by a trained analyst before being used as input to dispersion models. Even though more time-consuming and more subjective, the visual inspection of reflectivity profiles seemed to be the most reliable method to determine the ABL height.

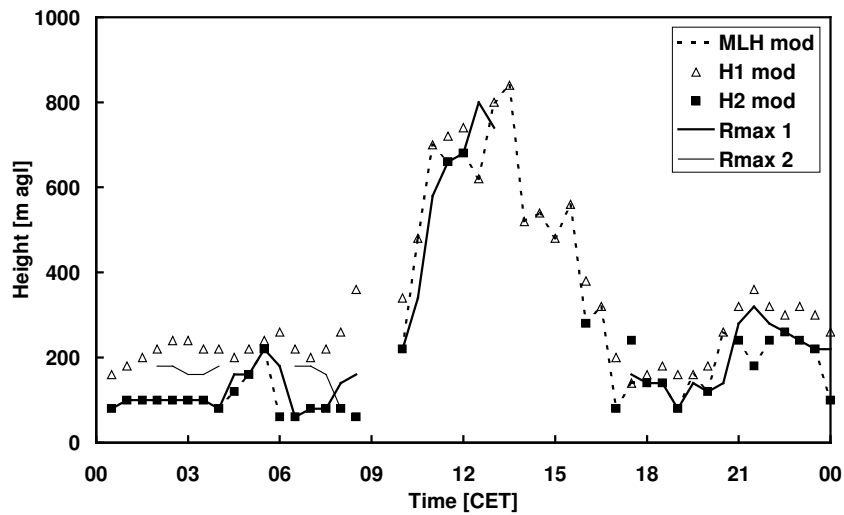


Figure 4-22: ABL heights derived from the modified automatic detection from sodar measurements (MLH mod, H1 mod, H2 mod) as well as Rmax 1 and Rmax 2 as determined by visual inspection from the profile of reflectivity for 30 August 2005.

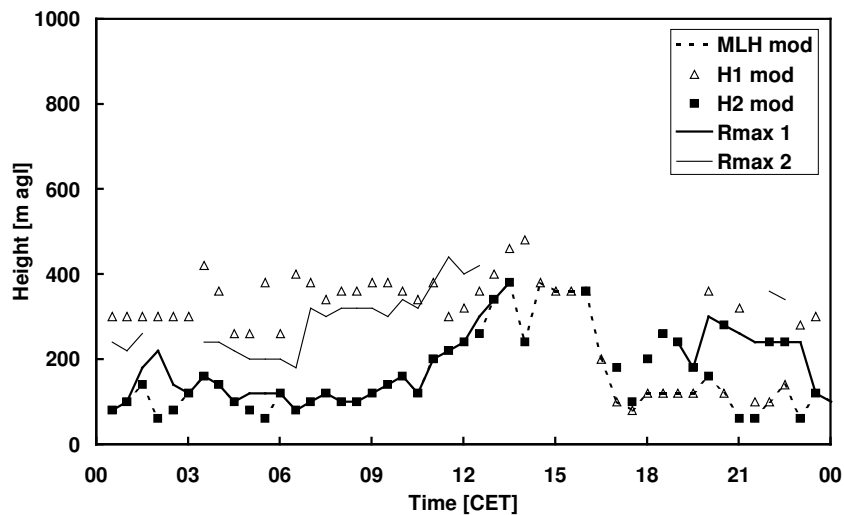


Figure 4-23: Same as Figure 4-22 for 5 September 2005.

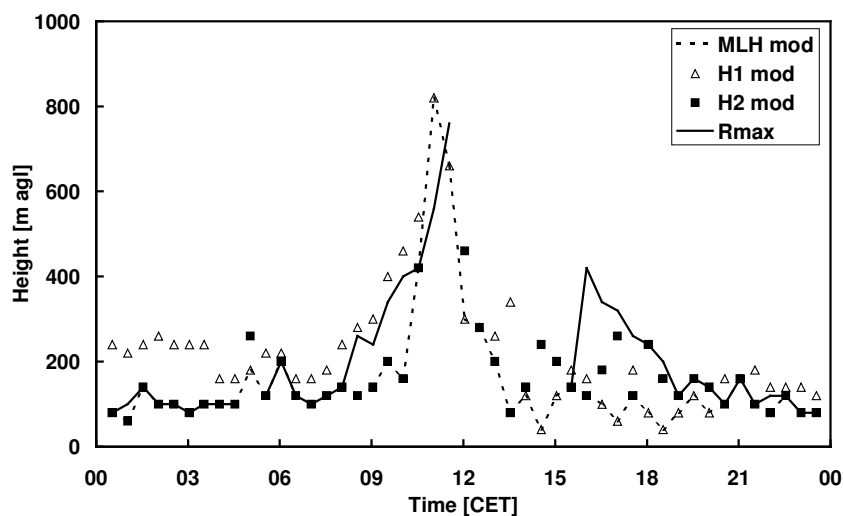


Figure 4-24: Same as Figure 4-22 for 11 September 2005.

Table 4-4: Statistical measures for the comparison of the outputs of the modified automatic routine to the lowest elevated maximum of reflectivity. Outputs of the automatic routine are: MLH (the ABL height) and H1 and H2 (criteria used in the routine). Only data from 0 CET until 13:30 CET was used for the statistical analysis. The second number of cases N applies to the second criteria H2 as this criteria was not fulfilled in all cases. (MAE = mean absolute error [m], RMSE = root mean square error [m], MPB = mean percent bias [%]).

all (N = 73, 67)				30.08.2005 (N = 24, 20)			
	MLH	H1	H2		MLH	H1	H2
MAE	25	127	17	MAE	27	101	16
RMSE	55	146	42	RMSE	53	111	38
r ²	0.88	0.77	0.85	r ²	0.93	0.92	0.96
MPB	-9	108	-10	MPB	-6	89	-11

05.09.2005 (N = 27, 27)				11.09.2005 (N = 22, 20)			
	MLH	H1	H2		MLH	H1	H2
MAE	15	183	15	MAE	35	86	21
RMSE	37	197	37	RMSE	73	98	50
r ²	0.82	0.14	0.82	r ²	0.78	0.85	0.61
MPB	-9	151	-9	MPB	-12	73	-10

4.4.3 Comparison of ABL heights inferred from sodar and balloon data

Tethered balloon soundings were performed next to the sodar/RASS measurements on selected days. In this study, only meteorological data for 5 September 2005 during the morning hours were analysed.

The evolution of the virtual potential temperature profile from 5 CET to 10 CET is shown in Figure 4-25. During the night strong cooling has occurred as a strong inversion is seen over the whole profile in the early morning hours. The first profile had an exponential shape, with very strong gradients in the lowest 100 m of about 75 K km^{-1} and smaller gradients of about 23 K km^{-1} above that. The ABL height from sodar data was detected approximately at the height where the gradient changed, which coincided with the SBL height determined from the profile of virtual potential temperature being at the height of the first discontinuity in the profile. A complex structure was observed in the virtual potential temperature profile with several steps marking heights of stronger inversions. It is not clear whether the top of the inversion was reached by the balloon sounding or not. 5 September 2005 by far exhibited the coldest night time temperatures out of the three golden days whereas maximum temperatures by day nearly reached the values measured for 30 August 2005. At all measuring stations, largest temperature amplitudes were measured at this day. During the first six profiles until 8:30 CET similar developments were observed. Warming not only took place from below due to solar radiation but was also observed over the whole profile. Above 100 m agl the original temperature gradient

was more or less maintained, even though temperatures increased, which indicates subsidence heating. An inversion top seemed to descend from above in successive profiles. These observations of a successive downward displacement of the virtual potential temperature curve resemble pattern 3 of inversion destruction as outlined in the study done by Whiteman (1982) in mountain valleys. In the balloon sounding from 08:14 until 08:34 CET the CBL could be seen for the first time reaching a depth of about 100 m. The shape of this virtual potential temperature profile was layered with a stable layer above the CBL reaching up to 300 m agl covered by a more stable lid. Air in the layer above became almost neutral. The evolution of the CBL is seen very well in the following two profiles, reaching a depth of 150 m agl in the last sounding. Above the CBL, warming was not observed any more. On the contrary, the layer above the CBL up to 300 m agl was cooled and became neutral. Cooling of the air was detected up to 400 m agl. The change of the wind direction that was attributed to Alpine pumping occurred at approximately 8:00 CET at the surface and at 9:30 CET at 300 m agl. The onset of the plain to mountain flow was accompanied by a drop in temperature, that was detected at all surface measuring stations including the MOHp. The cooling of the profiles around that time might have been caused by the reversal of the wind direction and the advection of colder air from the lower regions of the Alpine foreland.

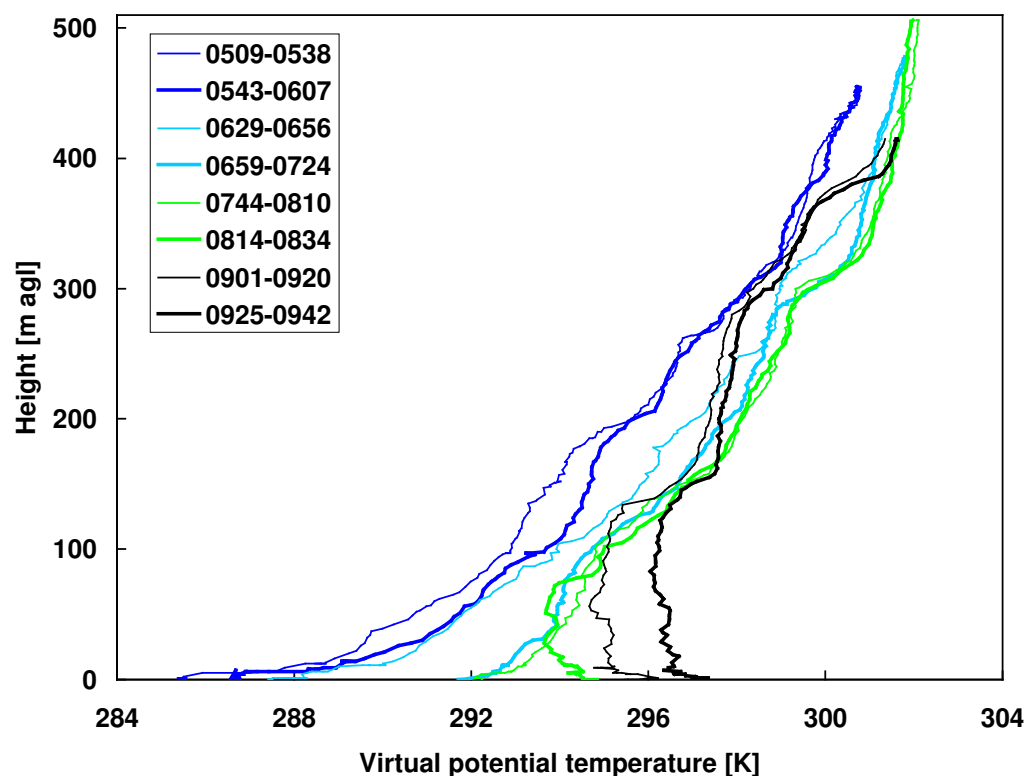


Figure 4-25: Virtual potential temperature profile evolution from tethered balloon data for 5 September 2005. Balloon ascents are marked by thin lines, descents by thick lines. Flights are labelled by the corresponding flight times [CET].

Reflectivity profiles, averaged over the duration of the tethered balloon flights, were compared to virtual potential temperature profiles (Figure 4-26) and to specific humidity profiles (Figure 4-27) measured by the tethered balloon system. Reflectivity profiles showed a complex structure with multiple layers as well.

The first reflectivity profile (08:14-08:34 CET) exhibited three maximums, at 100 m, 160 m and 320 m agl. The first and the third maximum coincided well with the transitions between the layers marked by inversions in the virtual potential temperature profile as described above. Distinct points in wind profiles (not shown here) occurred at the heights of these maximums, with wind speed maximums in 70 m and 320 m agl in the balloon data and in 100 m and 320 m agl in the sodar data. The second maximum in the reflectivity profile was associated with the transition zone between the plain to mountain wind layer of easterly to north-easterly winds and the westerly winds aloft. A jump in humidity coincided with the third maximum of reflectivity in 320 m agl.

Two maximums of reflectivity appeared in the second profile (09:01-09:20 CET). The lower maximum at 140 m coincided well with the CBL depth as determined from the virtual potential temperature profile. The second maximum of reflectivity did not have a distinct peak, it is more a zone of elevated reflectivity with the highest values between 300 m and 340 m agl. A temperature inversion above a layer of nearly neutral stratification occurred at the same height range. Again, distinct points in profiles of other meteorological parameters were found approximately at the level of the maximums of reflectivity. The transition of wind direction at the top of the plain to mountain wind layer happened between 330 m and 350 m agl (not shown here), whereas the humidity profile showed a layered structure with jumps in humidity at 140 m and 280 m agl. A well defined maximum occurred in the humidity profile between 280 m and 310 m agl. Above that, humidity decreased.

In the third profile (09:25-09:42 CET) three maximums of reflectivity were observed again. The lower two maximums were very distinct at 160 m and 300 m agl, whereas the third maximum between 360 m and 380 m agl was less pronounced. The shape of the virtual potential temperature profile indicated a layered structure of the ABL, with the CBL reaching up to 160 m agl, the second layer up to 300 m agl and the third layer up to 380 m agl, each confined by a temperature inversion. Again, the structure of the reflectivity profile coincided well with the structure of the virtual potential temperature profile. Three layers of nearly constant humidity were exhibited in the humidity profile with steps occurring at the same height as the maximums in reflectivity for the first and third layer. The second layer was topped by a local maximum at 290 m agl.

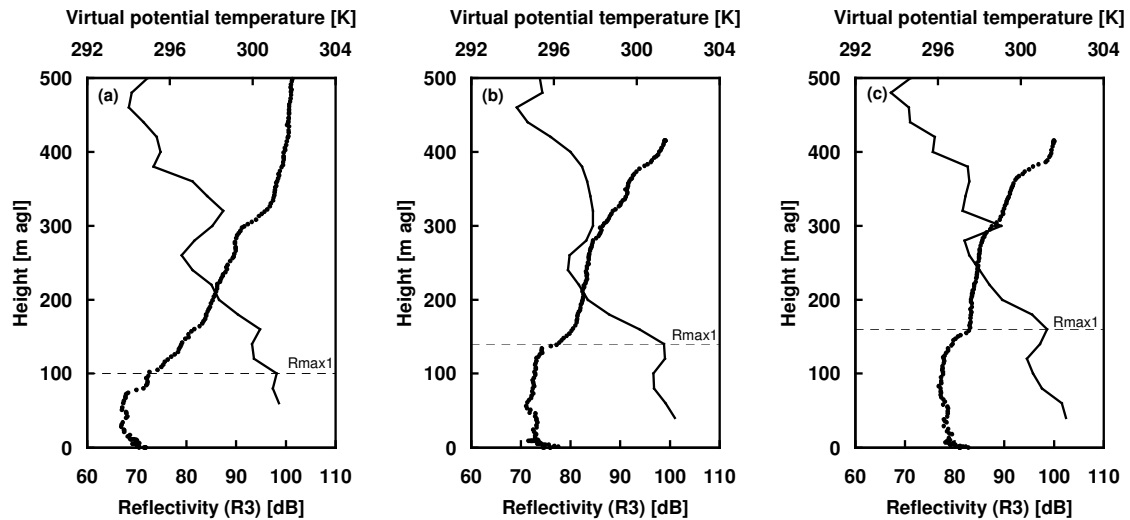


Figure 4-26: Simultaneously measured profiles of virtual potential temperature measured by tethered balloon soundings (dots) and profiles of reflectivity measured by sodar (line) on 5 September 2005 ((a): 08:14-08:34 CET, (b): 09:01-09:20 CET, (c): 09:25-09:42 CET). The dashed line marks the CBL depth derived from the reflectivity profile (R_{max1}).

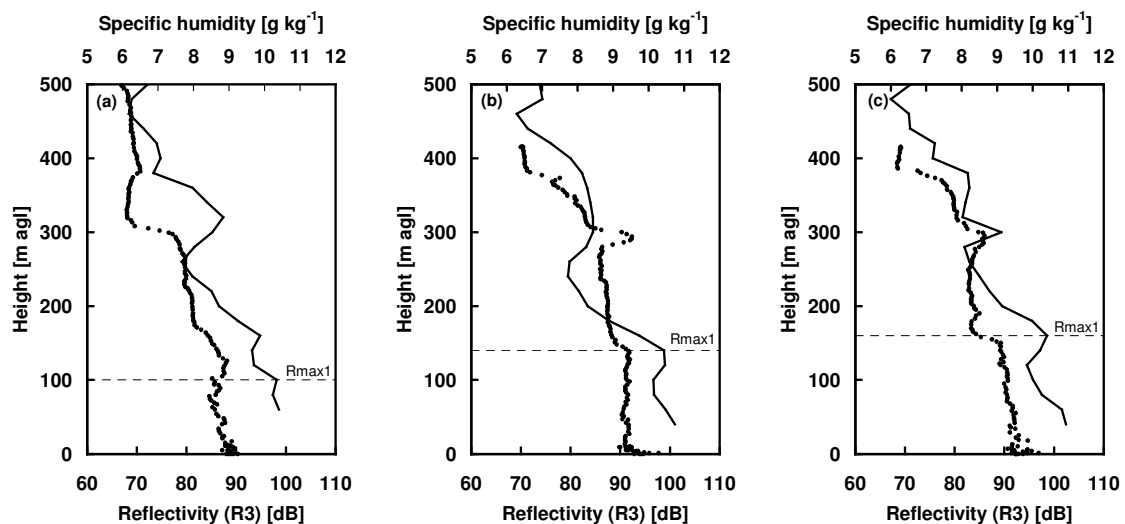


Figure 4-27: Simultaneously measured profiles of specific humidity measured by tethered balloon soundings (dots) and profiles of reflectivity measured by sodar (line) on 5 September 2005 ((a): 08:14-08:34 CET, (b): 09:01-09:20 CET, (c): 09:25-09:42 CET). The dashed line marks the CBL depth derived from the reflectivity profile (R_{max1}).

Comparison of these three profiles of sodar reflectivity data as well as meteorological data measured by tethered balloon sondes demonstrated the good agreement regarding the complex structure of the ABL. The coincidence of the lowest local maximum of reflectivity with the CBL depth as determined by the simple parcel method from the virtual potential temperature profile measured by the tethered balloon sonde supports the assumption that the first maximum during the evolution of the CBL at 5 September 2005 marks the top of the CBL as was made in section 4.4.2.1.

Profiles measured at 5 September 2005 exhibited typical features that were reported in complex terrain. A complex structured ABL is typical for complex terrain, resulting in a

number of local maximums in the reflectivity profile measured by sodar. Several local maximums in reflectivity profiles were also observed by Beyrich et al. (1996) who found good agreement between sodar data and meteorological as well as ozone profile measurements over the complex terrain in the Upper Rhine Valley, Germany. A layered structure in temperature profiles was also reported elsewhere. De Wekker et al. (2005) observed three layers in the daytime in the steep Riviera valley, Italy. The lowest layer was rather well-mixed, representing the CBL. Up to about ridge height, a middle stable layer occurred, becoming more stable near its top. Aloft, almost neutral conditions were found. Even though not located in a steep valley, the potential temperature profile at Hohenpeißenberg had a somewhat similar structure in a smaller scale. The top of the middle layer was located approximately at the height of the mountain top. In the Riviera valley, warming of the air was also not confined to the CBL, as also reported by Chemel and Cholet (2005) for the Chamonix valley. This typical feature of inversion destruction has been described by Whiteman (1982) as pattern 3 that usually occurs in valleys when the snow cover is absent. It is obvious that the destruction of the inversion as observed in Hohenpeißenberg did not reflect the pattern 1 that is usually observed over flat terrain. Even though a lot of similarities to typical mountain valley conditions were found, observations like the cooling of the air after the onset of the plain to mountain flow did not match a steep valley situation. On 5 September 2005 the CBL growth is decelerated in comparison to the other two days. Low growth rates of the CBL were not only reported in steep valleys, but also in cases with a strong surface-based nocturnal inversion (Coulter, 1979). He stated that after clear nights that are subject to subsidence and radiational cooling the CBL only slowly grew in spite of relatively strong heating. Such a strong nocturnal inversion was observed on 5 September 2005. Another possible reason for the low growth rates was described by Kossmann et al. (1998). Cold air advection by the upslope wind decelerated the CBL growth due to its influence on the heat budget near the ground. Such cold air advection was observed after the onset of the plain to mountain circulation by a drop in temperature at all measuring stations. On 5 September 2005, cold air advection, subsidence as well as a strong nocturnal surface inversion might have influenced the slow growth rates of the CBL.

4.4.4 Parameterisations of the SBL height

For the calculation of SBL depths, a very limited number of only 13 half-hourly cases remained after applying the selection criteria as described in section 3.4.1. These cases were very unevenly distributed, with 4 cases for 30 August, 1 case for 5 September and 8 cases for 11 September 2005. Quality flags were widely distributed with nearly all classes covered (Table 4-5). Due to the very limited number of cases, quality flags were not taken as a selection criteria, even though the quality of several data points was quite poor and should only have been used for orientation (class 7 and 8; Foken et al., 2004).

Table 4-5: Distribution of quality flags after Foken et al. (2004) for the friction velocity u_* and the buoyancy flux for the 13 half-hourly cases used for the parameterisations of the SBL depth.

Quality flag	1	2	3	4	5	6	7	8	9
u_*	1	0	3	0	8	0	1	0	0
Buoyancy flux	2	1	1	1	0	2	1	5	0

All 16 formulations were tested for the 13 cases and compared to the SBL depth as observed from the sodar measurements (secondary elevated maximum of reflectivity). Correlation of observed and predicted values was very poor for all equations (Table 4-6). Best correlation was observed for SWH(4). All equations but SWH(4) underestimated h , in most cases considerably. Mean absolute errors MAE and root mean square errors RMSE were lowest for equation SWH(3) and the simpler equations such as $700 \cdot u_*$ and VM(4). Multi-limit equations (VM(6), VM(7), HFK(19)) exhibited the largest errors and largest underestimations. Scatter plots are shown in Figure 4-28 for four exemplary equations.

Table 4-6: Statistical measures for the comparison of observed and predicted SBL depths [m agl] for the whole dataset (N = 13). Abbreviations for SBL depth formulations as described in section 2.3.4.2. Abbreviations for statistical measures see Table 4-4. Bold numbers mean the best quality for the particular statistical quantity.

Parameterisation	mean	MAE	RMSE	r^2	MPB
$700u_*$	64	46	54	0.082	-36
VM(1)	84	36	45	0.082	-16
VM(2)	36	83	88	0.060	-62
VM(3)	51	65	72	0.055	-48
VM(4)	93	33	42	0.010	-8
VM(5)	40	66	72	0.004	-61
VM(6)	16	90	94	0.018	-84
VM(6/2)	17	90	93	0.011	-83
VM(7)	11	95	99	0.023	-89
VM(8)	30	77	83	0.054	-69
VM(9)	71	66	77	0.047	-27
VM(10)	33	76	82	0.055	-67
VM(11)	34	73	80	0.043	-66
VM(11/2)	31	75	82	0.037	-69
SWH(3)	88	28	37	0.039	-13
SWH(4)	136	35	51	0.103	31
HFK(19)	15	91	95	0.020	-85
Observed (sodar)					
Rmax	106				

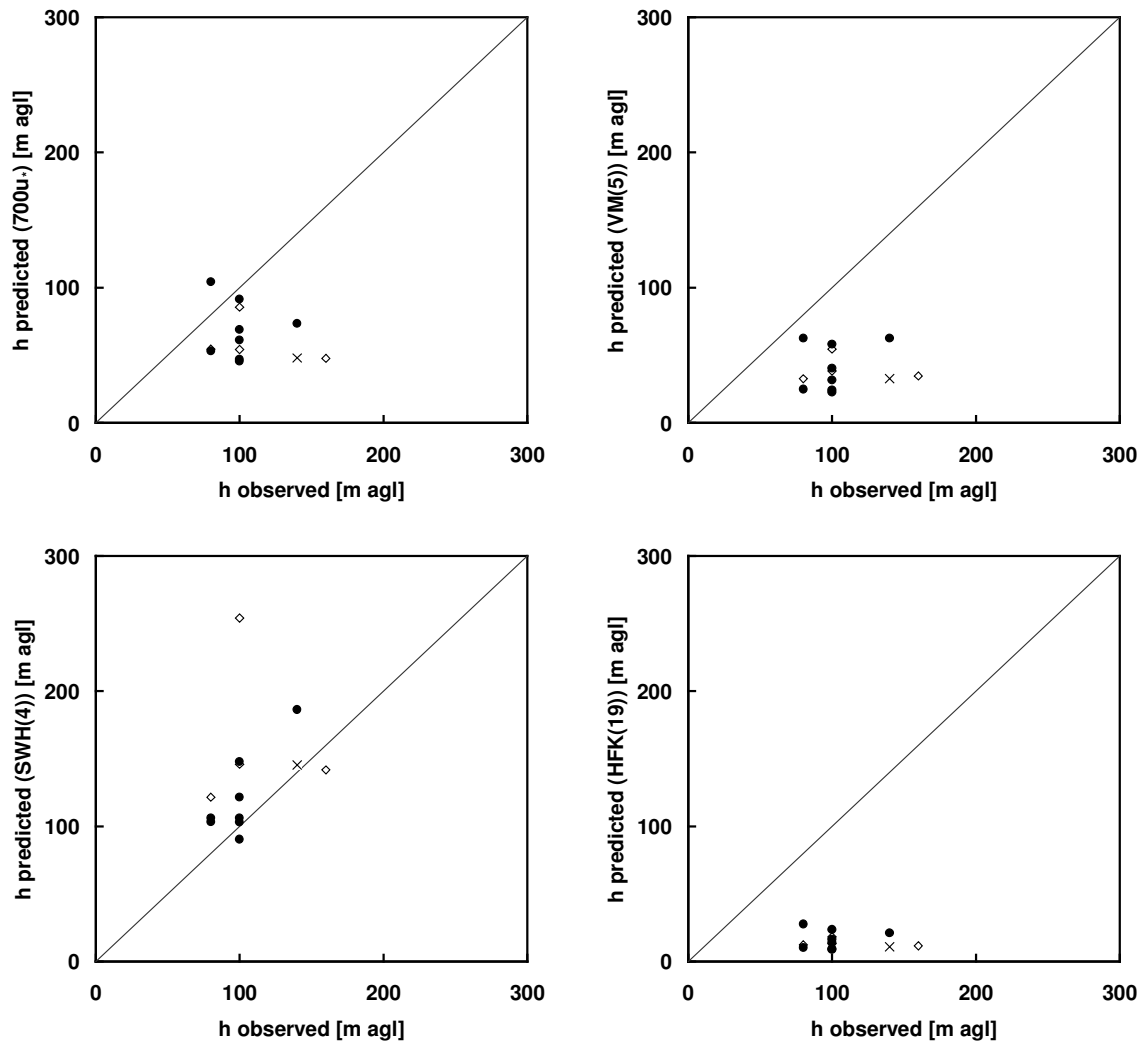


Figure 4-28: Predicted h [m agl] vs observed h [m agl] for stable boundary layer depth formulations described in the text with parameters in Table 2-1 and Table 2-2 for 30 August (white diamonds), 5 September (cross) and 11 September 2005 (black circles).

The boundary layer station and the location of the turbulence measurements at the meadow station were separated by about 1.1 km and there was a difference in elevation of 30 m. In the analysis shown above, this spatial separation was not taken into account. Meteorological conditions were quite different at these two stations with temperatures being frequently considerably colder at the boundary layer station than at the meadow station during nights and warmer during the day. As the SBL is assumed to be horizontal and not terrain following in complex terrain (see section 2.3.3), it might be important to consider the difference in elevation, which is not negligible regarding absolute SBL depths. Thus, SBL heights in m asl were calculated and observed SBL heights were compared to predicted SBL heights. Obviously, correlations could not be improved. But results clearly got better in terms of errors and bias (Table 4-7). Mean percent bias MPB did not indicate a general underestimation any more, even though 11 equations still underestimated observed values. Comparison of absolute values of MPB with the ones calculated above has to be done with caution as the absolute value of the SBL height is much larger than the

absolute value of the SBL depth. Errors were smaller when comparing SBL heights to SBL depths. Again, smallest errors occurred for the simpler equations ($700 \cdot u_*$, VM(1), VM(4)), whereas multi-limit equations exhibited the largest errors. Equation SWH(3) derived from dimensional analysis yielded similar results than the simpler equations mentioned before. Four exemplary scatter plots are shown in Figure 4-29.

Unfortunately, this study was based on a very limited number of data points, which are generally too few to carry out sound statistical analyses. Thus, correlation measures were especially of no value in estimating the performance of the equations. When comparing scatter plots as observed in this study (Figure 4-28 and Figure 4-29) to scatter plots displayed in the literature (e.g. Vickers and Mahrt, 2004; Steeneveld et al., 2006a, 2006b), the scatter does not seem to be much larger. Considering the values of SBL depths ranging between 80 m and 160 m, the vertical resolution of 20 m of the sodar data was quite large. Additionally taking into account the uncertainties in the determination of the SBL depth from sodar reflectivity data, a mean absolute error of 30 m seems to be reasonable.

Table 4-7: Same as Table 4-6 but difference in elevation considered (SBL heights [m asl]).

Parameterisation	mean	MAE	RMSE	r^2	MPB
$700u_*$	807	27	36	0.082	-1
VM(1)	827	30	39	0.082	1
VM(2)	779	58	66	0.060	-5
VM(3)	794	43	52	0.055	-3
VM(4)	836	34	43	0.010	2
VM(5)	783	38	45	0.004	-4
VM(6)	759	60	66	0.018	-7
VM(6/2)	760	60	65	0.011	-7
VM(7)	754	65	70	0.023	-8
VM(8)	773	51	57	0.054	-6
VM(9)	814	46	69	0.047	0
VM(10)	776	51	56	0.055	-5
VM(11)	777	48	54	0.043	-5
VM(11/2)	774	49	55	0.037	-5
SWH(3)	831	28	35	0.039	2
SWH(4)	879	60	73	0.103	7
HFK(19)	758	61	66	0.020	-7
Observed (sodar)					
Rmax	819				

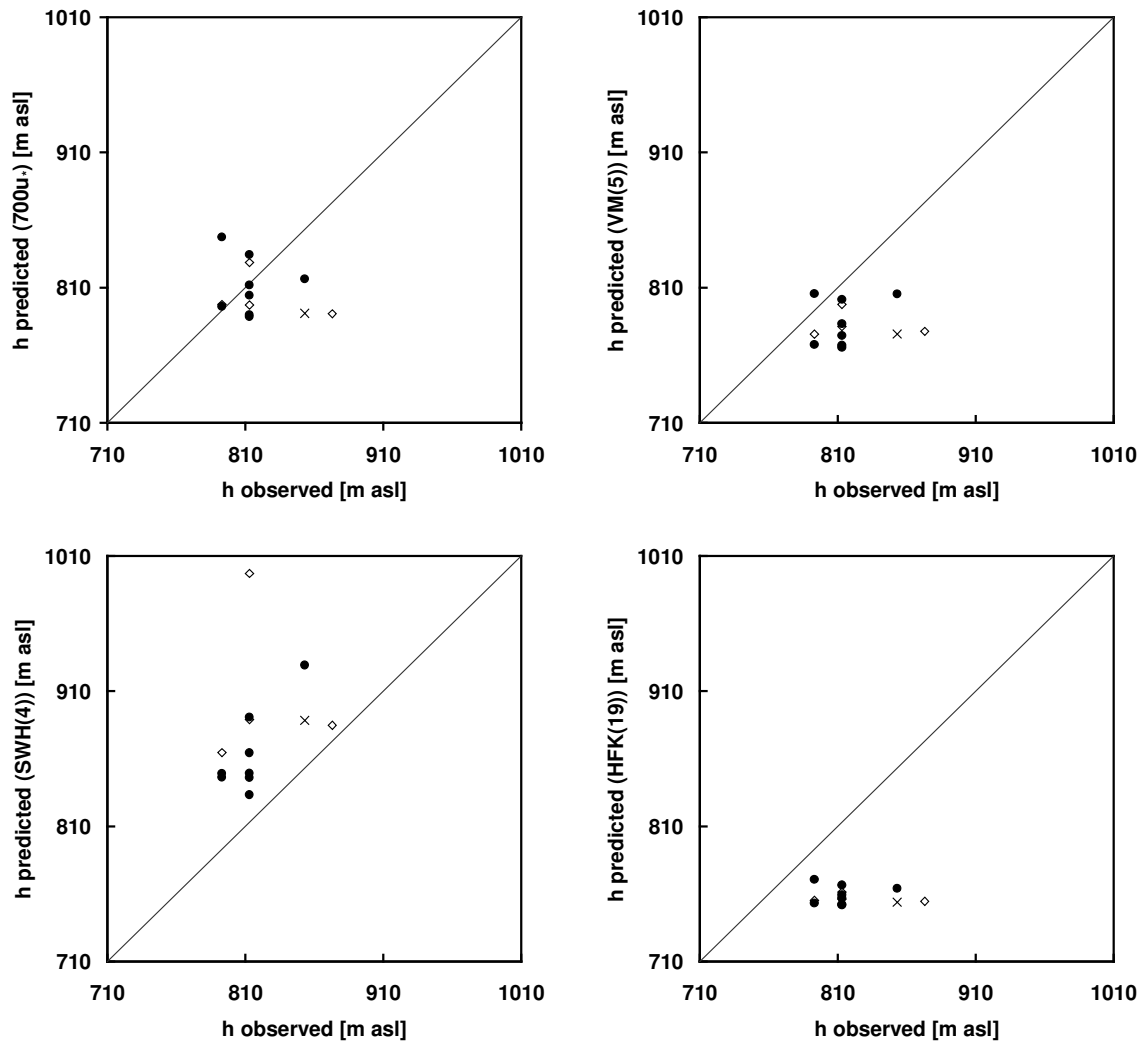


Figure 4-29: Same as Figure 4-28 but difference in elevation considered (SBL heights [m asl]).

It appeared to be very important to distinguish between the ABL height and the ABL depth in stable conditions in the complex terrain of Hohenpeißenberg. Assuming a vertical SBL height and accounting for the difference in elevation between the sodar and the turbulence measurement site, some of the surface flux formulations yielded sound results. The simpler equations performed much better than more complicated equations. Only taking into account the friction velocity already yielded good results (700- u_* , VM(1)), indicating the relevance of u_* . Steeneveld et al. (2006a) found the friction velocity u_* to be the dominant quantity on the SBL depth after performing a principal component analysis. The freeflow stratification N appeared to be the second important quantity. The good performance of equation VM(4) and VM(5) indicated as well that the freeflow stratification N is another relevant parameter for this data. In contrast to Vickers and Mahrt (2004) who found an overestimation for nearly all equations, in this study, even for the data corrected for the difference in elevation, underestimation was observed for most of the formulas. Coefficients as taken from the literature may not have been appropriate for the prevailing conditions, as some of them were determined using data from Antarctic stations.

But the dataset of only 13 data points was too small to do a sound recalculation of coefficients.

4.4.5 Slab models for the CBL height

The growth of the CBL was modelled with four different slab models (Gryning and Batchvarova, 1990b; Yi et al., 2001; Schipper et al., 2002) as presented in section 2.3.4.3. Formula (2-33) and (2-31) required the vertical gradient of potential temperature γ above the CBL. Radiosonde data between 1000 m and 3500 m agl were used to determine this parameter (Table 4-8), as temperature data from the sodar/RASS did not cover the height range needed for the determination. The lowest value of the gradient of 3.3 K km^{-1} was measured on 5 September 2005 whereas the highest value was observed on 30 August 2005 with 5.2 K km^{-1} . These values are within the range reported in literature. Other input data were the bouyancy flux and friction velocity measured at the meadow.

For each day, model results are presented together with results from the determination of the ABL depth from sodar reflectivity data (Figure 4-30, Figure 4-31 and Figure 4-32). On 30 August 2005 good agreement of modelled and observed ABL depths was found for the first hours until 6:30 CET and after 11 CET for nearly all equations (Figure 4-30). The final values after noon were quite well reproduced except for equation (2-34) ($z_i(2)$) with the parameters determined by Yi et al. (2001) which overestimated the CBL depth. In the morning hours after 6:30 CET the observed CBL depth was much lower than the modelled CBL depth. As final values were more or less the same, the growth rate in the model was lower than in the observations, where the CBL growth rate got large after 10 CET. Caution has to be paid regarding the lack of data after 8:30 CET.

On 5 September 2005 the very shallow ABL was reproduced by all equations reasonably well until 7:30 CET (Figure 4-31). After that, all models predicted a large growth rate and maximum CBL depths reached at 13:30 CET lay between 820 m and 1020 m agl. Models highly overestimated CBL depths as the maximum observed CBL depth at that time amounted to only 340 m agl.

On 11 September 2005 modelled and observed CBL depths agreed best (Figure 4-32). Modelled and observed growth rates were similar and CBL depths from the models coincided reasonably well with observed CBL depths until 11 CET. Unfortunately, later on determination of the CBL depth from reflectivity profiles was not possible any more for most of the profiles.

Table 4-8: Average lapse rates γ [K km^{-1}] determined from all potential temperature radiosonde profiles of the respective day between 1000 and 3500 m agl.

	γ [K km^{-1}]
30 August 2005	5.2
5 September 2005	3.3
11 September 2005	4.1

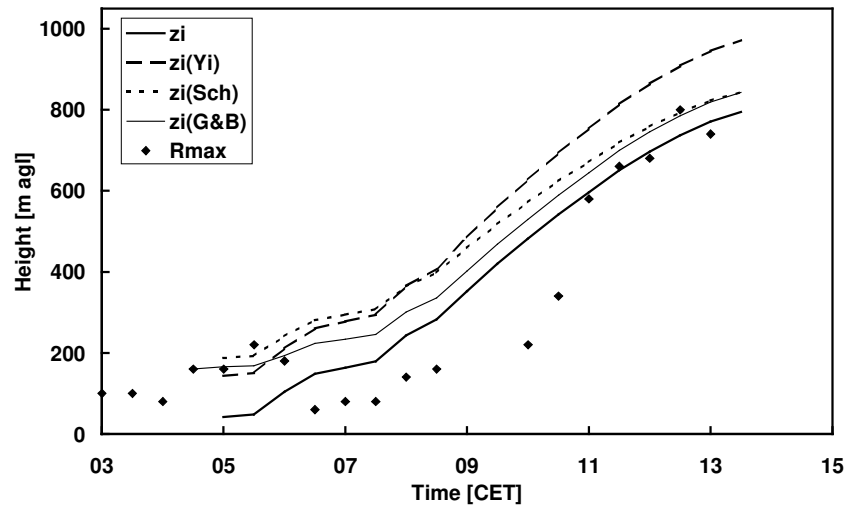


Figure 4-30: Development of the CBL for 30 August 2005 from sodar data (Rmax) and modelled by slab models. (Abbreviations: z_i = equation (2-33), $z_i(Y_i)$ and $z_i(Sch)$ = equation (2-34), using coefficients by Yi et al. (2001) and Schipper et al. (2002) respectively, $z_i(G\&B)$ = equation (2-31).)

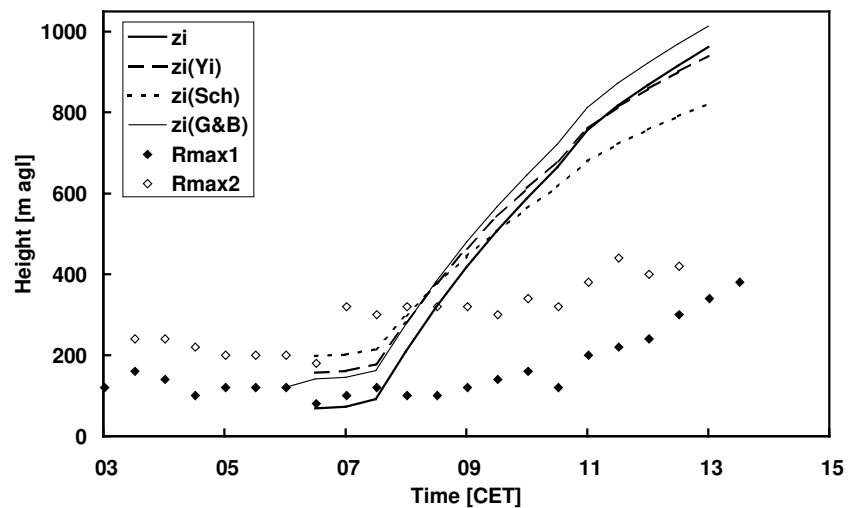


Figure 4-31: Same as Figure 4-30 for 5 September 2005.

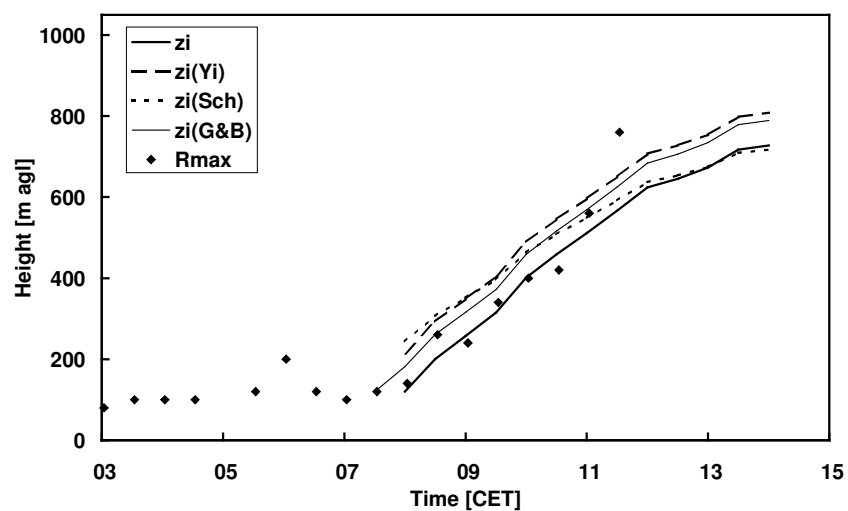


Figure 4-32: Same as Figure 4-30 for 11 September 2005.

Table 4-9: Statistical measures for the comparison of observed and modelled CBL depths. (Abbreviations: z_i = equation (2-33), $z_i(Y_i)$ and $z_i(\text{Sch})$ = equation (2-34), using coefficients by Yi et al. (2001) and Schipper et al. (2002) respectively, $z_i(\text{G\&B})$ = equation (2-31)). Bold numbers mean the best quality for the particular statistical quantity.

		z_i	$z_i(Y_i)$	$z_i(\text{Sch})$	$z_i(\text{G\&B})$
all N=37	MAE	187	208	238	214
	RMSE	278	264	304	310
	r^2	0.29	0.42	0.43	0.29
	MPB	85	127	132	123
30.08.2005 N = 15	MAE	97	146	186	114
	RMSE	120	180	212	144
	r^2	0.82	0.82	0.82	0.86
	MPB	34	104	103	76
05.09.2005 N = 14	MAE	361	346	384	412
	RMSE	430	380	438	478
	r^2	0.76	0.76	0.76	0.77
	MPB	192	213	226	238
11.09.2005 N = 8	MAE	51	81	80	56
	RMSE	76	93	86	70
	r^2	0.89	0.89	0.89	0.89
	MPB	-8	21	22	12

Statistical analyses (Table 4-9) confirmed the best performance of all models for 11 September 2005. Results for that day were best in terms of all statistical measures, such as lowest errors, highest correlations and smallest bias. Correlations were reasonably good for all days, even for 5 September 2005. But that day largest errors and largest overestimations of more than 200% were observed. On 30 September 2005 errors and mean percent bias were large for all models except for equation (2-34) $z_i(1)$. This was the only day that made it possible to judge one of the models to be better than the others, at least in regard to errors and bias. For all other days it was not very obvious which of the models performed best, even though the most simple model (equation (2-34) $z_i(1)$) seemed to give slightly better results. Although correlation coefficients were best for the more complicated model of Gryning and Batchvarova (1990b) for all days considered individually, results of this model did not seem to be superior to the other models. As all other models did not consider mechanical turbulence represented by the friction velocity u_* , but still worked comparatively well, it seems appropriate for these days to only take the buoyancy flux indicating buoyancy production into account. Results of equation (2-34) ($z_i(2)$) with the coefficients determined by Schipper et al. (2002), which is based on a limited data set, appeared to be slightly poorer than results of all the other models, even though the overall performance showed the best correlation.

Contrary to the parameterisations of the SBL depth, the difference in elevation between the boundary layer station and the meadow station where turbulence measurements were performed was not taken into account when comparing modelled and observed CBL

depths. As explained in section 2.3.3, the CBL is considered to be more or less terrain following in the morning. As the CBL is growing, the influence of the terrain becomes less important. Considering CBL depths in the forenoon and around noon, the height difference between the two sites was small making it appropriate to neglect this difference.

5 September 2005 was already described in detail in previous sections and appeared to be a day that was strongly influenced by thermally induced wind systems due to complex terrain, especially the mesoscale circulation Alpine pumping. The CBL models used in this section predicted a very deep CBL. As observed values were much lower than the predicted ones, it becomes obvious that factors other than convective and mechanical turbulence expressed by the buoyancy flux and the friction velocity governed the CBL growth. Factors such as advection and subsidence were neglected by these models. Yi et al. (2001) made an assumption of the influence of subsidence and arrived at a possible reduction of z_i of 20 to 60% when applying equation (2-33). Using equation (4-4), subsidence in terms of the mean large-scale vertical motion \bar{w} can be estimated for 5 September 2005.

$$(\Delta z_i)_{\text{subsidence}} \approx (1 + c) \cdot \bar{w} \cdot t \quad (4-4)$$

The resulting large-scale vertical motion \bar{w} of -0.024 m s^{-1} is well within the range of -0.01 to -0.03 m s^{-1} assumed by Yi et al. (2001). Thus, subsidence might be the reason for the unexpectedly low CBL depths on 5 September 2005. As air from the foreland is “pumped” into the Alps, a downward air mass flux into the CBL has to replace the boundary layer air. Winkler et al. (2004) observed a subsiding aerosol layer with a sinking motion of -0.06 m s^{-1} from lidar measurements in the Alpine foreland during the VERTIKATOR field experiment in 2002 which is considerably larger than the large-scale vertical motion estimated for 5 September 2005. Lugauer et al. (2003) observed even stronger sinking motions at the same day from flight data. The occurrence of subsidence under Alpine pumping conditions was supported by the suppression of convective cloud formation above the foreland as reported by Lugauer and Winkler (2005). Subsidence also suppressed CBL evolution in deep valleys, as explained in Whiteman (1982). Kossmann et al. (1998) modelled the CBL depth with a more complicated equation than used in this study for a valley and a mountain station. Comparison of the modelled with the observed boundary layer depth revealed good agreement for the valley station whereas the CBL depth was largely overestimated at the mountain top, even though both stations received similar input of sensible heat from the ground. They explained this disagreement with the absence of advective processes and only weak large-scale subsidence at the valley site whereas advection was considered to be important at the mountain site. Similarly, on 11 September 2005 good agreement was observed, which was a day with westerly winds and no influence of thermally induced wind systems, i.e. no influence of advective processes or subsidence, whereas on 5 September the CBL evolution is strongly influenced

by the Alpine pumping and associated subsidence and advective processes. On 30 August 2005 phenomena that are linked to complex terrain like the occurrence of a shear layer during the night probably affected the CBL growth in the morning which was delayed in comparison to the modelled CBL evolution.

4.4.6 The ABL height in the Lokal-Modell

Hourly ABL heights were provided by the Lokal-Modell (LM), the operational NWP model of the DWD with a grid-resolution of 7 km. In Figure 4-33, Figure 4-34 and Figure 4-35 the LM output is compared to sodar derived ABL depths. Thereby pbltop values (CBL) were only shown for daytime. Few times during the night on 5 September and 11 September 2005 were pbltop values detected. Generally, these values also depict the RL height. But as these values were unrealistically high, they were not displayed due to better readability of the figures. Similarly, pbstop values are only shown for night time. Sodars values were 30 minute averages marking the end of the 30 minute period, whereas the Lokal-Modell delivered 1-hourly values for every prediction hour, being instantaneous values. On all three days, the SBL depth appeared as a horizontal line with a constant value of 305 m and 306 m agl respectively. This means that no SBL top was detected below 300 m agl by the Richardson number scheme and the SBL depth was set to this fixed value to avoid unrealistically high SBL depths. The CBL depth from LM output compared to sodar derived ABL depths revealed variable performance for the three days. Generally, the onset of CBL growth was late, as the first time a CBL is detected was between 10 to 12 CET. On 30 August 2005 the CBL depth was underestimated by the LM by about 200 m for the second grid point, which represents the grid box the boundary layer station was located at. Large overestimations up to 400 m were observed on 5 September 2005 by the CBL depth from the LM compared to sodar results. On 5 September 2005 the CBL growth started very late (12:00 CET) but exhibited a large growth rate. Best agreement was found on 11 September 2005, even though sodar derived CBL depths were only detected until 11:30 CET.

Problems with the determination of the SBL depth were also found by Fay (2005). Poor estimation of the SBL depth is a general problem of dispersion models and new approaches and parameterisations are needed for NWP models as well as dispersion models (Baklanov et al., 2002). Results for the CBL depth on 30 August and 11 September 2005 are in line with results from a comparison of LM output and measured ABL depths at Lindenberg, Germany. Fay (2005) reported a systematic underestimation, which was largest under convective and front-dominated conditions and in winter. For 119 summer cases in 1997, the average deviation between CBL depths from the LM and determined from radiosoundings amounted to -190 m ($\approx -15\%$). The deviation observed for 30 August coincides well with these observations.

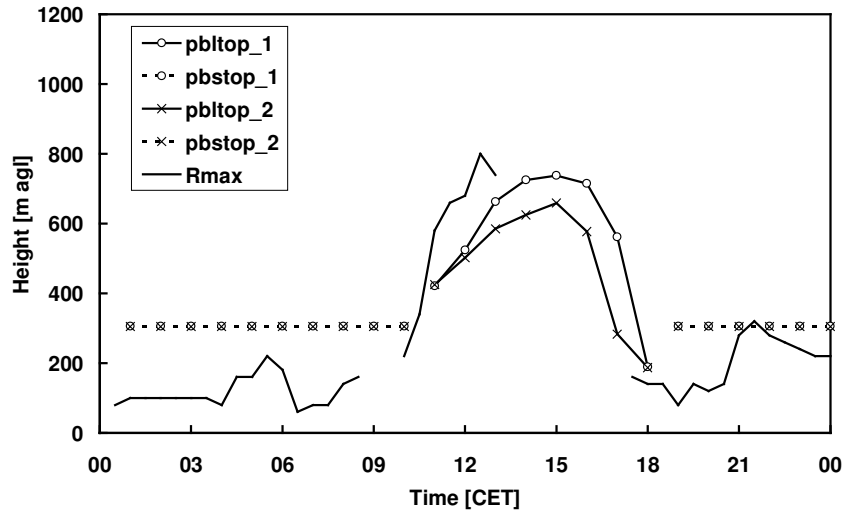


Figure 4-33: ABL depth from Lokal-Modell output for 30 August 2005 in comparison to ABL depths determined from sodar reflectivity profiles (Rmax). pbltop = CBL or RL depth, pbstop = SBL depth. Indices 1 and 2 stand for the two grid points in the vicinity of Hohenpeißenberg.

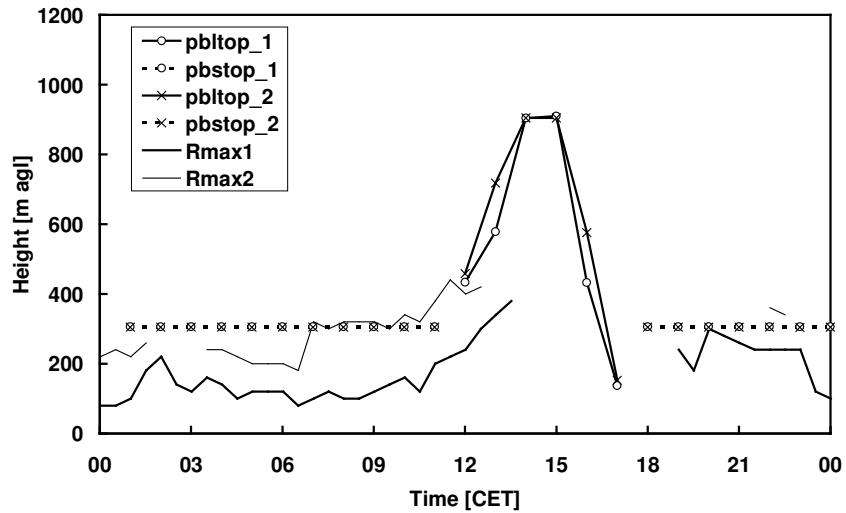


Figure 4-34: Same as Figure 4-33 for 5 September.

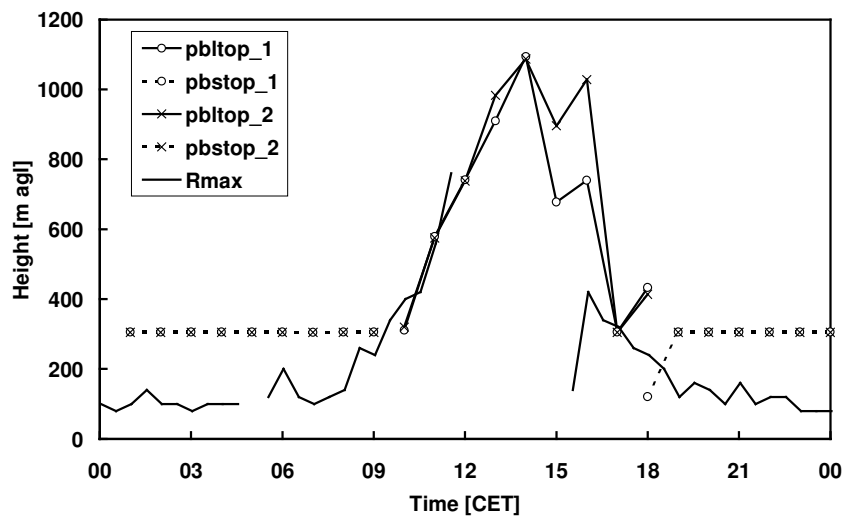


Figure 4-35: Same as Figure 4-33 for 11 September 2005.

On 5 September 2005 results look similar to results from the slab model (section 4.4.5) as both models overestimated the CBL height. The overestimation by the LM is surprising, as the Alpine pumping is reproduced by the LM when considering wind directions. The growth of the inflow layer with north north-easterly wind directions was clearly observed. Within this inflow layer, the vertical wind speed as predicted by the LM was positive, whereas negative vertical wind speeds in a range as reported in the previous section were observed in the layers above. CBL heights as detected by the LM were larger than the height of the inflow layer as observed from profiles of wind direction which is contrary to the characteristics of Alpine pumping found from sodar data.

5 Conclusions

The main objective of this study was to determine the atmospheric boundary layer (ABL) height for the complex terrain of Hohenpeißenberg, Southern Bavaria, during the SALSA 2005 campaign in August and September of 2005. In this section, a concluding summary of various methods is given and the implications of this study are outlined.

Determination of the ABL height was done for three selected days that were thought to represent different atmospheric conditions. Figure 5-1, Figure 5-2 and Figure 5-3 summarise results for the ABL depth from measurements, models and parameterisations for these days and demonstrate strengths and shortcomings of the various methods used. Radiosonde ascents were routinely performed, but low temporal and vertical resolution did not allow to infer a daily cycle of the ABL height. The considerable distance of some of the radiosonde stations to the study site challenged the validity of the data for the complex terrain. Sodar measurements supplied continuous reflectivity profiles to determine the ABL height, even though only the stable boundary layer (SBL) height, provided that it was not too shallow, and the evolution of the convective boundary layer (CBL) in the morning and forenoon hours could be detected due to its limited range. Reflectivity data had to be analysed by visual inspection of every single profile, which is time consuming and may be subjective, but could not be replaced by automatic methods. Tethered balloon data proved to be a very valuable tool to study the ABL structure in more detail due to its high resolution and revealed good agreement with sodar/RASS measurements on 5 September 2005. As tethered balloon ascents were only performed in the morning and evening hours on selected days, limited information about the daily cycle of the ABL height was provided. Attempts to parameterise the SBL height using surface flux measurements from a meadow station nearby the boundary layer station were not very useful in terms of time coverage. For two out of the three days only a limited number of data points were left after applying data selection criteria. Slab models for the CBL depth using surface flux measurements could only model the period when the CBL is growing and did not cover afternoon hours. The Lokal-Modell was the only option that provided a continuous ABL height, even though the SBL height was set to a fixed default value due to the incapability of detecting a true SBL height with the incorporated scheme.

Performance of various methods in comparison to the results from sodar measurements varied from day to day, as results from different methods were in agreement on 11 September 2005, but deviated largely on 5 September 2005. The three days appeared to represent very different conditions. On 11 September 2005 westerly winds prevailed and no influence of thermally induced wind systems was observed. Under westerly wind and partly overcast conditions thermally induced wind systems usually cannot develop. Additionally, there are no striking terrain features like deep valleys or steps in topography west of the study site. That day all methods worked best and the situation seemed to

resemble most the conditions of flat homogeneous terrain. The CBL depth from the slab model and the Lokal-Modell were especially in good agreement with measured data. Parameterisations of the SBL covered most of the second half of the night, but underestimated the measured SBL depth. On 5 September 2005 the mesoscale circulation between the foreland and the mountains was established. Southerly wind directions during the night indicated outflow of air from the Alps. The day time period of Alpine pumping when air is sucked into the Alps started with a sudden reversal of wind direction in the morning to east north-easterly whereas the transition back to southerly wind directions in the evening hours was more continuous. Complex structures in reflectivity profiles from sodar data as well as in meteorological profiles from tethered balloon data revealed the influence of this secondary wind system on the ABL structure. CBL growth was suppressed and only shallow CBL heights were reached. Processes such as subsidence and advection triggered by the mesoscale circulation played an important role. Thus, methods that were developed for flat homogeneous terrain are not applicable under these conditions. The slab model that neglects these processes largely overestimated the CBL height, as did the Lokal-Modell. Even though 30 August 2005 was another day with high radiative input, Alpine pumping did not develop. At night time, a shear layer was observed adjacent to the ground, whereas in the daytime easterly wind directions prevailed. Models worked moderately. The dissolution of the shear layer in the morning seemed to retard the growth of the CBL somewhat, which was not reproduced by the slab model. The step in topography east of the measuring site might have additionally influenced the CBL structure.

It is not possible to make general statements for the duration of the experiment. Results are only valid for the three analysed days and for the particular measuring sites, which are situated at the foot of the mountain and above the Ammer valley. Generalisation in space is not possible, as it is assumed that the mountain and the complex terrain of Hohenpeißenberg have an influence on the spatial structure of the CBL. To get information about the spatial distribution of the CBL height around Hohenpeißenberg, other methods such as a high resolution 3-D model or a more detailed measuring campaign are needed. A measuring campaign should comprise remote sensing measurements at more than one station or aircraft measurements to get more detailed insight into the spatial CBL structure. Simultaneous operation of different remote sensing techniques could make the determination of the complete diurnal cycle from measurements possible, such as a combination of sodar and wind profiler measurements (Beyrich and Görndorf, 1995) or sodar and ceilometer measurements (Emeis et al., 2004; Eresmaa et al., 2006). On the other hand, a different approach could be a 3-D model with a high resolution that is able to resolve the important terrain features such as the mountain and the Ammer valley. Models such as MUKLIMO_3 (Sievers, 2004) or the non-hydrostatic flow model MM5 (e.g. Grell et al., 2000; Weissmann et al., 2005) could be considered for such a task.

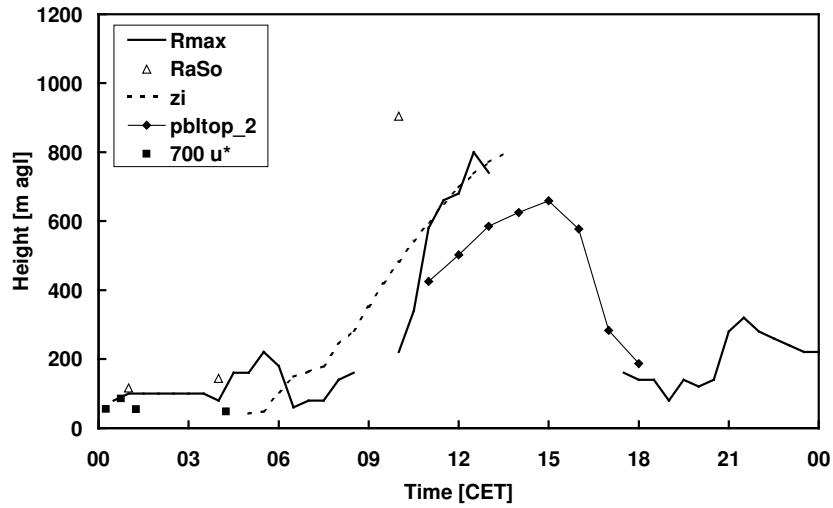


Figure 5-1: Depth of the atmospheric boundary layer from measurements (Rmax = sodar, RaSo = Radiosondes), models (zi = simple slab model, pbltop_2 = Lokal-Modell) and parameterisations (700 u*) for 30 August 2005.

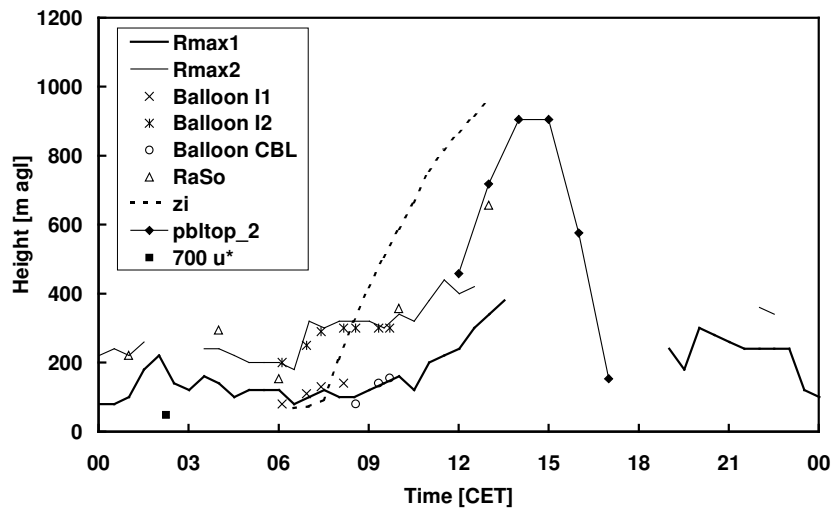


Figure 5-2: Same as Figure 5-1 for 5 September 2005 with ABL depths from tethered balloon measurements (I1 = 1st inversion, I2 = 2nd inversion, CBL = CBL height from simple parcel method).

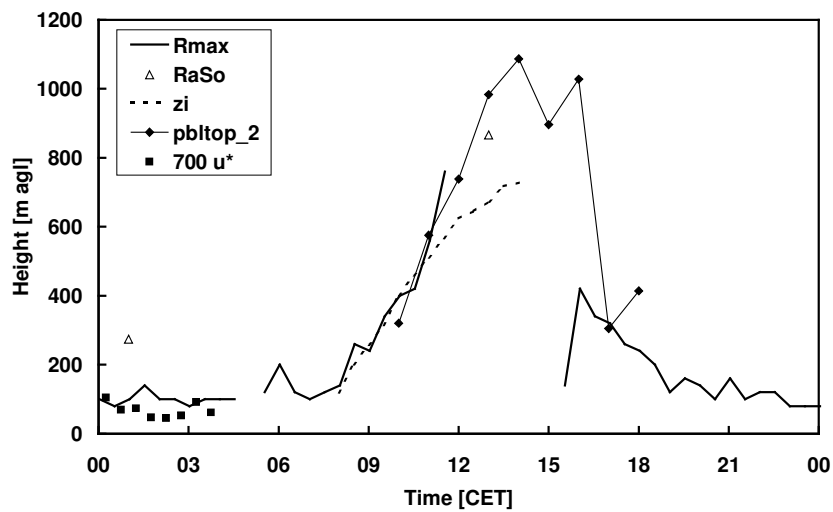


Figure 5-3: Same as Figure 5-1 for 11 September 2005.

When considering the applied methods, the determination of the ABL height from sodar data is clearly favoured for this field experiment. Sodar measurements continuously supply data with an adequate vertical as well as temporal resolution and proved to be a valuable tool to study the ABL under all conditions in the complex terrain of Hohenpeißenberg. Shortcomings are the subjectivity of the visual inspection method and the incapability of determining the ABL height in the afternoon due to the limited range of the sodar. None of the other measurement systems or parameterisations and models using surface based measurements can overcome the lack of data or provide a more comprehensive data base. Sodar measurements could not be replaced by parameterisations and slab models using surface based measurements in the complex terrain of this field experiment, as their applicability proved to be strongly dependent on the prevailing conditions. Thermally induced wind systems, especially Alpine pumping, render their applicability impossible. For this experiment, a complete diurnal cycle of the ABL height can only be achieved by combining ABL heights determined from sodar reflectivity data and CBL heights from the Lokal-Modell. But this combination is not appropriate for all days, as large overestimations could result on days influenced by thermally induced wind systems. Due to the variability of the ABL structure between individual days and the dependence of the methods on the prevailing conditions, a detailed analysis of each day is necessary to make profound statements.

6 References

- Akima, H., 1970. A new method of interpolation and smooth curve fitting based on local procedures. *Journal of the Association for Computing Machinery*, 17: 589-602.
- Arya, S.P.S., 2001. Introduction to micrometeorology. International Geophysics Series 79, Academic Press, San Diego, USA, 420 pp.
- Asimakopoulos, D.N., Helmis, C.G., Michopoulos, J., 2004. Evaluation of sodar methods for the determination of the atmospheric boundary layer mixing height. *Meteorology and Atmospheric Physics*, 85: 85-92.
- Baklanov, A., Rasmussen, A., Fay, B., Berge, E., Finardi, S., 2002. Potential and shortcomings of numerical weather prediction models in providing meteorological data for urban air pollution forecasting. *Water, Air and Soil Pollution: Focus*, 2: 43-60.
- Banta, R.M., 1984. Daytime boundary-layer evolution over mountainous terrain. Part I: Observations of the dry circulations. *Monthly Weather Review*, 112: 340-356.
- Barry, R.G., 1992. Mountain weather and climate. Routledge, London, New York, 402 pp.
- Baumann-Stanzer, K., Groehn, I., 2004. Alpine radiosoundings – feasible for mixing height determination? *Meteorologische Zeitschrift*, 13: 131-142.
- Beljaars, A.C.M., Viterbo, P., 1998. Role of the boundary layer in a numerical weather prediction model. In: A.A.M. Holtslag, P.G. Duynkerke (Editors), *Clear and cloudy boundary layers*. Royal Netherlands Academy of Arts and Sciences, Amsterdam, pp. 287-304.
- Best, P.R., Kanowski, M., Stumer, L., Green, D., 1986. Convective dispersion modelling utilizing acoustic sounder information. *Atmospheric Research*, 20: 173-197.
- Betts, A.K., 1973. Non-precipitating cumulus convection and its parameterisation. *Quarterly Journal of the Royal Meteorological Society*, 99: 178-196.
- Beyrich, F., Weill, A., 1993. Some aspects of determining the stable boundary layer depth from sodar data. *Boundary-Layer Meteorology*, 63: 97-116.
- Beyrich, F., 1994. Sodar observations of the stable boundary layer height in relation to the nocturnal low-level jet. *Meteorologische Zeitschrift*, N.F., 3: 29-34.
- Beyrich, F., Görsdorf, U., 1995. Composing the diurnal cycle of mixing height from simultaneous sodar and wind profiler measurements. *Boundary-Layer Meteorology*, 76: 387-394.
- Beyrich, F., Weisensee, U., Sprung, D., Güsten, H., 1996. Comparative analysis of sodar and ozone profile measurements in a complex structured boundary layer and implications for mixing height estimation. *Boundary-Layer Meteorology*, 81: 1-9.

- Beyrich, F., 1997. Mixing height estimation from SODAR data – a critical discussion. *Atmospheric Environment*, 31: 3941-3953.
- Businger, J.A., Arya, S.P.S., 1974. Heights of the mixed layer in the stably stratified planetary boundary layer. *Advances in Geophysics*, 18A: 73-92.
- Chemel, C., Chollet, J.-P., 2005. Observations of the daytime boundary layer in deep alpine valleys. *Boundary-Layer Meteorology*, DOI: 10.1007/s10546-005-9026-4.
- Corsmeier, U., Kottmeier, C., Winkler, P., Lugauer, M., Reitebuch, O., Drobinski, P., 2003. Flow modification and mesoscale transport caused by „alpine pumping“: a VERTIKATOR case study. International Conference on Alpine Meteorology, Brig, 2003, 3 pp. www.map.ethz.ch/icam2003/ICAM-MAP2003.htm. Accessed: 03.05.2005.
- Coulter, R.L., 1979. A comparison of three methods for measuring mixing layer height. *Journal of Applied Meteorology*, 18: 1495-1499.
- Crescenti, G.H., 1998. The degradation of doppler sodar performance due to noise: a review. *Atmospheric Environment*, 32: 1499-1509.
- Deardorff, J.W., 1972. Parameterization of the planetary boundary layer for use in general circulation models. *Monthly Weather Review*, 100: 93-106.
- Defant, F., 1949. Zur Theorie der Hangwinde, nebst Bemerkungen zur Theorie der Berg- und Talwinde. *Archives of Meteorology, Geophysics and Bioclimatology*, A1: 421-450.
- De Wekker, S.F.J., 2002. Structure and morphology of the convective boundary layer in mountainous terrain. Ph.D. Dissertation, The University of British Columbia, Vancouver, 191 pp.
- De Wekker, S.F.J., Steyn, D.G., Nyeki, S., 2004. A comparison of aerosol-layer and convective boundary-layer structure over a mountain range during STAARTE '97. *Boundary-Layer Meteorology*, 113: 249-271.
- De Wekker, S.F.J., Steyn, D.G., Fast, J.D., Rotach, M.W., Zhong, S., 2005. The performance of RAMS in representing the convective boundary layer structure in a very steep valley. *Environmental Fluid Mechanics*, 5: 35-62.
- Doms, G., Förstner, J., Heise, E., Herzog, H.-J., Raschendorfer, M., Schrodin, R., Reinhardt, T., Vogel, G., 2005. A description of the nonhydrostatic regional model LM. Part II: Physical Parameterization. LM_F90 3.16, Consortium for Small-Scale Modelling (COSMO), 140 pp. <http://www.cosmo-model.org/public/documentation.htm>. Accessed: 19.09.2006.
- Driedonks, A.G.M., 1982. Models and observations of the growth of the atmospheric boundary layer. *Boundary-Layer Meteorology*, 23: 283-306.

- Emeis, S., Türk, M., 2004. Frequency distributions of the mixing height over an urban area from SODAR data. *Meteorologische Zeitschrift*, 13: 361-367.
- Emeis, S., Münkler, C., Vogt, S., Müller, W.J., Schäfer, K., 2004. Atmospheric boundary-layer structure from simultaneous SODAR, RASS, and ceilometer measurements. *Atmospheric Environment*, 38: 273-286.
- Engelbart, D.A.M., Bange, J., 2002. Determination of boundary-layer parameters using wind profiler/RASS and sodar/RASS in the frame of the LITFASS project. *Theoretical and Applied Climatology*, 73: 53-65.
- Eresmaa, N., Karppinen, A., Joffre, S.M., Räsänen, J., Talvitie, H., 2006. Mixing height determination by ceilometer. *Atmospheric Chemistry and Physics*, 6: 1485-1493.
- Fay, B., Schrodin, R., Jacobsen, I., Engelbart, D., 1997. Validation of mixing heights derived from the operational NWP models at the German Meteorological Service. In: *The determination of the mixing height – current progress and problems*, EURASAP workshop proceedings, Risø National Lab, pp. 55-58.
- Fay, B., 2005. Operational mixing height scheme at the German Meteorological Service (DWD). In: S. Finardi (Editor): *Improved interfaces and meteorological pre-processors for urban air pollution models*, EU FP5 Project FUMAPEX Report D5.2-3: 8-13.
- Fiedler, F., Corsmeier, U., Kottmeier, C., Beheng, K.D., Kalthoff, N., Winkler, P., Adrian, G., Emeis, S., Egger, J., Höller, H., 2005. Vertical transport and orography (VERTIKATOR). In: R. Winkler (Editor), *Results of the German Atmospheric Research Programme – AFO 2000*. Federal Ministry of Education and Research (BMBF), Berlin, pp. 91-95.
- Finnigan, J., 2000. Turbulence in plant canopies. *Annual Reviews of Fluid Mechanics*, 32: 519-571.
- Foken, T., 2006. *Angewandte Meteorologie, Mikrometeorologische Methoden*. 2. Auflage. Springer Verlag, Heidelberg, 325 pp.
- Foken, T., Hartmann, K.-H., Keder, J., Küchler, W., Neisser, J., Vogt, F., 1987. Possibilities of an optimal encoding of SODAR information. *Zeitschrift für Meteorologie*, 35: 348-354.
- Foken, T., Göckede, M., Mauder, M., Mahrt, L., Amiro, B.D., Munger, J.W., 2004. Post-field data quality control. In: X. Lee (Editor), *Handbook of Micrometeorology: A Guide for Surface Flux Measurements*. Kluwer, Dordrecht, pp. 81-108.
- Garrat, J.R., 1992. *The atmospheric boundary layer*. University Press, Cambridge, 316 pp.

- Grell, G.A., Emeis, S., Stockwell, W.R., Schoenemeyer, T., Forkel, R., Michalakes, J., Knoche, R., Seidl, W., 2000. Application of a multiscale, coupled MM5/chemistry model to the complex terrain of the VOTALP valley campaign. *Atmospheric Environment*, 34: 1435-1453.
- Gryning, S.-E., Batchvarova, E., 1990. Analytical model for the growth of the coastal internal boundary layer during onshore flow. *Quarterly Journal of the Royal Meteorological Society*, 116: 187-203.
- Gryning, S.E., Batchvarova, E., 1990. Simple model of the daytime boundary layer height. *Proceedings of the 9th AMS Symposium on Turbulence and Diffusion*, Roskilde, 379-382.
- Handorf, D., Foken, T., Kottmeier, C., 1999. The stable atmospheric boundary layer over an Antarctic ice sheet. *Boundary-Layer Meteorology*, 91: 165-189.
- Hanna, S.R., 1969. The thickness of the planetary boundary layer. *Atmospheric Environment*, 3: 519-536.
- Henne, S., Furger, M., Nyeki, S., Steinbacher, M., Neininger, B., de Wekker, S.F.J., Dommen, J., Spichtinger, N., Stohl, A., Prévot, A.S.H., 2004. Quantification of topographic venting of boundary layer air to the free troposphere. *Atmospheric Chemistry and Physics*, 4: 497-509.
- Hennemuth, B., Lammert, A., 2006. Determination of the atmospheric boundary layer height from radiosonde and lidar backscatter. *Boundary-Layer Meteorology*. DOI: 10.1007/s10546-005-9035-3.
- Höller, H., Fehr, T., Friedrich, K., Hagen, M., Reitebuch, O., Corsmeier, U., 2004. VERTIKATOR – Subproject 8: Thunderstorm development over mountains. DLR, Oberpfaffenhofen, Poster. <http://www.vertikator-af02000.de>. Accessed: 09.05.2005.
- Holtslag, A.A.M., Nieuwstadt, F.T.M., 1986. Scaling the atmospheric boundary layer. *Boundary-Layer Meteorology*, 36: 201-209.
- Holtslag, A.A.M., De Bruin, E.I.F., Pan, H.-L., 1990. A high resolution air mass transformation model for short-range weather forecasting. *Monthly Weather Review*, 118: 1561-1575.
- Holzworth, C.G., 1967. Mixing depths, wind speeds and air pollution potential for selected locations in the United States. *Journal of Applied Meteorology*, 6: 1039-1044.
- Holzworth, C.G., 1964. Estimates of mean maximum mixing depths in the contiguous United States. *Monthly Weather Review*, 118: 1561-1575.
- Kallistratova, M.A., 1959. An experimental investigation in the scattering of sound in turbulent atmosphere. *Doklady Akademii Nauk SSSR*, 125: 69-72.

- Kallistratova, M.A., 1997. Physical grounds for acoustic remote sensing of the atmospheric boundary layer. In: S.P. Singal (Editor), *Acoustic remote sensing applications*. Springer Verlag, Berlin, Heidelberg, New York, pp. 3-34.
- Kalthoff, N., Binder, H.-J., Koßmann, M., Vöglin, R., Corsmeier, U., Fiedler, F., Schlager, H., 1998. Temporal evolution and spatial variation of the boundary layer over complex terrain. *Atmospheric Environment*, 32: 1179-1194.
- Keder, J., 1999. Detection of inversions and mixing height by REMTECH PA2 sodar in comparison with collocated radiosonde measurements. *Meteorology and Atmospheric Physics*, 71: 133-138.
- Kitaigorodskii, S.A., 1960. On the computation of the thickness of the wind-mixing layer in the ocean. *Bulletin (Izvestiya) Academy of Sciences, USSR, Geophysics Series*, 3: 425-431.
- Kitaigorodskii, S.A., Joffe, S.M., 1988. In search of simple scaling for the heights of the stratified atmospheric boundary layer. *Tellus*, 40A: 419-433.
- Koracin, D., Berkowicz, R., 1988. Nocturnal boundary-layer height: observations by acoustic sounders and prediction in terms of surface-layer parameters. *Boundary-Layer Meteorology*, 43: 65-83.
- Kossmann, M., Vöglin, R., Corsmeier, U., Vogel, B., Fiedler, F., Binder, H.-J., Kalthoff, N., Beyrich, F., 1998. Aspects of the convective boundary layer structure over complex terrain. *Atmospheric Environment*, 32: 1323-1348.
- Kossmann, M., Corsmeier, U., De Wekker, S.F.J., Fiedler, F., Vöglin, R., Kalthoff, N., Güsten, H., Neining, B., 1999. Observations of handover processes between the atmospheric boundary layer and the free troposphere over mountainous terrain. *Contributions to Atmospheric Physics*, 72: 329-350.
- Kossmann, M., Sturman, A.P., Zawar-Reza, P., McGowan, H.A., Oliphant, A.J., Owens, I.F., Spronken-Smith, R.A., 2002. Analysis of the wind field and heat budget in an alpine lake basin during summertime fair weather conditions. *Meteorology and Atmospheric Physics*, 81: 27-52.
- Kuwagata, T., Kimura, F., 1995. Daytime boundary layer evolution in a deep valley. Part I: Observations in the Ina Valley. *Journal of Applied Meteorology*, 34: 1082-1091.
- Lieman, R., Alpert, P., 1993. Investigation of the planetary boundary layer height variations over complex terrain. *Boundary-Layer Meteorology*, 62: 129-142.
- Little, C.G., 1969. Acoustic methods for the remote probing of the lower atmosphere. *Proceedings of the IEEE*, 57: 571-578.

- Lugauer, M., Winkler, P., 2002. Alpines Pumpen – Thermische Zirkulation zwischen Alpen und bayerischem Alpenvorland. DWD-FE-Arbeitsergebnisse Nr. 72, DWD, Hohenpeißenberg.
- Lugauer, M., Berresheim, H., Corsmeier, U., Dabas, A., Dyck, W., Emeis, S., Egger, J., Fehr, T., Fiedler, F., Freuer, Ch., Gantner, L., Gilge, S., Heese, B., Hornsteiner, M., Höller, H., Jakobi, G., Junkermann, W., Kalthoff, N., Kaminski, U., Kirchner, M., Krämer, H., Köhler, P., Kottmeier, Ch., Luksch, B., Ott, H., Plass-Dülmer, Ch., Reitebuch, O., Tagliazucca, M., Trickl, T., Vogt, S., Winkler, P., 2003. An overview of the VERTIKATOR project and results of Alpine pumping. International Conference on Alpine Meteorology, Brig, 2003, 4 pp. www.map.ethz.ch/icam2003/ICAM-MAP2003.htm. Accessed: 03.05.2005.
- Lugauer, M., Winkler, P., 2005. Thermal circulation in South Bavaria – climatology and synoptic aspects. *Meteorologische Zeitschrift*, 14: 15-30.
- Matuura, N., Masuda, Y., Inkui, H., Kato, S., Fukao, S., Sato, T., Tsuda, T., 1986. Radio acoustic measurement of temperature profile in the troposphere and stratosphere. *Nature*, 323: 426-428.
- Mauder, M., Foken, T., 2004. Documentation and instruction manual of the eddy covariance software package TK2. Arbeitsergebnisse Nr. 26, University of Bayreuth, Bayreuth. ISSN 1614-8916.
- May, P.T., Strauch, R.G., Moran, K.P., 1988. The altitude coverage of temperature measurements using RASS with wind profiler RADARs. *Geophysical Research Letters*, 15: 1381-1384.
- May, P.T., Moran, K.P., Strauch, R.G., 1989. The accuracy of RASS temperature measurements. *Journal of Applied Meteorology*, 28: 1329-1335.
- Mayer, J.-C., 2005. Characterisation of the atmospheric boundary layer in a complex terrain using SODAR-RASS. Diploma thesis, University of Bayreuth, 86 pp.
- McAllister, L.G., Pollard, J.R., Mahoney, A.R., Shaw, P.J.R., 1969. Acoustic sounding – a new approach to the study of atmospheric structure. *Proceedings of the IEEE*, 57: 579-587.
- METEK, 2000. DSDPA.90 Benutzer-Handbuch. METEK GmbH, Elmshorn, 64 pp.
- METEK, 2001. The METEK radio acoustic sounding system. METEK GmbH, Elmshorn, 22 pp.
- Neff, W.D., Coulter, R.L., 1986. Acoustic remote sensing. In: D.H. Lenschow (Editor): *Probing the atmospheric boundary layer*. American Meteorological Society, Boston, pp. 201-239.

- Nieuwstadt, F.T.M., 1981. The steady-state height and resistance laws of the nocturnal boundary layer: Theory compared with Cabauw observations. *Boundary-Layer Meteorology*, 20: 3-17.
- Oldenburg, S., 2005. Flow over hills – comparison of SODAR-RASS measurements and WasP modelling. Diploma thesis, University of Bayreuth, 105 pp.
- Pamperin, H., Stilke, G., 1985. Nächtliche Grenzschicht und LLJ im Alpenvorland nahe dem Inntalausgang. *Meteorologische Rundschau*, 38: 145-156.
- Pollard, R.T., Rhines, P.B., Thompson, R.O.R.Y., 1973. The deepening of the wind-mixed layer. *Geophysical Fluid Dynamics*, 3: 381-404.
- Raupach, M.R., Finnigan, J.J., Brunet, Y., 1996. Coherent eddies and turbulence in vegetation canopies: the mixing-layer analogy. *Boundary-Layer Meteorology*, 78: 351-382.
- Reitebuch, O., Dabas, A., Delville, P., Drobinski, P., Gantner, L., 2003. Characterisation of „Alpine Pumping“ by airborne Doppler lidar and numerical simulations. International Conference on Alpine Meteorology, Brig, 2003, 4 pp. www.map.ethz.ch/icam2003/ICAM-MAP2003.htm. Accessed: 03.05.2005.
- Reuten, C., Steyn, D.G., Strawbridge, K.B., Bovis, P., 2005. Observations of the relation between upslope flows and the convective boundary layer in steep terrain. *Boundary-Layer Meteorology*, 116: 37-61.
- Rosby, C.G., Montgomery, R.B., 1935. The layer of frictional influence in wind and ocean currents. *Papers in Physical Oceanography and Meteorology*, 3: 1-101.
- Rudolf, B., Frank, H., Grieser, J., Müller-Westermeier, G., Rapp, J., Trampf, W., 2006. Das Hochwasser in Südbayern im August 2005: Niederschlagsvorhersage, Warnung und klimatologische Bewertung des DWD. *Hochwasserschutz und Katastrophenmanagement, Ernst & Sohn Special*, 1/06: 4-13.
- Schipper, J.W., Angevine, W.M., White, A.B., Myers, T., 2002. Evaluation of relationships between boundary-layer height and heat flux. 15th Conference on Boundary Layer and Turbulence, Wageningen, Netherlands, 14.7.-19.7.2002, 4 pp.
- Seibert, P., Beyrich, F., Gryning, S.-E., Joffre, S., Rasmussen, A., Tercier, P., 1998. Mixing layer depth determination for dispersion modelling. European Commission. In: B.E.A. Fisher, J.J. Erbrink, S. Finardi, P. Jeannot, S. Joffre, M.G. Morselli, U. Pechinger, P. Seibert, D.J. Thomson (Editors), COST Action 710 – Final report. Harmonisation of the pre-processing of meteorological data for atmospheric dispersion models. European Communities, Luxembourg, 120 pp.

- Seibert, P., Beyrich, F., Gryning, S.-E., Joffre, S., Rasmussen, A., Tercier, P., 2000. Review and intercomparison of operational methods for the determination of the mixing height. *Atmospheric Environment*, 34: 1001-1027.
- Sievers, U., 2004. Das Windfeld- und Ausbreitungsmodell MUKLIMO_3, Basisversion. Deutscher Wetterdienst, Offenbach, 44 pp.
- Singal, S.P., Goel, M., 1997. Radio acoustic sounding system (RASS) for studying the lower atmosphere. In: Singal, S.P. (Editor), *Acoustic remote sensing applications*. Springer Verlag, Berlin, Heidelberg, New York, pp. 142-176.
- Sodemann, H., Foken, T., 2004. Empirical evaluation of an extended similarity theory for the stably stratified atmospheric surface layer. *Quarterly Journal of the Royal Meteorological Society*, 130: 2665-2671.
- Steenefeld, G.J., van de Wiel, B.J.H., Holtslag, A.A.M., 2006. Diagnostic equations for the stable boundary-layer height: evaluation and dimensional analysis. *Journal of Applied Meteorology and Climatology*, accepted.
- Steenefeld, G.J., van de Wiel, B.J.H., Holtslag, A.A.M., 2006. Comments on deriving the equilibrium height of the stable boundary layer. *Quarterly Journal of the Royal Meteorological Society*, submitted.
- Steinacker, R., 1984. Area – height distribution of a valley and its relation to the valley wind. *Beiträge zur Physik der Atmosphäre*, 57: 64-71.
- Stull, R.B., 1988. *An introduction to boundary layer meteorology*. Kluwer Academic Publishers, Dordrecht, 666 pp.
- Tatarskii, V.I., 1961. *Wave propagation in a turbulent medium*. McGraw-Hill, New York, 285 pp.
- Tennekes, H., 1973. A model for the dynamics of the inversion above a convective boundary layer. *Journal of the Atmospheric Sciences*, 30: 558-567.
- Tennekes, H., Driedonks, A.G.M., 1981. Basic entrainment equations for the atmospheric boundary layer. *Boundary-Layer Meteorology*, 20: 515-531.
- Troen, I.B., Mahrt, L., 1986. A simple model of the atmospheric boundary layer; sensitivity to surface evaporation. *Boundary-Layer Meteorology*, 37: 129-148.
- Van Pul, W.A.J., Holtslag, A.A.M., Swart, D.P.J., 1994. A comparison of ABL-heights inferred routinely from lidar and radiosonde at noontime. *Boundary-Layer Meteorology*, 68: 173-191.
- Vergeiner, I., Dreiseitl, E., 1987. Valley winds and slope winds – observations and elementary thoughts. *Meteorology and Atmospheric Physics*, 36: 264-286.

- Vickers, D., Mahrt, L., 2004. Evaluating formulations of stable boundary layer height. *Journal of applied meteorology*, 43: 1736-1749.
- Vogelezang, D.H.P., Holtslag, A.A.M., 1996. Evolution and model impacts of alternative boundary layer formulations. *Boundary-Layer Meteorology*, 81: 245-269.
- Weissmann, M., Braun, F.J., Gantner, L., Mayr, G.J., Rahm, S., Reitebuch, O., 2005. The alpine mountain-plain circulation: airborne Doppler lidar measurements and numerical simulations. *Monthly Weather Review*, 133: 3095-3109.
- Whiteman, C.D., 1982. Breakup of temperature inversions in deep mountain valleys: Part 1. Observations. *Journal of Applied Meteorology*, 21: 270-289.
- Whiteman, C.D., 1990. Observations of thermally developed wind systems in mountainous terrain. In: W. Blumen (Editor), *Atmospheric Processes over Complex Terrain. Meteorological Monographs*, 23(45), American Meteorological Society, Boston, USA, Chapter 2, pp. 5-42.
- Whiteman, C.D., 2000. *Mountain Meteorology*. Oxford University Press, New York, Oxford, 355 pp.
- Wiegner, M., Emeis, S., Freudenthaler, V., Heese, B., Junkermann, W., Münkler, C., Schäfer, M., Seefeldner, M., Vogt, S., 2006. Mixing layer height over Munich, Germany: Variability and comparisons of different methodologies. *Journal of Geophysical Research*, 111, D13201, DOI: 10.1029/2005JD006593.
- Wilczak, J.M., Gossard, E.E., Neff, W.D., Eberhard, W.L., 1996. Ground-based remote sensing of the atmospheric boundary layer: 25 years of progress. *Boundary-Layer Meteorology*, 78: 321-349.
- Willmott, C.J., 1982. Some comments on the evaluation of model performance. *Bulletin American Meteorological Society*, 63: 1309-1313.
- Winkler, P., Lugauer, M., Berresheim, H., Corsmeier, U., Dyck, W., Gilge, S., Kaminski, U., Kirchner, M., Köhler, P., Kottmeier, C., Luksch, B., Plass-Dülmer, C., Vogt, S., 2004. Spurenstoffflüsse aus der Grenzschicht in die freie Troposphäre – Ergebnisse aus dem VERTIKATOR Feldexperiment “Alpines Pumpen”. *DACH-Meteorologentagung 2004*, Karlsruhe. 8 pp.
- Winkler, P., Lugauer, M., Reitebuch, O., 2006. Alpines Pumpen. *Promet*, 32: 34-42.
- Wotawa, G., Kröger, H., Stohl, A., 2000. Transport of ozone towards the Alps – results from trajectory analyses and photochemical model studies. *Atmospheric Environment*, 34: 1367-1377.

- Wyngaard, J.C., Izumi, Y., Collins Jr., S.A., 1971. Behaviour of the refractive-index-structure parameter near the ground. *Journal of the Optical Society of America*, 61: 1646-1650.
- Yamada, T., 1979. Prediction of the nocturnal surface inversion height. *Journal of Applied Meteorology*, 18: 526-531.
- Yi, C., Davis, K.J., Berger, B.W., Bakwin, P.S., 2001. Long-term observations of the dynamics of the continental planetary boundary layer. *Journal of the Atmospheric Sciences*, 58: 1288-1299.
- Zilitinkevich, S., 1972. On the determination of the height of the Ekman boundary layer. *Boundary-Layer Meteorology*, 3: 141-145.
- Zilitinkevich, S., Mironov, D.V., 1996. A multi-limit formulation for the equilibrium depth of a stably stratified boundary layer. *Boundary-Layer Meteorology*, 81: 325-351.
- Zilitinkevich, S., Baklanov, A., 2002. Calculation of the height of stable boundary layers in practical applications. *Boundary-Layer Meteorology*, 105: 389-409.
- Zilitinkevich, S., Baklanov, A., Rost, J., Smedman, A.S., Lykosov, V., Calanca, P., 2002. Diagnostic and prognostic equations for the depth of the stably stratified Ekman boundary layer. *Quarterly Journal of the Royal Meteorological Society*, 128: 25-46.

7 Index of figures

Figure 2-1: Schematic daytime flow structure with convective lifting in the Northern Alps and compensating subsidence above Southern Bavaria in association with 500 hPa winds from south (full arrows) and north (dotted arrows), respectively (Lugauer and Winkler, 2005).	6
Figure 2-2: Schematic diagram of the diurnal evolution of the boundary layer over a plain in fair weather during summer. Time markers indicated by S1-S6 will be used in Figure 2-3 (Stull, 1988).....	9
Figure 2-3: Profiles of mean virtual potential temperature $\overline{\theta}_v$, illustrating the boundary layer evolution during a diurnal cycle starting in the late afternoon. S1-S6 identify each sounding with an associated launch time indicated in Figure 2-2. (FA = free atmosphere, ML = mixed layer, RL = residual layer, SBL = stable boundary layer, CL = cloud layer, SCL = subcloud layer) (Stull, 1988).	10
Figure 2-4: Temperature and wind structure evolution over a valley cross section during the course of a day focussing on the slope wind system. Lines with arrows indicate slope flows, wavy vertical lines with arrows indicate convective currents, the grey fill represents the valley inversion, and the scalloped line marks the entrainment zone at the top of the CBL (Whiteman, 2000).	12
Figure 2-5: The profile of potential temperature and heat flux distribution in a slab model (modified after Tennekes and Driedonks, 1981).....	21
Figure 3-1: Map of the Alpine foreland and the northern Alps. Hohenpeißenberg is indicated with a black triangle (modified after Top50 Viewer, Topographische Karte 1 : 1 000 000 Bundesrepublik Deutschland).	25
Figure 3-2: Contour map of mount Hohenpeißenberg and its surroundings, dotted lines mark profiles shown in Figure 3-3 (adapted from Top50 Viewer, Topographische Karte 1 : 50 000 Bayern (Süd)).	25
Figure 3-3: W-E-profile (a) and N-S-profile (b) as indicated in Figure 3-2 (adapted from Top50 Viewer, Topographische Karte 1 : 50 000 Bayern (Süd)).	26
Figure 3-4: Data processing scheme of the sodar/RASS data (Mayer, 2005).....	28
Figure 4-1: Maximum, mean and minimum daily values of temperature (a), relative humidity (b) and windspeed (c) measured at the Meteorological Observatory Hohenpeißenberg (MOHp) from 25 August to 18 September 2005 and daily precipitation (d) measured at the boundary layer station from 26 August to 18 September 2005.	39
Figure 4-2: Relative frequency of wind direction (10 min averages) at the Meteorological Observatory Hohenpeißenberg (MOHp) from 25 August to 18 September 2005 (N = 3599, wind speed > 1 m s ⁻¹).	39
Figure 4-3: Relative frequency of wind direction measured with the sonic anemometer	

(30 min averages) at the meadow station from 25 August to 18 September 2005. Dark grey: wind speed $> 1 \text{ m s}^{-1}$, light grey: wind speed $< 1 \text{ m s}^{-1}$ (N = 1141).....	41
Figure 4-4: Wind direction at the meadow station ($z = 2 \text{ m}$, 30 min averages) and the Meteorological Observatory Hohenpeißenberg (MOHp) ($z = 10 \text{ m}$, 10 min averages) for 5 September 2005.....	42
Figure 4-5: Daily total global radiation at the meadow station from 25 August to 18 September 2005. The dotted line marks 20 MJ m^{-2} (class 1 of daily total global radiation: $K_{\downarrow d} > 20 \text{ MJ m}^{-2}$, following Lugauer and Winkler, 2005).	42
Figure 4-6: Mean diurnal variation of wind direction at the Meteorological Observatory Hohenpeißenberg for period 1 and period 2.....	44
Figure 4-7: Mean diurnal variations of wind speed (a), persistence (b) and wind components ((c), (d)) at the Meteorological Observatory Hohenpeißenberg for period 1 (dashed line) and period 2 (solid line).....	45
Figure 4-8: Sodargram of the wind direction for 5 September 2005.....	46
Figure 4-9: Sodargram of horizontal wind speed for period 2 (5 September to 8 September 2005).....	47
Figure 4-10: Sodargram of wind direction for 30 August 2005.....	48
Figure 4-11: Global radiation at the meadow station for the three golden days.	49
Figure 4-12: Wind direction at the MOHp for the three golden days (30 August: grey diamonds, 5 September: black squares, 11 September: white triangles).	49
Figure 4-13: Profiles of virtual potential temperature (solid line) and relative humidity (dashed line) measured by radiosondes at Altenstadt on 30 August 2005 at 4 CET (a) and 10 CET (b). Vertical lines mark the SBL height and the CBL height, respectively, determined by different methods (SPM = simple parcel method, 1stD = 1 st discontinuity, HU= humidity jump).	52
Figure 4-14: Profiles measured by radiosonde at Altenstadt on 5 September 2005, 4 CET. (a): virtual potential temperature (solid line) and relative humidity (dashed line), (b): wind speed (solid line) and wind direction (dashed line). Vertical lines mark the SBL height and the CBL height, respectively, determined by different methods (1stD = 1 st discontinuity, HU = humidity jump, WMAX = maximum of wind speed, WMIN = minimum of wind speed).....	52
Figure 4-15: Sodargram of reflectivity for 30 August 2005. The ABL height is indicated by the black line, thereby values are indicated at the end times of the half hour period.....	54
Figure 4-16: Sodargram of reflectivity for 5 September 2005. The ABL height is indicated by the black line, thereby values are indicated at the end times of the half hour period.....	54
Figure 4-17: Sodargram of the standard deviation of the vertical wind velocity for 5 September 2005. The ABL height determined from reflectivity profiles is	

indicated by the black line, thereby values are indicated at the end times of the half hour period.....	55
Figure 4-18: Sodargram of reflectivity for 11 September 2005. The ABL height is indicated by the black line, thereby values are indicated at the end times of the half hour period.....	55
Figure 4-19: ABL depths derived from the automatic detection from sodar measurements (MLH, H1, H2 after Emeis and Türk, 2004) as well as Rmax 1 and Rmax 2 as determined by visual inspection from the profile of reflectivity for 30 August 2005.....	58
Figure 4-20: Same as Figure 4-19 for 5 September 2005.....	58
Figure 4-21: Same as Figure 4-19 for 11 September 2005.....	58
Figure 4-22: ABL heights derived from the modified automatic detection from sodar measurements (MLH mod, H1 mod, H2 mod) as well as Rmax 1 and Rmax 2 as determined by visual inspection from the profile of reflectivity for 30 August 2005.	61
Figure 4-23: Same as Figure 4-22 for 5 September 2005.....	61
Figure 4-24: Same as Figure 4-22 for 11 September 2005.....	61
Figure 4-25: Virtual potential temperature profile evolution from tethered balloon data for 5 September 2005. Balloon ascents are marked by thin lines, descents by thick lines. Flights are labelled by the corresponding flight times [CET].....	63
Figure 4-26: Simultaneously measured profiles of virtual potential temperature measured by tethered balloon soundings (dots) and profiles of reflectivity measured by sodar (line) on 5 September 2005 ((a): 08:14-08:34 CET, (b): 09:01-09:20 CET, (c): 09:25-09:42 CET). The dashed line marks the CBL depth derived from the reflectivity profile (Rmax1).....	65
Figure 4-27: Simultaneously measured profiles of specific humidity measured by tethered balloon soundings (dots) and profiles of reflectivity measured by sodar (line) on 5 September 2005 ((a): 08:14-08:34 CET, (b): 09:01-09:20 CET, (c): 09:25-09:42 CET). The dashed line marks the CBL depth derived from the reflectivity profile (Rmax1).....	65
Figure 4-28: Predicted h [m agl] vs observed h [m agl] for stable boundary layer depth formulations described in the text with parameters in Table 2-1 and Table 2-2 for 30 August (white diamonds), 5 September (cross) and 11 September 2005 (black circles).	68
Figure 4-29: Same as Figure 4-28 but difference in elevation considered (SBL heights [m asl]).....	70
Figure 4-30: Development of the CBL for 30 August 2005 from sodar data (Rmax) and modelled by slab models. (Abbreviations: z_i = equation (2-33), $z_i(Y_i)$ and $z_i(\text{Sch})$ = equation (2-34), using coefficients by Yi et al. (2001) and Schipper et al. (2002) respectively, $z_i(\text{G\&B})$ = equation (2-31)).	72

Figure 4-31: Same as Figure 4-30 for 5 September 2005.....	72
Figure 4-32: Same as Figure 4-30 for 11 September 2005.....	72
Figure 4-33: ABL depth from Lokal-Modell output for 30 August 2005 in comparison to ABL depths determined from sodar reflectivity profiles (Rmax). pbltop = CBL or RL depth, pbstop = SBL depth. Indices 1 and 2 stand for the two grid points in the vicinity of Hohenpeißenberg.	76
Figure 4-34: Same as Figure 4-33 for 5 September.....	76
Figure 4-35: Same as Figure 4-33 for 11 September 2005.....	76
Figure 5-1: Depth of the atmospheric boundary layer from measurements (Rmax = sodar, RaSo = Radiosondes), models (zi = simple slab model, pbltop_2 = Lokal-Modell) and parameterisations (700 u*) for 30 August 2005.	80
Figure 5-2: Same as Figure 5-1 for 5 September 2005 with ABL depths from tethered balloon measurements (I1 = 1st inversion, I2 = 2nd inversion, CBL = CBL height from simple parcel method).....	80
Figure 5-3: Same as Figure 5-1 for 11 September 2005.....	80

8 Index of tables

Table 2-1: Dimensionless coefficients from Handorf et al. (1999) for the use in (2-14) and (2-23).	20
Table 2-2: Dimensionless coefficients from the literature (after Vickers and Mahrt, 2004; Steeneveld et al., 2006a).	20
Table 3-1: Coordinates of the measuring stations.	27
Table 3-2: Sounding parameters for the continuous measurements at location 1 and location 2 during SALSA 2005.	28
Table 3-3: Locations of radiosounding stations.	29
Table 3-4: Criteria for boundary layer height estimation from sodar data in the stable and shallow convective boundary layer (Beyrich et al., 1996).	32
Table 4-1: ABL heights [m asl] determined from radiosonde ascents at Oberschleißheim (OS), Altenstadt (AS) and Hohenpeißenberg (HP) following various criteria (SPM = simple parcel method, 1stD = 1 st discontinuity, HU = humidity jump, WMAX = maximum of wind speed, WMIN = minimum of wind speed, RI = Richardson number, RI(VH) = Richardson number after Vogelezang and Holtslag (1996).)	51
Table 4-2: Characteristics of the development of the CBL height using the elevated (secondary) maximum of reflectivity criterion.	56
Table 4-3: Statistical measures for the comparison of the outputs of the automatic routine to the lowest elevated maximum of reflectivity. Outputs of the automatic routine are: MLH (the ABL height) and H1 and H2 (criteria used in the routine). Only data from 0 CET until 13:30 CET was used for the statistical analyses. (MAE = mean absolute error [m], RMSE = root mean square error [m], MPB = mean percent bias [%]).	59
Table 4-4: Statistical measures for the comparison of the outputs of the modified automatic routine to the lowest elevated maximum of reflectivity. Outputs of the automatic routine are: MLH (the ABL height) and H1 and H2 (criteria used in the routine). Only data from 0 CET until 13:30 CET was used for the statistical analysis. The second number of cases N applies to the second criteria H2 as this criteria was not fulfilled in all cases. (MAE = mean absolute error [m], RMSE = root mean square error [m], MPB = mean percent bias [%]).	62
Table 4-5: Distribution of quality flags after Foken et al. (2004) for the friction velocity u_* and the buoyancy flux for the 13 half-hourly cases used for the parameterisations of the SBL depth.	67
Table 4-6: Statistical measures for the comparison of observed and predicted SBL depths [m agl] for the whole dataset (N = 13). Abbreviations for SBL depth formulations as described in section 2.3.4.2. Abbreviations for statistical measures see Table 4-4. Bold numbers mean the best quality for the particular statistical	

quantity.....	67
Table 4-7: Same as Table 4-6 but difference in elevation considered (SBL heights [m asl]).....	69
Table 4-8: Average lapse rates γ [K km^{-1}] determined from all potential temperature radiosonde profiles of the respective day between 1000 and 3500 m agl.....	71
Table 4-9: Statistical measures for the comparison of observed and modelled CBL depths. (Abbreviations: z_i = equation (2-33), $z_i(\text{Yi})$ and $z_i(\text{Sch})$ = equation (2-34), using coefficients by Yi et al. (2001) and Schipper et al. (2002) respectively, $z_i(\text{G\&B})$ = equation (2-31)). Bold numbers mean the best quality for the particular statistical quantity.....	73
Table 10-1: Technical specifications of the sodar system.....	101
Table 10-2: Technical specifications of the RASS system.	101
Table 10-3: Technical specifications of the entire system.	102
Table 10-4: Technical specifications of the meteorological sensors.....	102
Table 10-5: Technical specifications of the telemetry.....	102
Table 10-6: Technical specifications of the turbulence measurements.....	103
Table 10-7: Technical specifications of the radiation measurements.....	103
Table 10-8: System Specifications of the tethersonde meteorological tower.	103
Table 10-9: Sensor Specifications of the tethersondes.....	104
Table 10-10: Tethered balloon specifications.	104

9 Index of used abbreviations and symbols

9.1 Abbreviations

ABL	Atmospheric boundary layer
agl	Above ground level
asl	Above sea level
CBL	Convective boundary layer
CET	Central European Time
CL	Cloud layer
DWD	Deutscher Wetterdienst (German Meteorological Service)
FA	Free atmosphere
GAW	Global Atmosphere Watch
lidar	Light detecting and ranging
LM	Lokal-Modell
LLJ	Low-level jet
ML	Mixed layer
MOHp	Meteorological Observatory Hohenpeißenberg
NWP	Numerical weather prediction
PBL	Planetary boundary layer
radar	Radio detecting and ranging
RASS	Radio acoustic sounding system
RL	Residual layer
SALSA	Beitrag salpetriger Säure zur atmosphärischen OH-Konzentration
SBL	Stable boundary layer
SCL	Subcloud layer
sodar	Sound detecting and ranging
TKE	Turbulence kinetic energy
TRACT	Transport of air pollutants over complex terrain
VERTIKATOR	Vertical exchange and orography

9.2 Latin symbols

B_s	Scaled surface buoyancy flux	$\text{m}^2 \text{s}^{-3}$
c_a	Speed of sound	m s^{-1}
c_p	Specific heat at constant pressure	$\text{J kg}^{-1} \text{K}^{-1}$
C_N^2	Refraction structure parameter	$\text{m}^{-2/3}$
C_T^2	Temperature structure parameter	$\text{K m}^{-2/3}$
f	Coriolis parameter	s^{-1}
g	Acceleration due to gravity	m s^{-2}

h	Stable boundary layer depth	m
H	Surface buoyancy flux	$W m^{-2}$
H ₁	Criteria 1 for the automatic determination of the ABL height	m
H ₂	Criteria 2 for the automatic determination of the ABL height	m
K _d	Daily total global radiation	$MJ m^{-2}$
L	Obukhov length, including von Kármán constant	m
L*	Obukhov length, von Kármán constant not included	m
l _t	Characteristic scale of temperature inhomogeneities	m
M	Molecular weight of air	$kg mol^{-1}$
MAE	Mean absolute error	
MLH	Height of the mixing layer	m
MPB	Mean percent bias	%
N	Buoyancy frequency in the free atmosphere above the boundary layer (Brunt-Väisälä frequency)	s^{-1}
O	Observed variables	
p	Air pressure	hPa
P	Model predicted variables	
P	Persistence	-
pbltop	Height of the mixed (convective) layer or residual layer in the LM	m
pbstop	Height of the stable nocturnal boundary layer in the LM	m
q	Specific humidity	$kg kg^{-1}$
r	Pearson's correlation coefficient	-
r ²	Coefficient of determination	-
R	Universal gas constant (8.3145)	$J mol^{-1}K^{-1}$
R	Acoustic reflectivity	dB
R _{max}	Height of a (secondary) elevated maximum in reflectivity	m
Ri	Gradient Richardson number	-
Ri _b	Bulk Richardson number	-
Ri _c	Critical Richardson number	-
Ri _g	Bulk Richardson number (after Vogelezang & Holtslag, 1996)	-
RMSE	Root mean square error	
s	Wind speed	$m s^{-1}$
t	time	s
T	Air Temperature	K
T _s	Sonic temperature	K
T _v	Virtual temperature	K
u	Horizontal component of wind speed	$m s^{-1}$
u*	Friction velocity	$m s^{-1}$

v	Lateral component of wind speed	m s^{-1}
w	Vertical component of wind speed	m s^{-1}
w'	Fluctuation of the vertical component of wind speed	m s^{-1}
\overline{w}	Large scale vertical motion at the top of the mixed layer	m s^{-1}
w_e	Entrainment velocity	m s^{-1}
w^*	Convective scaling velocity	m s^{-1}
z	Height	m
z_i	Convective boundary layer depth	m

9.3 *Greek symbols*

γ	Gradient of potential temperature	K m^{-1}
γ	Ratio of specific heat	-
$\Delta\theta$	Temperature jump at the top of the mixed layer	K
θ	Potential temperature	K
θ_0	Potential temperature at the surface	K
θ'	Fluctuation of the potential temperature	K
θ_m	Mixed layer potential temperature	K
θ_v	Virtual potential temperature	K
Θ_B	Bragg angle	$^\circ$
κ	Von-Kármán-constant (0.4)	-
λ_a	Wavelength of the sound	m
λ_r	Wavelength of the radar waves	m
σ_w	Vertical wind velocity standard deviation	m s^{-1}
$\overline{w'\theta'}$	Kinematic turbulent heat flux	K m s^{-1}
$\left(\overline{w'\theta'}\right)_i$	Kinematic turbulent heat flux at the top of the mixed layer	K m s^{-1}
$\left(\overline{w'\theta'}\right)_s$	Kinematic turbulent heat flux at the surface	K m s^{-1}
$\overline{w'\theta'_v}$	Kinematic buoyancy flux	K m s^{-1}

10 Appendix: Technical specifications of measurement systems

Sodar/RASS system

Sodar type: DSDPA.90/64

Manufacturer: METEK, Meteorologische Messtechnik GmbH, Germany

Table 10-1: Technical specifications of the sodar system.

Property	Description/Value
Operating range	
Wind velocity	0-35 m s ⁻¹
Wind direction	0-360°
Standard deviation of radial components	0-3 m s ⁻¹
Accuracy	
Wind velocity (0-5 m s ⁻¹)	± 0.5 m s ⁻¹
Wind velocity (5-35 m s ⁻¹)	± 10%
Wind direction	± 5°
Radial components	± 0.1 m s ⁻¹
Standard deviation of radial components	± 0.15 m s ⁻¹
Range of measurements	
Minimum height	10 m
Height resolution	5–100 m
Availability	80% up to 200 m
Transmitted frequency	
Tunable	1.0-4.0 kHz

Table 10-2: Technical specifications of the RASS system.

Property	Description/Value
Transmitter	
Operating frequency	1290 MHz
Transmitting power	20 W
Frequency stability	2·10 ⁻⁶
Single side band phase-noise	-100 dBc/Hz
Modulation	Continuous wave
Receiver	
Detection	Phase synchronously with respect to transmit signal
Noise figure	1.5 dB
Bandwidth	32·(c _a /Δh) [Δh = height res.]
Noise bandwidth	(c _a /Δh)
Antennas	
Parabolic dish diameter	Ø 1.8 m

Table 10-3: Technical specifications of the entire system.

Property	Description/Value
Electrical values	
Sodar computer	230 V, 250 W
Power supply	230 V, 2500W
Data transfer	
4 RS-232 (V.24) interfaces	110-38400 Baud

Radiosonde

Type: RS92-SGP

Manufacturer: Vaisala, Finland

Table 10-4: Technical specifications of the meteorological sensors.

Sensor/Property	Description/Value
Temperature	Type: capacitive wire
Range	+60°C to -90°C
Accuracy	± 0.5°C (total uncertainty in sounding)
Resolution	0.1°C
Humidity	Type: thin-film capacitor, heated twin sensor
Range	0 to 100% RH
Accuracy	± 5% RH (total uncertainty in sounding)
Resolution	1% RH
Pressure	Type: silicon
Range	1080 to 3 hPa
Accuracy	1080 – 100 hPa: 1 hPa (total uncertainty in sounding) 100 – 3 hPa: 0.6 hPa (total uncertainty in sounding)
Resolution	0.1 hPa

Table 10-5: Technical specifications of the telemetry.

Sensor/Property	Description/Value
Transmitter type	Synthesized
Frequency band	403 MHz
Tuning range	400-406 MHz
Frequency stability, 90 % probability	± 2 kHz
Deviation, peak-to-peak	4.8 kHz
Emission bandwidth	According to EN 302 054
Output power (high-power mode)	60 mW min
Modulation	GFSK
Data downlink	2400 bit/s, digital
Measurement cycle	1 s
Code correlating GPS Receiver (SA OFF, PDOP<4)	
Number of channels	12
Navigation accuracy	
Positioning uncertainty, horizontal	10 m
Velocity measurement uncertainty	0.15 m/s
Directional measurement uncertainty	2 degrees

Turbulence Measurements

Table 10-6: Technical specifications of the turbulence measurements.

Sensor/Property	Description/Value
Sonic anemometer	CSAT3 (Campbell), SN: 235-2
CO ₂ /H ₂ O-analyser	LICOR LI7500 (Campbell), SN: 754-0220
Thermometer	AIR150, SN: 9
System setup:	
Measuring height	2.1 m above canopy height
Orientation of sonic anemometer	240° (expected wind direction)
Orientation hygrometer	North
Positioning hygrometer	Distance to centre of sonic anemometer: 25 cm 5 cm below the centre of the sonic anemometer
Platinum thermometer	Distance to centre of sonic anemometer: 5 cm
Logger	Campbell CR23X, SN: 1351
Logger-program	CSAT3_36

Radiation measurements

Table 10-7: Technical specifications of the radiation measurements.

Sensor/Property	Description/Value
Pyranometer (upper half space)	CM21 (Kipp & Zonen B.V.), SN: 020955 Correction: $\mu\text{V} = \text{value}/11.19 \mu\text{V W}^{-1} \text{m}^2$
Pyranometer (lower half space)	CM21 (Kipp & Zonen, B.V.), SN: 020956 Correction: $\mu\text{V} = \text{value}/11.04 \mu\text{V W}^{-1} \text{m}^2$
Pyrgeometer (upper half space)	Eppley PIR Pyrgeometer, SN: 32006F3 No f-correction possible
Pyrgeometer (lower half space)	Eppley PIR Pyrgeometer, SN: 32007F3
System setup:	
Measuring height	2 m above ground
Orientation	South
Logger	QLC1 (Vaisala), SN: 52523 QLI1 (Vaisala): SN 52527

Tethered balloon

Table 10-8: System Specifications of the tethered meteorological tower.

Sensor/Property	Description/Value
Capacity	Up to 6 tethered sensor packages (Tethersondes) Ozonesonde optionally
Measurements	Wind speed, wind direction, pressure, temperature, relative humidity, ozone (optional)
Frequency	400-406 MHz
Antenna	Monopole antenna with preamp and 50 ft cable
Altitude	Up to 3 km
Software	TMT Application Software
Standard system configuration	AIR-5A-RCVR 403 MHz receiver, notebook PC, electric winch with tetherline, up to six tethersondes and tethered balloon

Tethersonde type: TS-5A-SP

Manufacturer: Vaisala, Finland

Table 10-9: Sensor Specifications of the tethersondes.

Sensor/Property	Description/Value
Temperature	
Range	+50°C to -40°C
Accuracy	± 0.5°C
Resolution	0.1°C
Humidity	
Range	0 to 100% RH
Accuracy	± 3% RH
Resolution	0.1% RH
Pressure	
Range	1050 to 600 hPa
Accuracy	± 1 hPa
Resolution	0.1 hPa
Temperature compensation	automatic
Wind speed	
Range	0 to 20 m s ⁻¹
Accuracy	± 0.5 m s ⁻¹
Wind Direction	
Range	0 to 360°
Accuracy	± 10°

Table 10-10: Tethered balloon specifications.

Model	Description	Length	Diameter	Payload
TSB-7	7.0 m ³ balloon	4.57 m	2.13 m	4.22 kg

Acknowledgements

First of all, I very much would like to thank my supervisor Prof. Thomas Foken for making this thesis possible and for always being supportive of my work.

I am grateful to Prof. Franz X. Meixner from the Max Planck Institute for Chemistry for giving me the opportunity to participate in the SALSA 2005 experiment. The whole SALSA crew made the field campaign at Hohenpeißenberg not only a very salutary but also a personally enriching time.

I wish to thank the Meteorological Observatory Hohenpeißenberg headed by Prof. Harald Berresheim for making the data available, especially to Thomas Elste for responding to all my questions concerning this data.

For hosting me at the Meteorology and Air Quality department of Wageningen University, the Netherlands, I would like to thank Prof. Bert Holtslag, Gert-Jan Steeneveld and Joel Schröter. They instructed me with data analysis and provided useful suggestions.

I would like to thank Jens Mayer and Michael Kortner from the Max Planck Institute of Chemistry as well as Dr. Tiina Markkanen and Dr. Johannes Lüers from the University of Bayreuth who gave me helpful advice during the data analysis and writing my thesis.

I wish to thank all my friends who encouraged me during my work. Thanks to Daniela, who made our office a pleasant place to work, and to Andra and Julia for reviewing this thesis.

I am very grateful to my parents for their manifold support during my studies.

Lastly, I am deeply grateful to my boyfriend Florian whose continuous support and encouragement I needed so much to complete this thesis.

Eidesstattliche Erklärung

Hiermit erkläre ich, dass ich die vorliegende Diplomarbeit selbständig verfasst und keine anderen als die angegebenen Quellen und Hilfsmittel verwendet habe.

Bayreuth, den 29. September 2006

Katharina Staudt